Wesleyan University

Shadows on the Sky: Mapping *New Horizons'* Vision of the Local Interstellar Cloudscape

by

Rewa Clark Bush
Class of 2024

A thesis submitted to the
faculty of Wesleyan University
in partial fulfillment of the requirements for the
Degree of Master of Arts

Middletown, Connecticut April, 2024

The void is a spectral realm; not even nothing can be free of ghosts.

—Karen Barad

Physicist

Acknowledgements

To begin, I acknowledge the Wangunk of central Connecticut, the people at the bend in the river, on whose ancestral and unceded land Wesleyan University is situated, as I continue examining the ways metaphors of *conquest* and *the final frontier* are enacted in our science and impact our world as more than metaphor.

I have immense gratitude for my thesis advisor, Seth Redfield, who championed this project every step of the way. In addition to being a generous scientific resource and collaborator, Seth has been a first-rate mentor, offering wisdom and support through the ups and downs of the research process. Seth always trusted me to make my own decisions, which has helped me learn to trust myself.

Warmest thanks to Meredith Hughes for offering heartfelt mentorship from my earliest days at Wesleyan; Roy Kilgard for delighting with me in the histories and paraphernalia of the scientific endeavor; and Sarah Wellons and Ed Moran for some of the most enjoyable and elegantly crafted classes I've had. Thank you all for patiently sitting though countless office hours, and at the end of the day, reminding me that done is better than perfect. Special thanks to our enthusiastic accomplice, Stef Dinneen, for providing the glue that holds this department together, and helping me realize every one of my outrageous ideas.

I deeply appreciate the Wesleyan Astronomy Department at large for supporting this most unusual master's program. I would likely no longer be in the field if it weren't for this program opening up a bridge. You are doing something incredibly significant here by sustaining a lifeline for non-traditional students; thank you for seeing tenacity in our circuitous paths, and believing that we were too important to let slip through the cracks.

Beyond the domes of Van Vleck Observatory, I am grateful to Brian Stewart

for making me feel welcome in Exley Science Center; Keiji Shinohara for accompanying my artistic explorations into the practice of capturing cloudscapes; fellow organizers of the Wesleyan Graduate Labor Union for grounding me in something beyond myself; the extravagant saucer magnolia tree outside Davison Health Center; and Wesleyan's grounds keepers, Physical Plant workers, clerical workers, and cleaning staff who make all of this possible.

I am grateful to have been in conversation with Daniel Kwan, co-director of the 2022 A24 film *Everything Everywhere All At Once*, and a gaggle of brilliant students, faculty, and staff from across the disciplines whose generous insights on my thesis helped me understand how we, like clouds, transcend every boundary we put on ourselves. I am especially grateful to MJ Rubenstein, the orchestrator of that conversation and many others, for indelibly shaping my approach to this thesis and my perception of the humility required of us as scientists that seek to describe a universe that is very much alive and shifting beneath our fingertips.

My dear friend Caroline Meister is in this thesis because, in the words of our teacher Thích Nhất Hạnh, a cloud never dies. In the past month I have become aware of the immense web of people that Caroline touched, of which I was unwittingly a thread. I am the way I am because of the ways she shaped me, and she was who she was because of all those who knew and shaped her, which means I am the way I am because of them, too, these numerous people I have never met but who already live on in me.

In this spirit, I am unspeakably indebted to my friends and family, my teachers, and my students, who have all shaped me into who I am (becoming). Enormous gratitude goes to Anza Jarschke, who enabled me to attend my first math class seven years ago and believed me when I labeled the notebook "Astrophysics Step One." Infinite, loving thanks to Mom, Dad, and Burton, Wendy Faris, Barbara

and Koorosh Komeyli, Stéphane Bernard, Helena Omaña Zapata, Wren Leader, Kristen Stipanov, and the INFJs for celebrating each step that came after. I'm grateful to Karen Barad for telling me to stick with it, and to my many scientific role models – notably Robin Wall Kimmerer, Chanda Prescod-Weinstein, Carl Sagan, and Melinda Soares-Furtado – whose insistence that we hold our science and our humanity in the same breath inspires me to make a place for myself here. Thanks to Kate Brown for first introducing to me the possibility that I think like a physicist, as well as Stan Rushworth, Kelli Horner, Karen Groppi, Matt Wetstein, and my WiSE friends at Cabrillo Community College. Immense thanks to Enrico Ramirez-Ruiz, Deana Tanguay, Samantha Wu, and the Lamat scholars for being the warmest scientific family anyone could dream of.

Thank you to the Wesleyan students of ASTR 155, 105, and 211 for witnessing my baby steps as a TA, and my classmates for carrying me through; to my wonderful friends, Carlos Ordoñez, Eva Yang, Lily Henley, Anya Shatilova, Venus Marroquin, Angelina Reddy, Isaac Moss, Qiushi Tian, Kyle McGregor, Fi Keane, Sarah Rosen, and Katie Sagarin; to the VVO postdocs, Jonathan Jackson, Azmain Nisak, Brianna Zawadzki, and the EPIC research group for your guidance; to my fellow master's students, Sara Negussie, Alaina Einsig, Katie Ciurleo, and Cat Sarosi for showing me how it's done, and how we do it even when we're scared; and to Lisseth Gonzales Quevedo and Pritha Sengupta, for being my home away from home and for your frustratingly relentless positivity.

This research was made possible by funding from the NASA Connecticut Space Grant Consortium, Wesleyan Graduate Student Association, American Astronomical Society, and New Horizons Science Team. I particularly wish to thank Pontus Brandt for his enthusiastic support of this project, and Randy Gladstone, Joel Parker, and Max Gronke for their expert assistance.

Most importantly, Reader, thank you. I hope you find something of value here that propels you forward with your own scientific questions. When we engage in research, we enter into a conversation with the entire scientific community – past, present, and future – in which we are collectively expanding the edges of humanity's understanding of our Universe. We reach out and grasp things that do not yet have words, and together try to name them and uncover their place in the order of things. All the better when someone comes along to disorder the order and question the names. Please take what you find here and run with it; make it better. I am excited to see where we go together, and honored to be a part of the conversation.

Contents

Chapter 1

Introduction

Outer space is far from empty. Rather than the vast void popularized in science fiction films ("In space no one can hear you scream"[1]), our cosmos is a veritable soup of gas and dust. Our Galaxy, and other galaxies, ranges in density from 10^{-6} particles per cubic centimeter in the hot ionized medium (Cox 2005) to 10^{6} particles per cubic centimeter in cold molecular clouds (Saintonge & Catinella 2022), meaning even the seemingly emptiest hinterlands have a topography.

Our solar system itself is couched in an environment of interstellar gas clouds, composed of ambient gas and dust known as the local interstellar medium. These clouds do not shine in light visible to the eye, but have been inferred based on how they block ultraviolet (UV) radiation from the spectra of nearby stars. Over the past 40 years, numerous studies have gradually pieced together a map of our interstellar environs, identifying over a dozen distinct clouds directly surrounding the Solar System (Crutcher 1982; Lallement et al. 1994; Redfield & Linsky 2000, 2008).

We now have a distinct opportunity to test this cloud map, thanks to the *New Horizons* (*NH*) spacecraft. When *NH* left Earth in 2006, it was the fastest spacecraft ever launched. *NH* gave us our first glimpse of Pluto in 2015 (Stern et al. 2015), followed by our first encounter with a Kuiper Belt object in 2018 (Stern et al. 2019), and then... it just kept going. Few spacecraft have ever

[1] O'Bannon, Dan. *Alien*. Film. USA: 20th Century-Fox, 1979.

ventured this far; the last of the *Pioneers* stopped operating in 2003, and while the *Voyager* missions still operate, they do not have the UV capabilities of *NH*. As the only UV telescope in the outer Solar System, *NH* now provides a remarkably unique vantage point from which to observe.

At the moment of this writing, as part of its extended mission, *NH* has just completed its first all-sky observations from a phenomenal distance of 58 au from the Sun. At this far-flung location where the Sun has been reduced to 1/3000th its intrinsic brightness, *NH* may finally be able to glimpse the shadows of these elusive interstellar clouds against the dim backdrop of the Galaxy.

In this thesis, I utilize a map of all known LISM clouds to model how light streaming towards us from the Galaxy in the form of UV Lyman-alpha (Lyα) photons should be filtered through this cloudscape. Ultimately I predict the Lyα flux we expect *NH* to measure from its current position and compare our predictions with the new all-sky data. There exist many more factors than we will be able to account for; worlds are far more complex than any map can pin down. But in the spirit of statistician George Box who popularized the aphorism, “All models are wrong, some are useful" (Box & Draper 1986), we aim to construct a model that may be of use to the *NH* Science Team and wider LISM community, as we take a stab at determining whether *NH* is indeed able to image the environment in which our solar system resides for the first time.

1.1 Local Interstellar Medium

Our Sun is just one star among billions in the Milky Way Galaxy. Observations of the light reaching us from distant stars provide information both about the stars themselves, and the interceding material the light has passed through along its

trajectory. This material is collectively known as the interstellar medium (ISM), the diffuse gas and dust that permeates the space between stars. It is largely comprised of hydrogen gas leftover from the Big Bang and other trace elements propelled into the expanse between stars by supernovae. When a supernova sends a shock wave rippling through space, it propagates as a density wave in the ISM, bunching up regions of over-density that become ripe environments for the formation of new stars (Zucker et al. 2022). Consequently, the ISM is the material from which stars are born and into which stellar material disperses at the end of the stellar life cycle. Its properties vary widely from place to place, recording the history of the celestial bodies within it.

Figure 1.1: The space between stars is not empty. The rapidly-moving giant star Zeta Ophiuchi produces a shock wave in the interstellar dust, as seen in this infrared image from NASA's *Spitzer Space Telescope*. (Image: NASA/JPL-Caltech.)

As our solar system orbits the center of the Milky Way Galaxy roughly once every 230 million years, it passes through diverse regions of ISM, some diffuse

($n \sim 10^{-6}$ cm^{-3}), some clumpy ($n \sim 10^{6}$ cm^{-3}) (Draine 2011). We can see this happening to other stars (e.g., Fig. 1.1) as they create bow shocks in the interstellar dust of the Galaxy as they move. For a ship sailing on the ocean, whether the surrounding waters are calm or rocky has profound implications for the well-being of the passengers on board. Similarly, mapping and characterizing the morphology and dynamics of the Solar System's immediate surroundings allows us to understand the impact the ISM has on the shape of our heliosphere, and may even shed light on the history and future of life in the Solar System (Wyman & Redfield 2013; Zank & Frisch 1999; Vannier et al. 2019).

1.1.1 What Is It & How Do We Know?

What is this material that fills in the voids between stars? The compositional breakdown of the ISM is predominantly hydrogen and helium, created in abundance in the Big Bang, with a small reduction in H fraction and small increase in He fraction, plus the addition of small amounts of heavier elements (from carbon to uranium), as can be expected from the recycling of elements created in stars and stellar explosions (Draine 2011). The heavy elements decline in abundance from the center of the Milky Way outwards; as the Sun resides ~ 8.5 kpc from the Galactic Center, the LISM heavy metal abundance is roughly half that of the Galactic Center.

These properties were determined by analyzing the spectra of stars, breaking up their light into the constituent wavelengths, and studying what is missing. Stars of a given mass emit light in an extremely well-characterized distribution, but that light can be distorted in unique ways when it encounters atoms en route. Each atomic element exists in its own unique energy states that allow it to ab-

sorb light of specific wavelengths, leaving any passing starlight deficient in those wavelengths. For example, observations of α Centauri A and B, the closest binary stars to Earth at a distance of 1.3 pc, reveal that they are both deficient in light of wavelengths 1215.67 Å and 1215.35 Å (1 Å = 10^{-8} cm), which are good indicators that the starlight has passed through a region of ISM (Fig. 1.2). The details of that deficiency – the shape, width, and depth of the absorption line missing from the stellar spectrum – encodes information about the absorbing media, including its velocity (centroid), amount or column density (depth), and temperature/turbulence (width). A schematic breaking down the Lyα absorption line from α Centauri B is shown in Figure 1.3.

An early example of ISM spectral lines was observed by Heger (1919b) in the spectra of two binary stars, β Scorpii and δ Orionis. Heger expected all absorption lines to oscillate back and forth as the stars orbited one another due to an effect known as Doppler shifting. To her surprise, she found sodium and calcium lines in the spectra that remained stationary, regardless of the motion of the stars (Fig. 1.4). She explored several possible explanations for this "peculiarity," eventually suggesting that "the effect is caused by an absorbing cloud of calcium vapor stationary in space between the binary star and the observer" (Heger 1919a). This hypothesized immobile "cloud of vapor in the line of sight" turned out to be the ISM (Heger 1919b).

The region of ISM within $\sim$ 100 parsecs of the Sun is specifically referred to as the local interstellar medium (LISM). The LISM is a complex and rich environment that shapes the heliosphere, and is in turn shaped by external forces like nearby supernovae and shocks. The Solar System is located in the Orion-Cygnus spiral arm of the Milky Way, approximately 8 kpc from the Galactic center (VERA Collaboration et al. 2020), but on a more detailed scale, where do

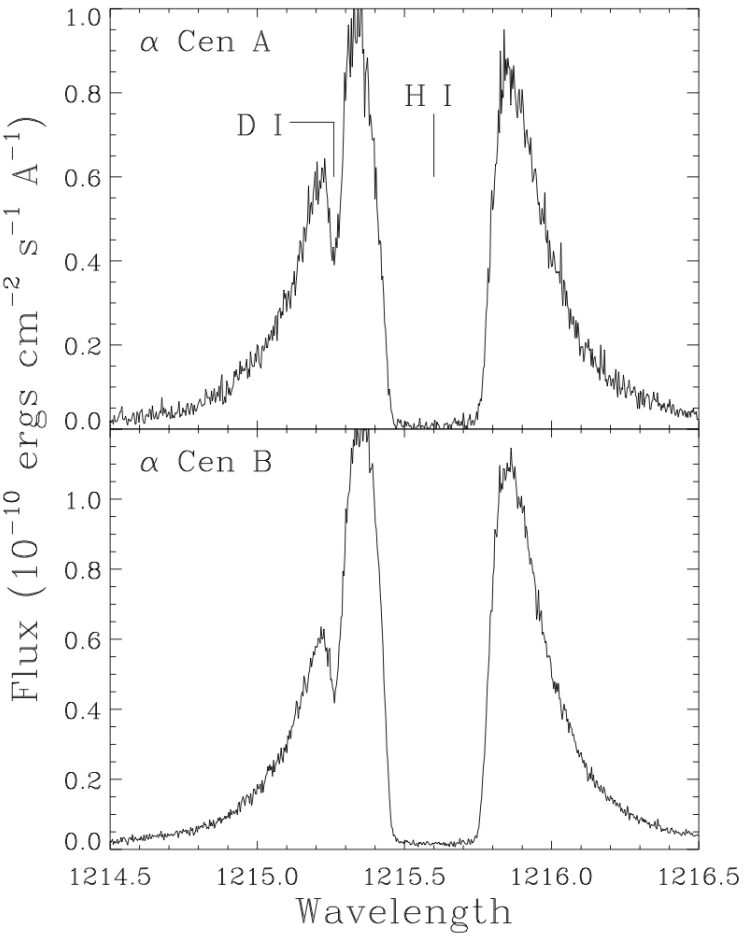

Figure 1.2: Goddard High Resolution Spectrograph (*Hubble Space Telescope*) spectra of the Lyα lines of α Centauri A and B, showing broad absorption from interstellar neutral hydrogen (HI) and narrow absorption from deuterium (DI). (Image: Linsky & Wood (1996).)

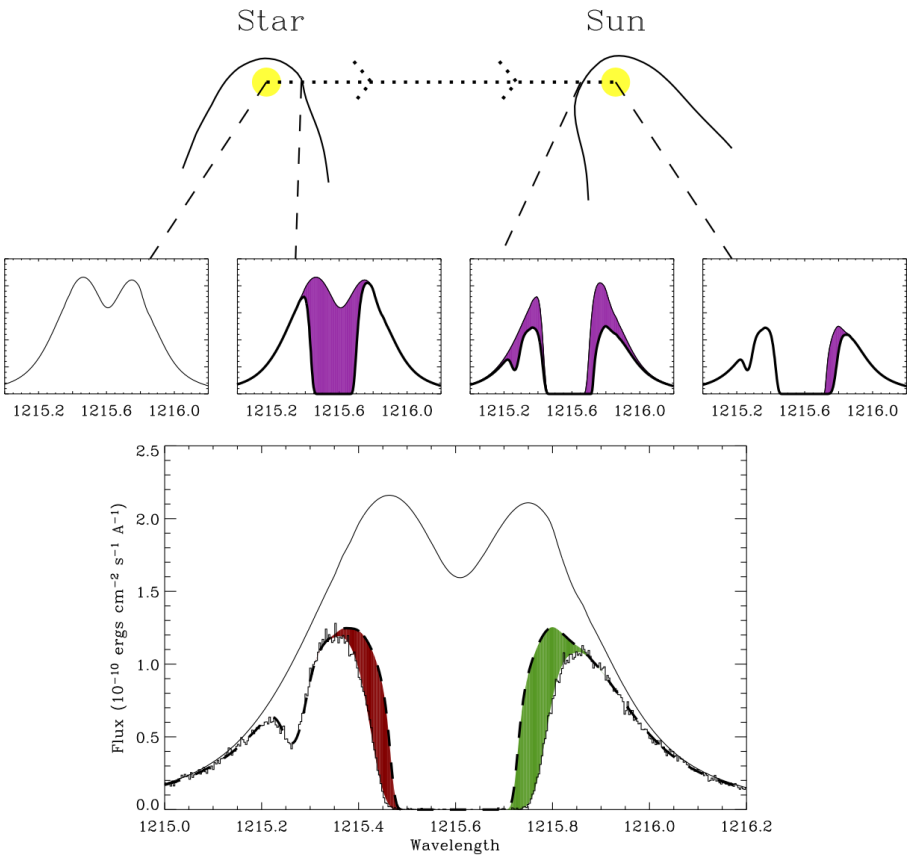

Figure 1.3: Schematic diagram showing how a Lyα absorption line profile changes from its initial appearance at the star and then through various regions (the stellar astrosphere, the LISM, and the heliosphere) that absorb parts of the profile before it reaches an observer at Earth. The lower plot shows the actual observed Lyα profile of α Centauri B. The upper solid line is the assumed stellar emission profile and the dashed line is the ISM absorption alone. The excess absorption is due to heliospheric H I (green shading) and astrospheric H I (red shading). (Image: Wood (2004).)

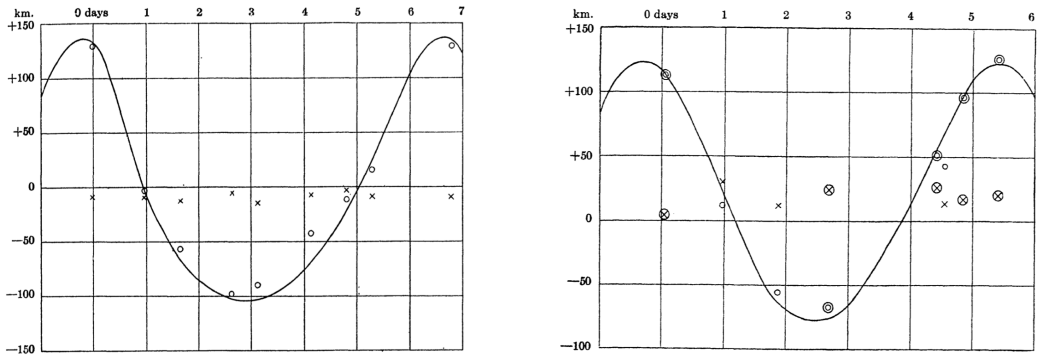

(a) Velocity curve of β Scorpii. **(b)** Velocity curve of δ Orionis.

Figure 1.4: Velocities of various absorption lines from two stars in a binary system charted over time. Small circles indicate the velocities of the oscillating absorption lines from the stellar spectrum. Small crosses are the mean velocities of sodium lines. Symbols inside larger circles represent values averaged across two observations made on the same night. Most absorption lines follow the velocity curves (solid lines) of the stars throughout their orbits; the sodium lines, however, remain relatively constant in velocity, indifferent to the motion of the stars, indicating the presence of a stationary cloud of gas between the stars and Earth. (Image: (Heger 1919b).)

we really reside? What is taking place in the solar neighborhood? Surprisingly, clouds get harder to study the closer they are. When we look farther out in space, there is more ISM in our line of sight, providing stronger absorption features that are easier to observe, although this can also muddy the waters because we may confuse the absorption features from local clouds with more distant clouds. But when we try to gaze at our immediate environs, the number of stars dwindles, resulting in a patchy sampling of the sky from which conclusions are difficult to draw.

Studies have shown that the Sun resides within a vast, low-density ($n \sim 0.05$ cm^{-3}), bubble-like region of hot ($T \sim 10^6$ K) ionized plasma, surrounded by a surface of cold, neutral gas and dust roughly 100 pc in radius (Frisch & York 1983; Breitschwerdt 1998; Streitmatter & Jones 2005; Zucker et al. 2022). Zucker et al. (2022) argue this "Local Bubble" likely originated from a supernova explosion

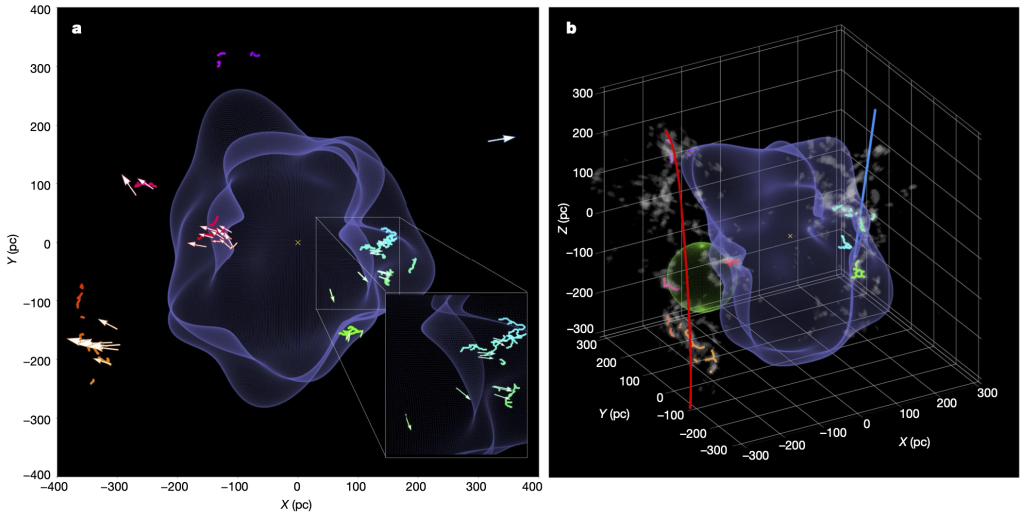

Figure 1.5: Left: A top-down projection of the surface of the Local Bubble (purple) in relation to nearby star-forming regions. The morphology of dense gas in nearby molecular clouds is indicated by short squiggly colored lines. 3D arrows mark the positions of young stellar clusters and their direction of motion. The Sun is demarcated by a yellow cross. **Right:** A 3D view of the relationship between the Local Bubble (purple), prominent nearby star-forming regions, and Galactic structure. Overlaid on the Local Bubble are models of 3D dust (grey blobs) and two Galactic scale features – the Radcliffe Wave (red) and the Split (blue). The Per-Tau Superbubble (green) is also shown. (Image: Zucker et al. (2022).)

∼14 Myr ago that swept up the ISM into an outward-moving shell while clearing out the central region. As the bubble expanded, the outer shell encountered inhomogeneities and turbulence, causing it to fragment, cool, and collapse into large molecular clouds. Nearly all nearby regions of star formation are located in the cool clouds on the bubble's surface, as mapped in Figure 1.5. The Sun has not always been inside the Local Bubble, but rather they intercepted each other on their respective orbits around the center of the Milky Way. Preliminary evidence suggested the Sun first entered the bubble roughly 5 Myr ago (Zucker et al. 2022). In the warm, diffuse gas inside the bubble, distinct ISM structures have been identified, and it is these structures with which this thesis concerns itself.

1.2 LISM Clouds

The distribution of interstellar gas and dust is not homogeneous across the cosmos, nor within the Local Bubble. At every scale, the ISM exhibits its own landscape; or rather, since we are referring to a terrain of gas, we might more aptly call it a *cloudscape*. In this context, we use the term "cloud" to refer to a region of ISM with similar physical properties that is moving with a coherent motion and has a distinct spectroscopic signature.

1.2.1 Cloud-spotting

Classic ISM models (McKee & Ostriker 1977; Wolfire et al. 2003) assumed the ISM was in thermal equilibrium, in one of three steady states: cold neutral medium ($T \leq 50$ K), warm neutral or ionized medium ($T \sim 8000$ K), or hot ionized medium ($T \sim 1,000,000$ K). These early models took into account the

cooling and heating of ISM clouds, but did not include gas flow nor predict cloud dimensions. Frisch et al. (2011) reports a mean LISM column density toward stars within 10 pc of 17.91 ± 0.18 logN(H I) cm^{-2}. Recent estimates of particle number density in the LISM are around 0.1 n(H I) cm^{-3} (Wood et al. 2005). Such low densities leave the LISM susceptible to being pushed out of equilibrium by stellar winds and supernovae, suggesting that the picture is far from static (Zucker et al. 2022). A classic diagram from McKee & Ostriker (1977) is reproduced in Figure 1.6, showing a supernova shock passing over a terrain of spherical ISM clouds and deforming their morphologies.

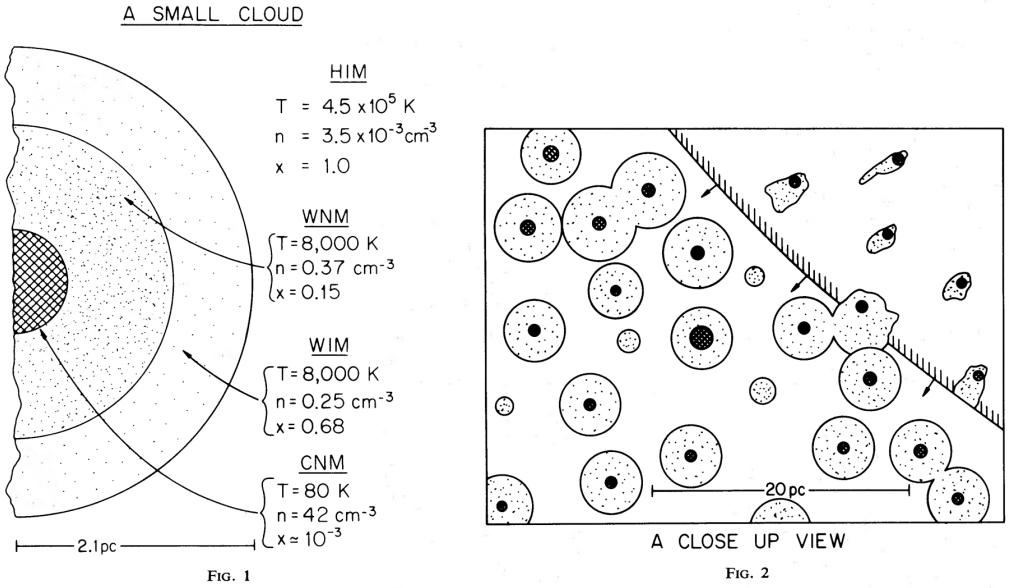

Figure 1.6: Left: An ISM cloud is shown in cross section. The cold core of neutral gas (CNM) is surrounded by a warm neutral medium (WNM) and an ionized outer layer (WIM). The cloud is surrounded by hot, ionized inter-cloud medium (HIM). Typical values of hydrogen density (n), temperature (T), and ionization ($x = n_e/n$) are indicated. **Right:** A zoomed out 30 × 40 pc schematic of spherical ISM clouds, with neutral cores ranging in size from 0.4 to 1 pc and warm envelopes of ∼ 2.1 pc. A supernova shock front arrives from the upper right, compressing and distorting the envelopes of clouds as it passes. (Image: McKee & Ostriker (1977).)

The first two LISM structures to be identified in the 1980s were the Anti-

Galactic (AG) and Galactic (G) Clouds, named for their respective directions towards or away from the Galactic center (Lallement & Bertin 1992). These clouds are now known as the Local Interstellar Cloud (LIC) and G Cloud. The number of clouds continued to tick upwards throughout the '90s, eventually comprising seven clouds within 12 pc of the Sun by the early 2000s (Lallement et al. 1995).

Redfield & Linsky (2008) expanded upon this foundation by using a much larger data set to create an empirical model of the LISM and its dynamics, ultimately mapping 15 distinct clouds. A single-cloud model was proposed (Gry & Jenkins 2014, 2017) but further observations (Malamut et al. 2014; Redfield & Linsky 2015) lent greater evidence for the Redfield & Linsky (2008) model, and it remains a widely-accepted model today. In their pivotal study, Redfield & Linsky (2008) used the *Hubble Space Telescope (HST)* to take UV observations of spectra from nearby stars along 157 distinct sight lines. Absorption lines in the stellar spectra revealed the presence of an absorbing gas medium along the line of sight between *HST* and the stars. They obtained 270 radial velocity measurements from the Doppler shifts of the spectral lines, which allowed them to determine the motion of the absorbing media for each sight line. When multiple stars across space exhibited absorption spectra with identical velocity vectors, this indicated that the same body of gas was moving in front of them. From here, the outlines of potential clouds began to take shape.

With measurements from 157 sight lines, Redfield & Linsky (2008) represented the most comprehensive sampling of the entire sky to date. This allowed them to finally "connect the dots," sketching boundaries around regions where all sight lines showed evidence of an interceding media with a consistent column density and velocity (to within ± 1 km s^{-1}, which was comparable to the spectrograph's precision). The authors defined these regions as LISM clouds. In attributing ab-

sorption lines to ISM clouds, they assumed the only thing causing absorption was the LISM. They determined that the probability of the spectrum being contaminated from edge-on disks that might be surrounding these stars was low enough to ignore. Furthermore, they constrained the upper limit of the distance to each of the clouds by using the distance to the closest star exhibiting absorption for that cloud, and thus determined all clouds to be within 15 pc of the Sun. In all, they identified three-dimensional (3D) velocity vectors for 15 warm LISM clouds within 15 pc, including LIC and G, which had been defined earlier by Lallement & Bertin (1992) and Lallement et al. (1995). Redfield and Linsky used five times the data to derive similar results for LIC and G Cloud velocity vectors as the 1990s estimates, which showed both that their method was reliable, and that one ultimately does not need many lines of sight to find a cloud (Swaczyna et al. 2022).

Figure 1.7 shows a galactic projection of the boundaries of the LISM clouds found in Redfield & Linsky (2008). One third of the clouds appear filamentary, although the authors admit this appearance may be exaggerated due to low spatial sampling. It is possible some of the compact clouds are also filamentary, but are projected from an angle where they appear compact; however, it is unlikely that all compact clouds fall under this scenario. The filaments are not similarly oriented, which suggest their cause is not a global magnetic field. Most filaments trace boundaries between the LIC and G Cloud, possibly indicating cloud-cloud interactions and shock collisions.

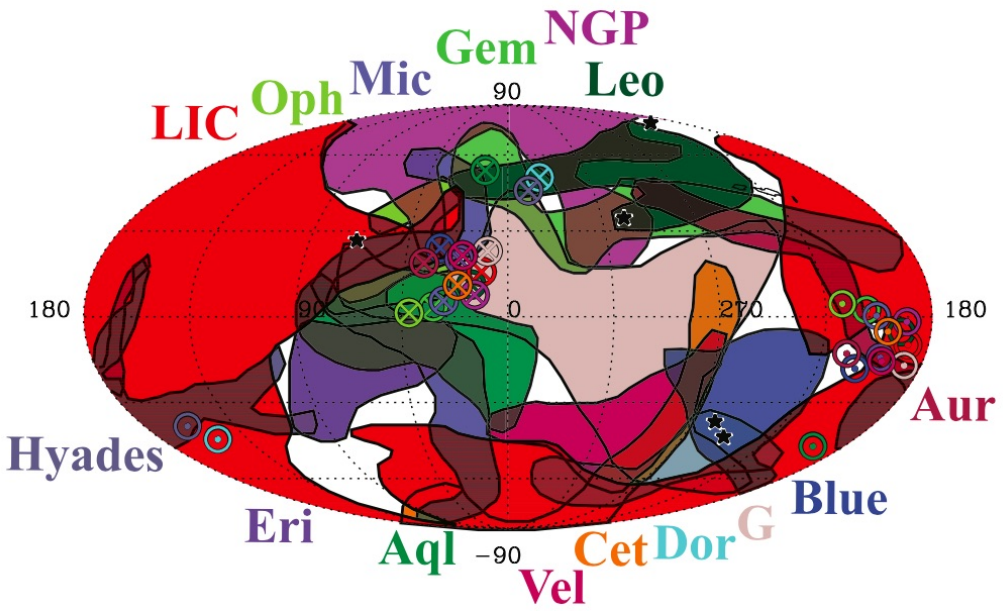

Figure 1.7: Map of the 15 LISM clouds within 15 pc of the Sun in galactic coordinates, known fondly as the *Psychedelic Easter Egg*. Color is used simply to distinguish clouds from one another. The direction of the velocity vector for each cloud is indicated by $\odot$ and $\otimes$. Star symbols indicate the locations of radio scintillation sources, which may be the result of turbulence caused by interactions between clouds. (Image: Redfield & Linsky (2008).)

1.2.2 Properties

The names given to the 15 clouds are either historical (e.g., LIC: McClintock et al. (1978); G: Lallement & Bertin (1992); Blue: Gry et al. (1995); Hyades: Redfield & Linsky (2001); north Galactic pole [NGP]: Linsky et al. (2000)) or derived from the International Astronomical Union constellation that the cloud's line of sight falls within.

In addition to finding the velocity vectors of each cloud, Redfield & Linsky (2008) obtained additional data for 1/3 of the sample (90 components), including temperature, turbulent velocity, and metal depletions. This allowed them to make initial characterizations of the kinematic, morphological, and physical properties

of the clouds.

The clouds all have sizes of < 6 pc. Most clouds were found to be moving parallel to the flow of the Scorpio-Centaurus association, perhaps driven by a supernova in that direction (Starecheski et al. 2023). Some clouds had quite disparate velocities, even reaching supersonic differences, which the authors suggest could produce shocks. Of the clouds that they obtained physical properties for, all were found to be warm, with average temperatures ranging from $5300 - 9900$ K, however large uncertainties were noted. The authors further estimated that these warm, partially ionized gas clouds fill $5.5 - 19\%$ of the volume within 15 pc of the Sun.

Table 1.1 lists the physical properties of the 15 LISM clouds obtained by Redfield & Linsky (2008), including temperature, projected surface area, distance upper limit, coordinates of the cloud center, turbulent velocity, and depletion of iron and magnesium. These properties were not found to correlate with any particular cloud morphology.

1.2.3 Assumptions & Limitations

We adopt the LISM cloud map created by Redfield & Linsky (2008), and their definition of a "cloud" as "a contiguous parcel of interstellar gas inside the LISM with homogeneous kinematical and physical properties." Although clouds are not rigid bodies, for the purpose of this study, we will assume the gas inside each cloud has coherent flow and is bounded by a sharply defined edge. We will also assume the H I cloud density is constant throughout each cloud. For most lines of sight within clouds, few to no measurements have been obtained of their physical properties, so it is difficult to assess whether properties vary across an

Summary of LISM Cloud Properties

Cloud Name	Number of Sight lines	l [deg]	b [deg]	Closest Star [pc]	Surface Area [deg^2]	$\langle$T$\rangle$ [K]	$\langle \log N(\mathrm{H\,I}) \rangle$ [cm^{-2}]	Morphology
LIC.....	79	170	−10	2.6	18270	7500 ± 1300	17.9	Compact
G.....	21	315	+00	1.3	8230	5500 ± 400	17.8	Compact
Blue.....	10	250	−30	2.6	2310	3900 ± 2300	18.1	Compact
Aql.....	9	40	−05	3.5	2960	7000 ± 2800	17.5	Compact
Eri.....	8	70	−20	3.5	1970	5300 ± 4000	17.9	Compact
Aur.....	9	210	+10	3.5	1640	(6710)	17.7	Filamentary
Hyades.....	14	180	−20	5.0	1810	6200 ± 3800	17.7	Filamentary
Mic.....	15	40	+15	5.1	3500	9900 ± 2000	17.4	Filamentary
Oph.....	6	45	+25	5.1	1360	(1700)	(17.5)	Compact
Gem.....	10	300	+40	6.7	3300	6000 ± 1100	17.8	Filamentary
NGP.....	15	5	+75	8.5	4020	8000 ± 600	18.0	Compact
Leo.....	7	270	+55	11.1	2400	...	(18.6)	Compact
Dor.....	4	270	−50	11.7	1550	(7000)	(18.1)	Compact
Vel.....	7	300	−45	14.9	2190	(10600)	18.5	Compact
Cet.....	5	290	−40	15.5	2270	(6300)	(18.5)	Filamentary

Table 1.1: Properties of the 15 LISM clouds within 15 pc of the Sun, provided by Redfield & Linsky (2008). Clouds are listed in order of their proximity to the Sun, with distance estimated according to the closest star in which absorption from the cloud is observed. Although G is observed in the spectrum of a closer star, other studies indicate the Sun is inside (or just exiting) LIC, hence LIC is listed first. This table gives galactic coordinates for the center of each cloud (l, b), surface area, average temperature, and morphology. The weighted average column density has been calculated as the log of the number of neutral hydrogen atoms per square-centimeter. Those clouds with only one sight line with a physical measurement are indicated in parentheses; since a weighted average is not possible, the listed properties should be considered uncertain.

individual cloud. Observations of binary stars show that small-scale variations are not occurring (e.g., α Centauri; Wood et al. 2001), corroborated by 18 closely spaced observations of Hyades stars that do not vary significantly (Redfield & Linsky 2001). As a result, each cloud is assumed to be fairly homogeneous, or slowly varying.

We put an upper limit on the distance to each cloud based on the nearest star that shows absorption in its spectrum consistent with the cloud's velocity vector. The presence of absorption lines indicates the cloud must be in front of said star, although it may extend further in either direction, and even surround the star. As we are unable to precisely determine the depth of the clouds, we treat each cloud as a solid slab located at its upper distance limit.

In Redfield & Linsky (2008), the threshold for identifying a cloud was having at least four measurements that were adjacent spatially. Although clouds could have more complex shapes, this limited the definition of a cloud to having spatially coherent, contiguous structure. Out of all the radial velocities they obtained, 81.2% were determined to be attributable to these 15 clouds; 18.8% of components did not fit with any cloud's velocity vector. 90% of the 51 unassigned components are from stars farther than 15 pc, and only 5 are within 15 pc. The authors suggest the unassigned components may be due to smaller or more distant clouds that did not yield enough data points to make meaningful accounts of.

Redfield & Linsky (2008) note there remain significant regions of poor sampling. Their methods are most sensitive to finding nearby clouds with large projected surface areas. To characterize this observational bias, they ran simulations that estimated $14.5 - 21.5\%$ of clouds would not be detected using their methods, which matches with the 18.8% of sight lines that were ultimately not assigned in the data.

In Redfield & Linsky (2008), the volume filling factor of the warm, partly ionized gas in the LISM is estimate to be 5.5 - 19%. To make this estimate, they assume all warm LISM is within 15 pc of the Sun. Even though the Local Bubble extends to ~ 100 pc, most warm gas appears to be close to the Sun (Zucker et al. 2022; Lallement et al. 2003). They also assume all warm LISM clouds are similar in size (radius 1.5 pc) and hydrogen density (0.2 cm^{-3}) to the LIC. Under these constraints, simulations estimated volume filling factors of $5.5 - 19\%$. In recent years, it has been determined that the clouds may be more diffuse (closer to 0.1 cm^{-3}), which means the clouds must be bigger to achieve the desired column density, so they may fill most of the volume (Linsky et al. 2022).

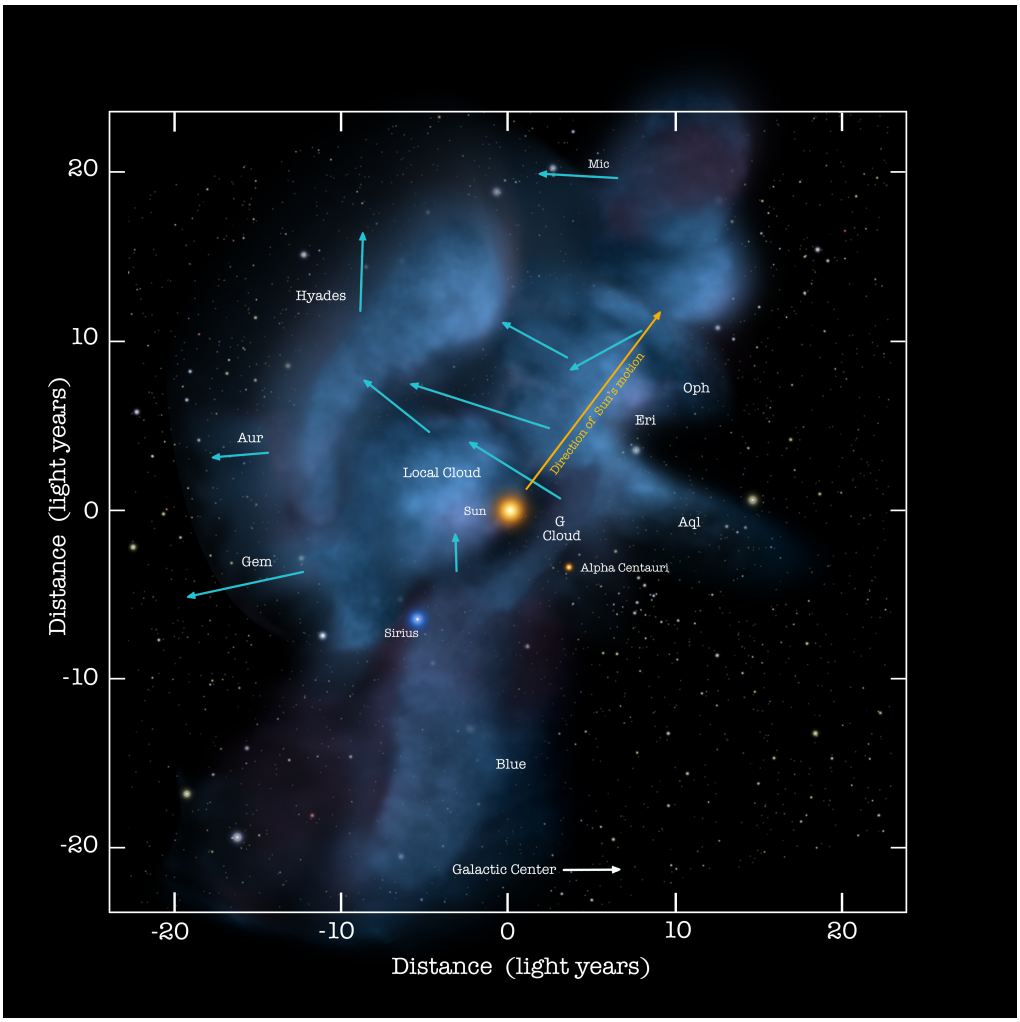

Figure 1.8: This two-dimensional (2D) artist's depiction of the LISM shows the rough directions, distances, and velocity vectors of the LISM clouds. The Sun is currently moving through an interaction zone between the LIC and G Cloud. (Image: Redfield / NASA / Goddard / Adler / University of Chicago / Wesleyan.)

1.2.4 Ongoing Questions

Despite immense progress characterizing and mapping LISM clouds over the past several decades, the fine details of our spatial relationship to our environs remains contested. There is ongoing discussion as to whether measurements of the LISM flow vector indicate that the Sun is inside the LIC, at the edge of the

LIC moving into the G Cloud, or in a region of interaction between the two. Historically, the AG Cloud was renamed the LIC (Local Interstellar Cloud) based on a body of evidence suggesting the Sun was inside this cloud (Swaczyna et al. 2022). However, support is growing for the second and third propositions. Redfield & Linsky (2008) argue that the Sun is on the boundary between the LIC and G Cloud, because the temperature and velocity of interstellar gas flowing through the Solar System is intermediate in value between the LIC and G values (Möbius et al. 2004). Observations from the *Ulysses* space probe, the *Interstellar Boundary Explorer* (*IBEX*), and the *Solar Terrestrial Relations Observatory* (*STEREO*) indicate the density of the hydrogen ISM surrounding the Sun is two times higher than average and has a velocity that is a linear combination of the G Cloud and LIC velocities, providing evidence that the Sun resides not inside the LIC or G Cloud, but in a mixing zone between them (Swaczyna et al. 2022). The LIC and G Cloud are probably interacting with each other and other nearby clouds. Some LISM clouds (such as the highly turbulent, filamentary Mic Cloud) may be a result of those interactions. Three scintillating quasars and two pulsars are spatially coincident with cloud boundaries, with three out of five located on lines of sight that cross transitional regions of interaction between the LIC and G Cloud, whose turbulent collision may be causing the scintillation (Linsky et al. 2008).

We will find in the next section that questions of the environment in which the Sun resides have profound implications for the Solar System.

1.3 Heliosphere

The Sun is continuously in motion as it is gravitationally drawn on an orbit around the Milky Way. The Sun has likely circumnavigated the Milky Way more

than a dozen times in its lifetime, passing through numerous and diverse ISM environments on its journey, just as it is now passing through the LIC and G Cloud. These environments interact with the Solar System and are in turn shaped by the passage of the Sun, and these interactions are all mediated by the heliosphere (depicted in Fig. 1.9).

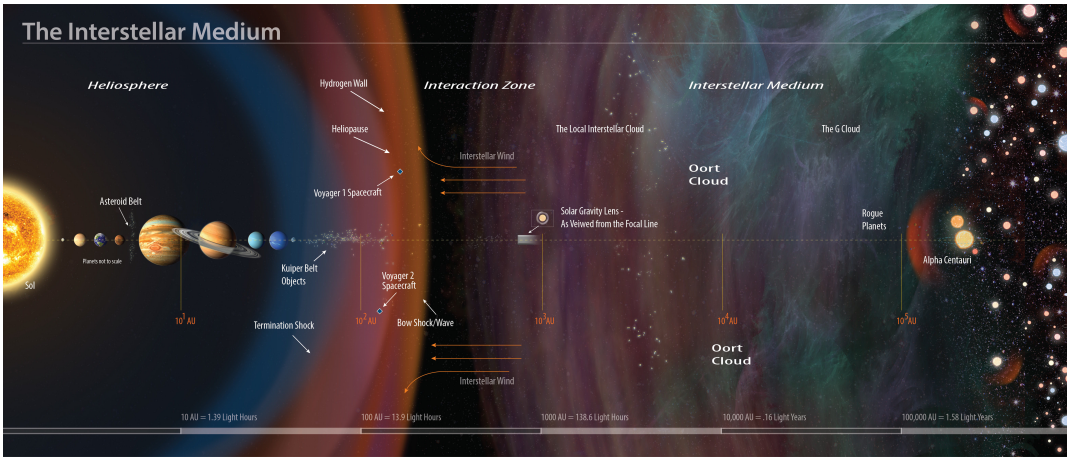

Figure 1.9: The heliosphere is defined as the boundary where the Sun's radiation meets the surrounding interstellar medium. The edge of this radiation-inflated bubble occurs around 120 au (Brandt et al. 2023), although the Sun's gravitational influence extends further into the Oort Cloud out to $10^4 - 10^5$ au. (Image: Chuck Carter / Keck Institute for Space Studies.)

The flow of charged particles released by the Sun is called the solar wind. This wind inflates a protective bubble in the LISM called the heliosphere that extends 100 au around the Sun (Parker 1958, 1961). The "edge" of the heliosphere is hard to pin down, but is generally defined as the boundary where the outward flowing solar wind is balanced by the pressure of the ISM gas we are moving through (Fig. 1.9). As a result, the morphology and size of the heliosphere is fundamentally shaped by the structure and properties of the ISM. Simulations predict the current shape of the heliosphere to be somewhere between a croissant and a comet-like bow shock with a tail (Fig. 1.10). Similar structures (called astrospheres) are

found around other stars, notably our closest neighbor, α Centauri (Wood et al. 2001, 2005). By observing other stars, we can extrapolate that the Sun's solar wind may have been 35 times stronger when it was young, 3.5 Gyr ago (Wood et al. 2005). ISM column densities can span six orders of magnitude, and this can have a strong impact on astrospheres. Even when density is constant, the dynamics of the ISM can act upon an astrosphere to sculpt it.

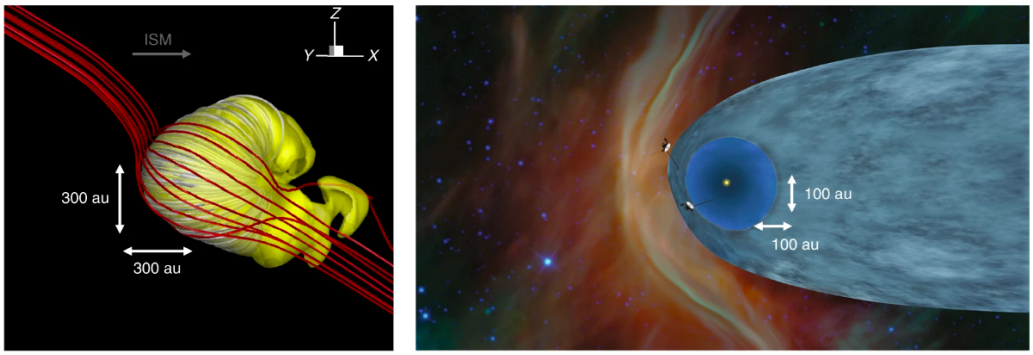

Figure 1.10: Left: Simulation showing a croissant-like heliosphere. The yellow surface is the heliopause, defined by a solar wind density of 0.0005 cm^3. White lines show the solar magnetic field. The direction of ISM flow is indicated at the top. **Right:** Artistic rendition of a comet-like heliosphere with a tail extending thousands of au. The locations of *Voyagers 1* and *2* are shown; *Voyager 2* has since passed the heliopause. The innermost blue sphere indicates the region dominated by the supersonic solar wind. The broader pale blue region is the heliosheath. (Left image: Opher et al. (2020); Right image: NASA/JPL-Caltech.)

Although largely shielded from the LISM, the region within the helisophere is not devoid of gas. It is filled with its own interplanetary medium (IPM), akin to the ISM, but mostly composed of dust grains from comets and Kuiper Belt objects from within the Solar System (Poppe 2016). The IPM generally begins declining in density exterior to 45 au, but fills the heliosphere up to the heliopause (Poppe 2016). Solar radiation flowing outwards from the Sun is continually deflected by dust particles in the IPM, which readily scatter Lyα photons. This creates a fog from which our telescope, *New Horizons*, needs to escape if it is to observe any

emission beyond the Solar System.

1.4 Exploration

The main challenge with exploring the outer Solar System is that of distance, and consequently, time. Since space exploration began in earnest in the 1950s, few missions have had time to travel the vast distances required to reach the outer Solar System. The distance from the Sun to Earth is a relatively cozy 93 million miles (1 au) when compared with the orbit of the farthest planet, Neptune, out at nearly 3 billion miles (30 au) from the Sun. Both are minuscule in comparison to the size of the heliosphere as a whole, the edge of which fluctuates somewhere around 123 au. If a planet circled the Sun at the edge of the helisophere, the weakness of the Sun's gravity would slow its orbit down to a crawl, and people on this distant world would celebrate their birthdays only once every 1,364 Earth-years. The fastest trains on Earth, traveling up to ∼280 mph, would take around 4,700 thousand years to cross that chasm.

The first attempts to reach the heliosphere's edge were *Pioneer 10* and *11*, NASA missions that launched in 1972 and 1973 respectively, with primary objectives of visiting Jupiter and Saturn. Due to declining power to their detectors and antennae, *Pioneer 11* was decommissioned in 1995, and *Pioneer 10* lost contact with Earth in 2003 at 80 au. They were ultimately overtaken by the *Voyager* spacecrafts, both launched in 1977, and which successfully crossed the heliopause in 2012 (*Voyager 1*; Webber & McDonald 2013) and 2018 (*Voyager 2*; Krimigis et al. 2019) respectively. The successor to these flagship NASA missions is *New*

[2]Giorgini, JD and JPL Solar System Dynamics Group, NASA/JPL Horizons On-Line Ephemeris System, `https://ssd.jpl.nasa.gov/horizons/`

[3]Creative Commons Attribution-ShareAlike 4.0 International License, `https://creativecommons.org/licenses/by-sa/4.0/`

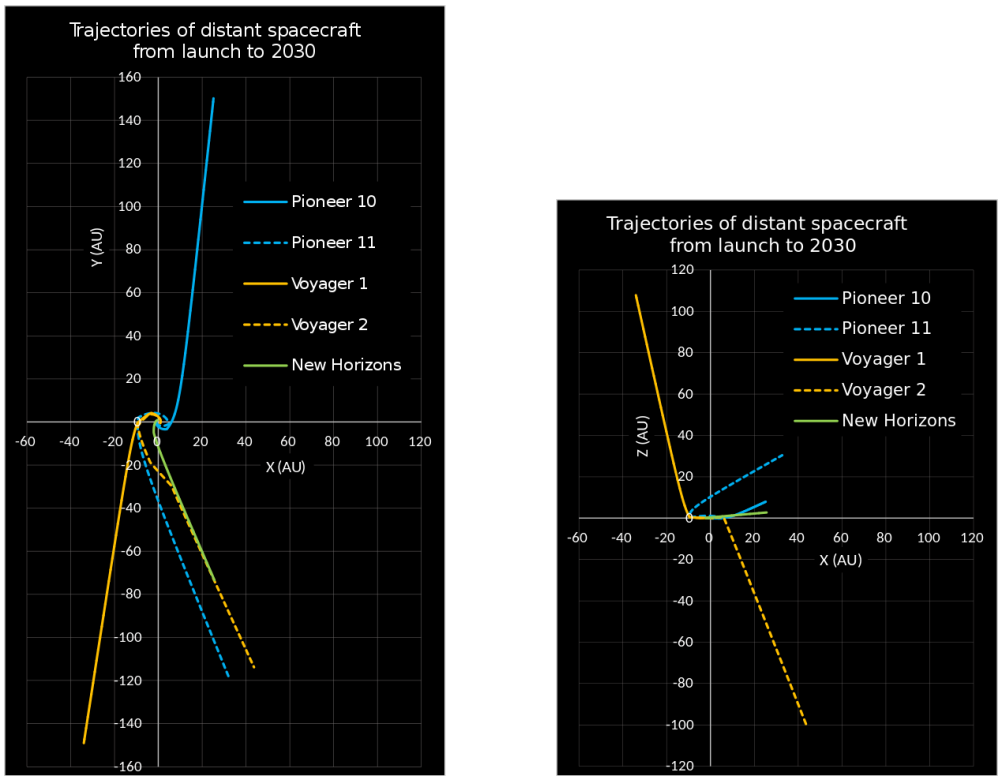

(a) Polar view. **(b)** Equatorial view.

Figure 1.11: Trajectories of artificial objects leaving the Solar System. Data is from the NASA/JPL Horizons On-Line Ephemeris System[2] (Giorgini et al. 1996; Giorgini & Yeomans 1999; Giorgini et al. 2001). (Image: Phoenix7777[3]).

Horizons, a smaller-scale mission launched in 2006 through the New Frontiers program, aimed at exploring Pluto and objects in the Kuiper Belt with more specialized instruments. *NH* is currently at 58 au and projected to begin approaching the termination shock in the next several years. Now that the *Pioneers* and *Voyagers* have left the heliosphere, *NH* is the only mission currently operating in the outer Solar System (Bagenal et al. 2023).

1.4.1 *Voyager* Missions

Voyager 1 and *Voyager 2* were two identical spacecraft launched in 1977, set to do the first close-up observations of Jupiter and Saturn. *Voyager 1* launched a couple weeks after *Voyager 2* and achieved a higher launch velocity, which resulted in *Voyager 1* overtaking *Voyager 2* within the first few months after launch (Stone 1981).

Both spacecraft were initially outfitted with a 12-foot radio dish and a suite of instruments, including cameras, a magnetometer, a plasma spectrometer, and instruments to measure low-energy charged particles, cosmic rays, and plasma waves (Voy 1977). As the first spacecraft since the *Pioneers* set to exit the Solar System, the *Voyagers* also carried with them two golden records (Fig. 1.12) upon which were etched greetings, music, and images from Earth, in case of interception by extraterrestrials in the distant future.

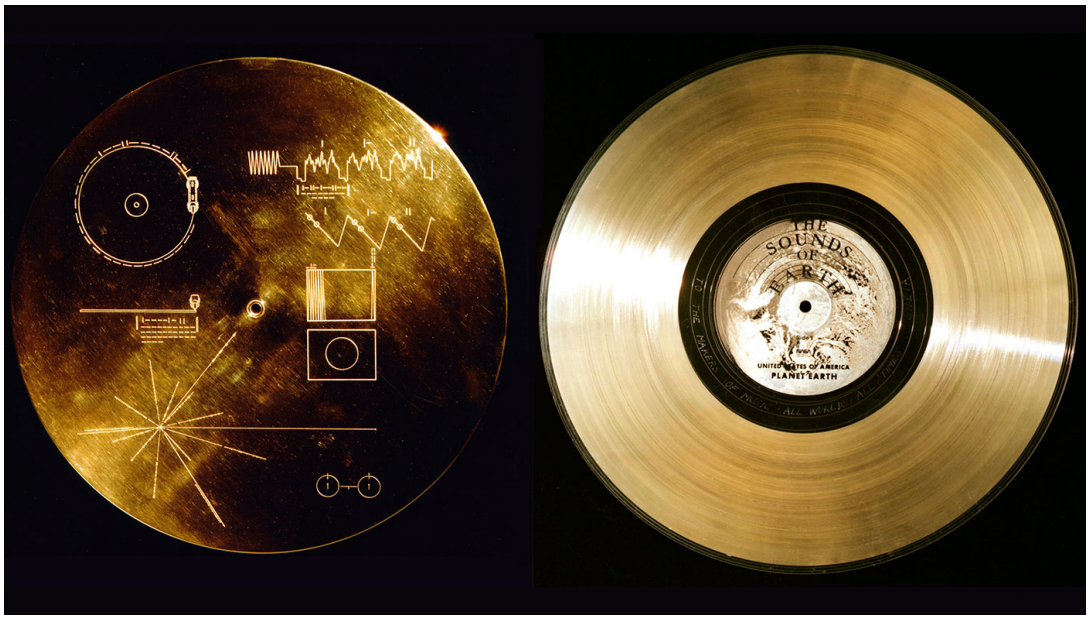

Figure 1.12: The Golden Records carried by *Voyagers 1* and *2*, 12-inch gold-plated copper disks engraved with sights and sounds of Earth. These records contained natural sounds, music, and greetings in 55 human languages – a hopeful hand extended to any extraterrestrial life that might encounter them in the future. (Image: NASA/JPL-Caltech.)

The *Voyagers* revealed new details about the time evolution of Jupiter's atmosphere, particularly the orientation of the Great Red Spot and its interactions with other storms. They also made significant discoveries regarding Jupiter's moons, including finding the first active volcanoes beyond Earth (Io), hints of the first non-terrestrial ocean (beneath the icy striations on Europa), and establishing the largest moon in the Solar System (Ganymede) (Smith et al. 1979). They discovered new moons around Saturn and investigated Titan's thick nitrogen-rich atmosphere (Smith et al. 1981). *Voyager 1* reached Jupiter in 1979, Saturn in 1980, then headed out of the heliosphere, passing *Pioneer 10* in 1998. *Voyager 1* remains the furthest human-made object from Earth.[4] *Voyager 2*, instead, continued on to Uranus and Neptune. To this day, *Voyager 2* is the only mission to

[4]NASA Press Release, First and Farthest, `https://voyager.jpl.nasa.gov/news/details.php?article_id=49`, updated 2007-JUL-31

have visited Uranus (1985) and Neptune (1989), where it identified 11 new Uranian moons and spotted volcanoes on Neptune's satellite Triton, before it, too, traveled beyond the heliosphere (Smith et al. 1986, 1989).

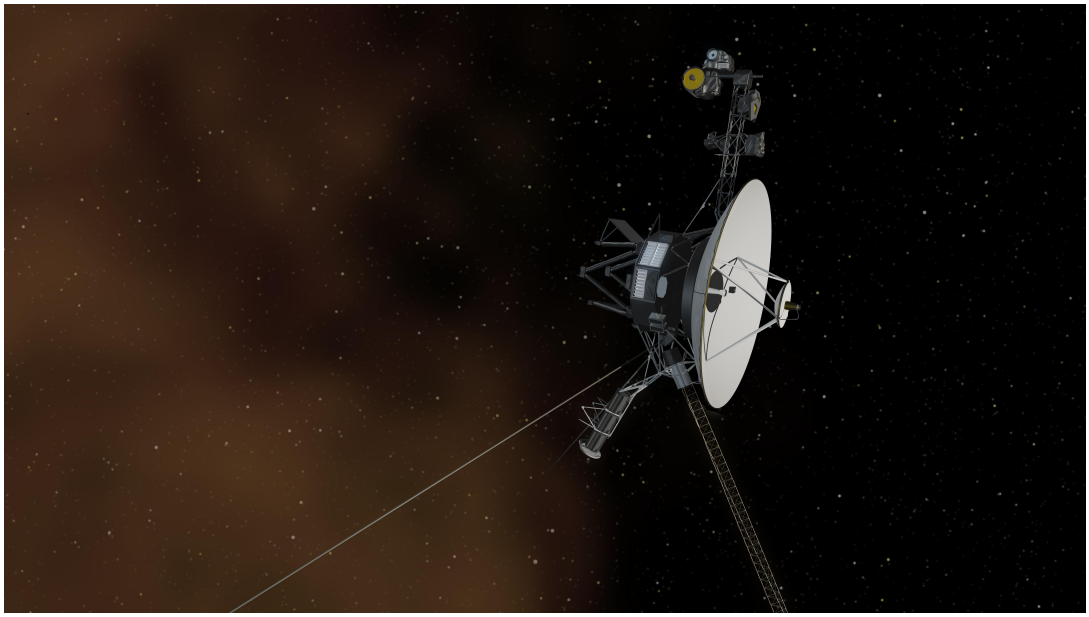

Figure 1.13: Artist depiction of the *Voyager 1* spacecraft entering the ISM gas clouds outside the heliosphere. The brown haze indicates the presence of interstellar gas species. The craft's high gain antenna points back towards the heliosphere as it transmits data to Earth. (Image: NASA/JPL-Caltech.)

The edge of the heliosphere is defined as the threshold at which the outward pressure of hot solar wind is balanced by the inward push of the much colder ISM, and is characterized by changes in plasma density and abundance of cosmic rays. *Voyager 1* exited the heliosphere in 2012 (Fig. 1.13), but the official announcement did not come until 2013 due to a broken plasma sensor that made the determination difficult (Webber & McDonald 2013). The ultimate determination was made thanks to a coronal mass ejection, which took 13 months to reach *Voyager 1* and then set the surrounding plasma oscillating. The *Voyager 1* team was able to use its plasma wave instrument to analyze these oscillations and infer

the density of the plasma, finding it to be 40 times denser than plasma in the heliosphere, a high density commensurate with interstellar space. The time frame of these oscillations aligned with abrupt changes in *Voyager 1*'s charged particle observations on Aug 25, 2012, which is now considered to be the date of the first human-made object's exit from the heliosphere (Stone et al. 2013). It was followed by *Voyager 2*'s heliospheric exit on November 5, 2018, as instruments onboard recorded the velocity of solar particles dropping to zero partnered with a marked increase in cosmic rays (Stone et al. 2019). The *Voyagers* were intended to last 5 years, long enough to conduct close-up studies of Jupiter and Saturn, but they have survived well beyond that lifetime. *Voyager 2* is NASA's longest running mission.

Although the *Voyagers* have left the heliosphere and passed beyond the influence of the solar wind, they have not yet left the gravitational influence of the Sun, which extends to the end of the Oort Cloud, a region populated by trillions of small icy bodies that are dragged around the Sun on periods that last hundreds of thousands of years (Oort 1950). The Oort Cloud's dimensions are not precisely known, but may reach from around 1,000 to 100,000 au. It is estimated that the *Voyagers* may arrive at the inner edge of the Oort Cloud in 300 years, and take another 30,000 to cross it. The *Voyagers* are powered by radioisotope solar electric generators with 88-year half lives and are expected to stop communicating with Earth within the next decade, at which point they will continue their journeys alone.

The LISM clouds that are the subject of this thesis all lie within 15 pc of the Sun. To give a sense of scale, this corresponds to roughly 3 million au. After 46 years of travel, Voyager 1 is currently 163 au from the Sun, and Voyager 2 is following at 136 au. The seemingly immense Oort Cloud extends from around

1,000 to 100,000 au, which is only half a parsec from the Sun and less than halfway to the next nearest star. The *Voyagers* may currently be moving through the LIC or G Cloud, which the Sun appears to be embedded within, but will need to travel much longer before detecting changes in ambient gas properties indicative of entering other LISM cloud structures. This could take millennia, long after the *Voyagers*' power sources have gone dark. However, even before the *Voyagers* reach the LISM clouds, we could potentially image them using *New Horizons*.

1.4.2 *New Horizons* Mission

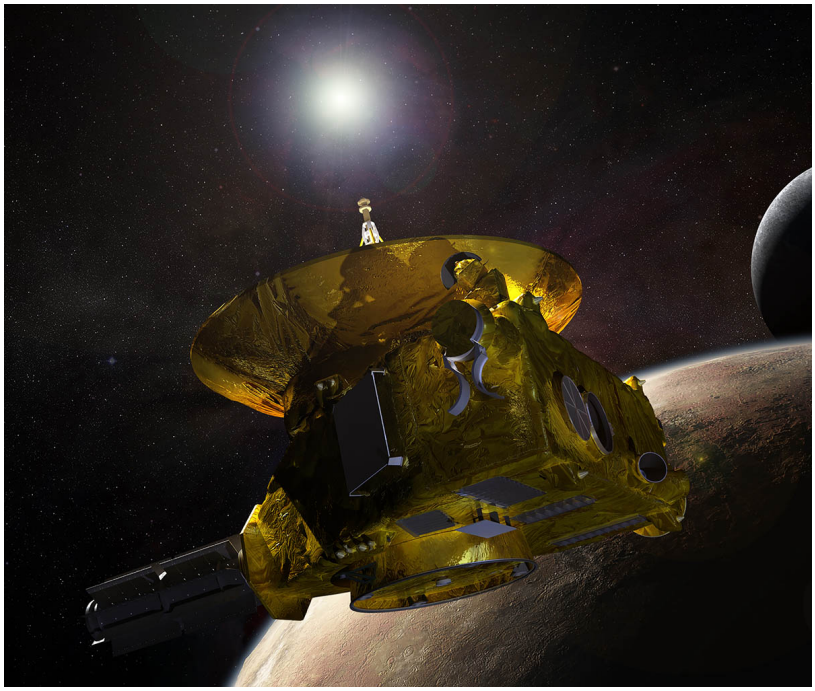

Figure 1.14: Artist's rendition of *New Horizons* approaching Pluto. *New Horizons* is a spacecraft originally designed to conduct the first flybys of Pluto and a Kuiper Belt object. It is currently conducting its second extended mission from its location in the outer Solar System at 58 au. (Image: Johns Hopkins APL.)

New Horizons follows in the footsteps of the *Voyager* missions. In 2003, the National Academies' *New Frontiers in the Solar System* decadal survey called

for a planetary mission to examine the Pluto-Charon system up close, and *New Horizons* (*NH*) answered the call (Fig. 1.14).[5] The *NH* mission was designed by teams at the Southwest Research Institute (SwRI) and Johns Hopkins Applied Physics Laboratory (Johns Hopkins APL) to conduct the first flybys of Pluto and a Kuiper Belt object (KBO) (Stern & Spencer 2003). It launched January 19, 2006 on a Lockheed Martin Atlas V-511 rocket from Cape Canaveral Air Force Station in Florida. It made a lot of firsts, including being the first Principal Investigator-led planetary mission, the first to include a student-designed instrument, and the first mission to an unexplored planet since the *Voyagers*.

Given the immense distance it had to traverse, at the time of its departure in 2006, it was the fastest spacecraft ever launched, moving nearly 100 times faster than a jetliner at 16 km s^{-1} after launch.[6] It reached the Moon in a mere nine hours (compared to the three days it took the Apollo missions) and surpassed Jupiter within 13 months (compared to four years for *Cassini* and six years for *Galileo*). At Jupiter it received a gravity assist that boosted its speed by 20%, shortening its trip to Pluto by more than 3 years (Weaver 2018).

[5]New Frontiers in the Solar System: An Integrated Exploration Strategy, `https://nap.nationalacademies.org/catalog/10432/new-frontiers-in-the-solar-system-an-integrated-exploration-strategy`, updated 2003

[6]NASA, New Horizons: Launch Press Kit, `https://www.nasa.gov/pdf/139889main_PressKit12_05.pdf`, updated 2005-DEC-19

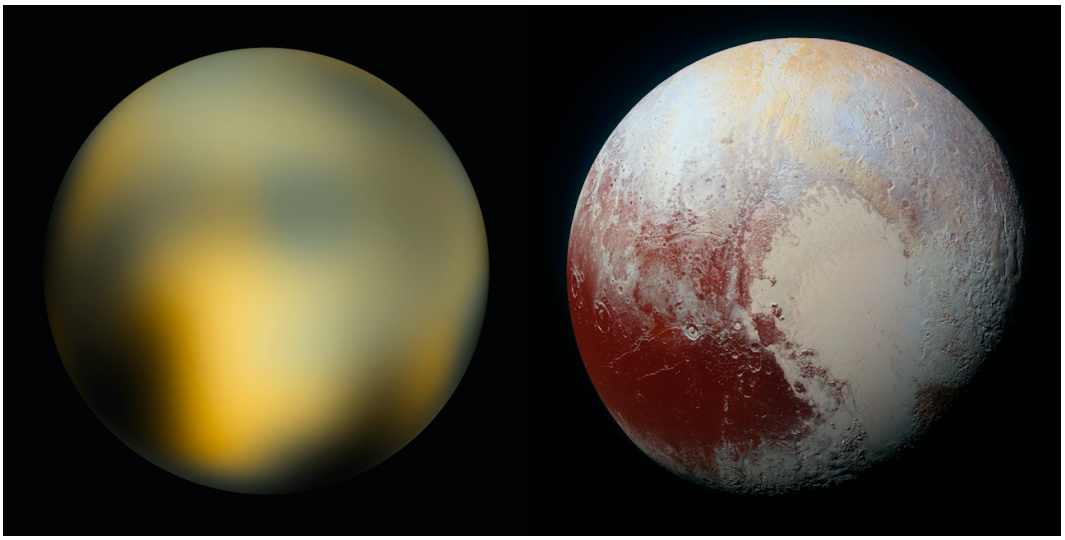

Figure 1.15: Left: Taken by Hubble in 2010, this was the best resolution optical image of Pluto prior to *New Horizons*. (Image: NASA/JHUAPL/SWRI.) **Right:** Image of Pluto taken by *New Horizons* during the 2016 flyby, ∼12,500 meters above the dwarf planet's surface. (Image: NASA/ESA/M. Buie SWRI.)

NH is powered by a radioisotope thermoelectric generator, contains numerous science instruments (including the Alice UV Spectrograph used in this thesis), and has an array of low, medium, and high gain antennas to communicate with Earth. It mostly hibernated during its 11-year journey from Jupiter to Pluto, awake only for 50 days per year for annual checkouts (ACOs) to calibrate instruments and perform minor course corrections. When *NH* finally approached its first destination in 2015, it awoke to find Pluto was no longer considered a full-fledged planet! Despite Pluto's reclassification to dwarf planet, *NH*'s investigation of the Pluto-Charon system provided pivotal insight into the atmospheres, densities, and surface features of the unexplored, icy mini-worlds of the outer Solar System (Fig. 1.15) (Stern et al. 2015). After studying Pluto-Charon and their two moons, Hydra and Nix, *NH* was approved for an extended mission to the KBO 486958 Arrokoth, which it successfully reached in 2018 at 43 au (Stern et al. 2021). *NH*'s trajectory since launch is shown in Figures 1.16 and 1.17.

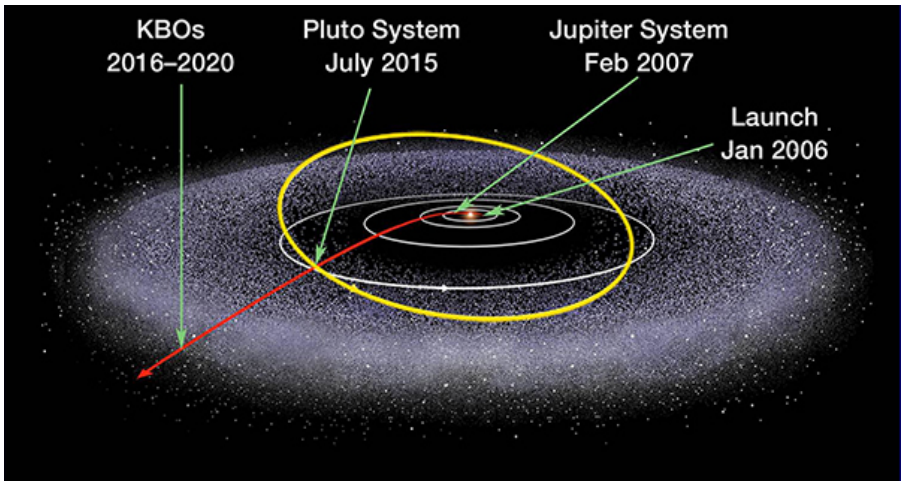

Figure 1.16: *New Horizons* launched from Cape Canaveral Air Force Station, Florida January 19, 2006. The spacecraft flew by Jupiter for a gravity assist in 2007, reached Pluto in 2015, and passed the Kuiper Belt object 486958 Arrokoth in 2018. *New Horizons* is currently the only mission operating in the outer Solar System. (Image: Johns Hopkins APL.)

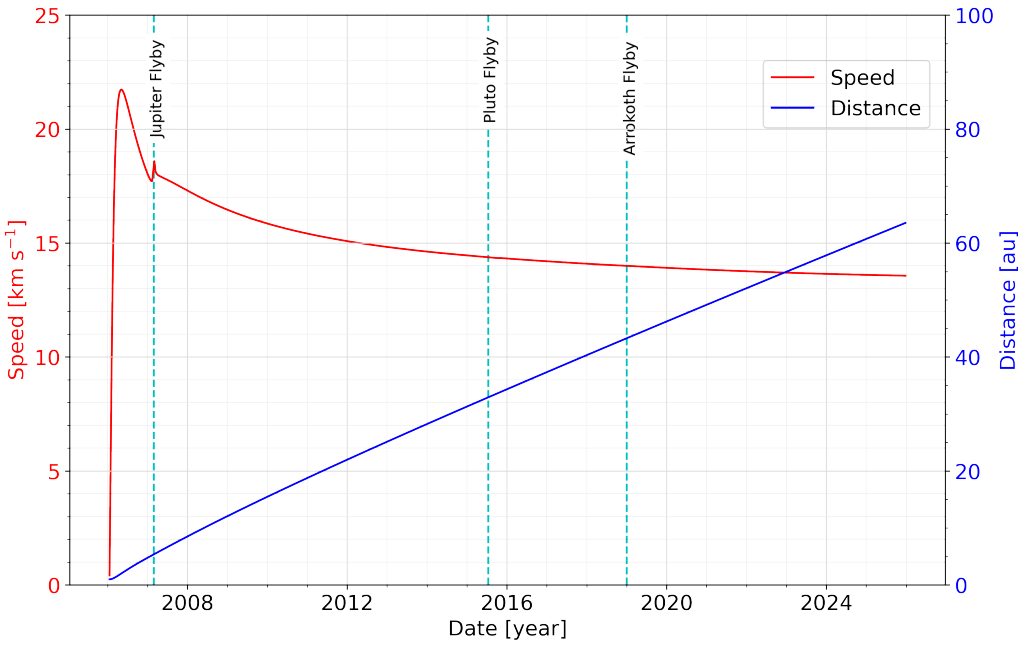

Figure 1.17: Trajectory of *New Horizons* spacecraft, with speed indicated in km s^{-1} by the red y-axis (left), and distance from the Sun shown in au on the blue y-axis (right). Major milestones are marked by dashed cyan lines. The NASA/JPL Horizons On-Line Ephemeris System[7] was used to project *NH*'s trajectory out to 2026 (Giorgini et al. 1996; Giorgini & Yeomans 1999; Giorgini et al. 2001).

It was initially projected that the farthest operating range of *NH*'s antennas would be 55 au, but *NH*'s longevity has surpassed all expectations. It is known that velocity measurements of the solar wind drop off at the termination shock – the threshold where the pressure of ISM slows the solar wind down from supersonic – although the solar wind continues all the way out to heliopause, where it is finally halted by the ISM. *NH* is traveling in the plane of the ecliptic with the same initial longitude as *Voyager 2*. *Voyager 2* started measuring an uptick in upstream ions around 60 au that preceded the termination shock. As *NH* is currently at 58 au, it is expected that *NH* may be getting close to the ramp up to the termination shock (Fig. 1.18). Given the current condition of its instruments, power supply, fuel, and comms range, *NH* is currently projected to run until 2050 and perhaps longer, continuing its journey to the edge of the heliosphere, and perhaps beyond (Stern 2023).

[7]Giorgini, JD and JPL Solar System Dynamics Group, NASA/JPL Horizons On-Line Ephemeris System, `https://ssd.jpl.nasa.gov/horizons/`, data retrieved 2023-JUN-14

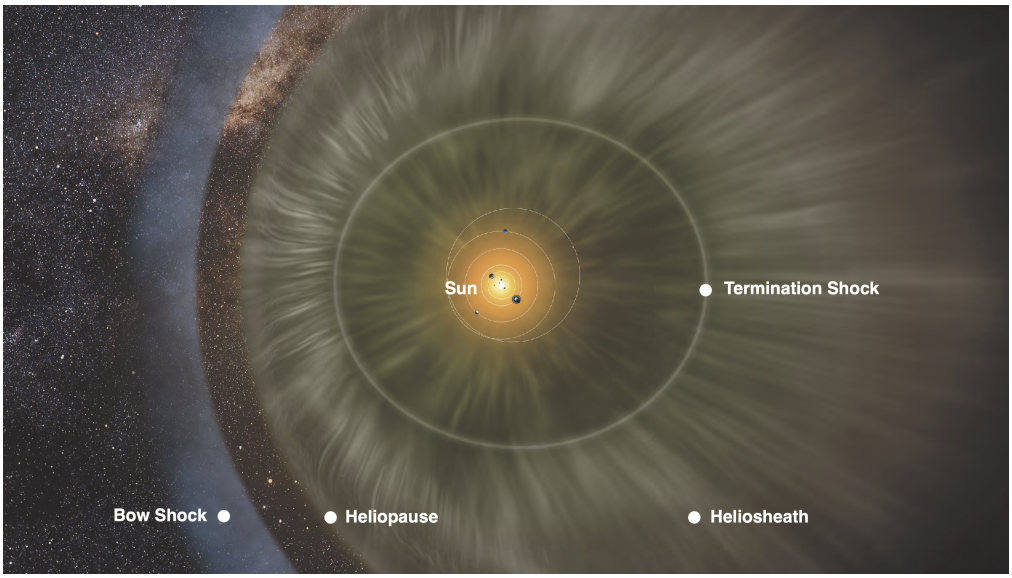

Figure 1.18: Artist depiction of the heliosphere, characterized by the complex interplay between the pressure of the solar wind as it encounters the surrounding ISM. The solar wind is slowed down from supersonic at the termination shock, continues into the heliosheath where it mingles with the ISM, and is finally brought to a halt at the heliopause. A bow shock is created at the interface between the heliosphere and the surrounding ISM. It is expected that *New Horizons* may begin nearing the termination shock in the next few years. (Image: NASA/IBEX/Adler Planetarium.)

Now, after nearly two decades of flight, *NH* is 58 times farther away from the Sun than Earth.[8] As the only telescope in the outer Solar System, *NH* offers a valuable and wholly unique vantage point from which to observe. At this gargantuan distance, it is shifting from answering planetary questions to probing interstellar ones. Anyone who has ever stood under a streetlight in the fog will have noticed how the dim silhouettes of buildings and trees began to appear the further they walked away from the light. Analogously, *NH* is now far enough away from the glare of the Sun that it is finally becoming sensitive to observing structures outside the Solar System, turning it into an instrument capable of investigating the LISM cloudscape in a whole new way.

[8]Giorgini, JD and JPL Solar System Dynamics Group, NASA/JPL Horizons On-Line Ephemeris System, `https://ssd.jpl.nasa.gov/horizons/`, data retrieved 2023-JUN-14

Chapter 2

New Horizons Observations

From its exceptional position in the outer Solar System, what can *New Horizons* see? Each of *NH*'s instruments provides a different window onto the cosmos by observing in a different wavelength regime. In this chapter, we explore why observing at UV wavelengths is ideal for cloud spotting, and we share information about *NH*'s UV spectrograph and its past observations.

2.1 How to Observe Clouds

All baryonic matter interacts with light. For example, stars emit light at a variety of wavelengths as a byproduct of the fusion reactions happening in their cores. Planets emit light because they are warmed by nearby stars, and they re-radiate that energy as infrared light and heat. Hot halos of circumgalactic medium that surround galaxies can be seen shining in x-ray wavelengths due to the high energies and temperatures of the gas particles. In what ways do we expect ISM clouds to interact with light?

There are three main ways to observe interstellar clouds: in emission, reflection, or absorption. Figure 2.1 illustrates examples of all three.

Figure 2.1: The Orion constellation hosts examples of emission, reflection, and absorption nebulae in the same cloudscape. The brightest blue star in the center left of the image is Alnitak (Zeta Orionis), the easternmost star of Orion's belt. Many other young stars and proto-stars lie hidden in the background, enshrouded in the dusty cloud. A red emission nebula is visible in the upper right, where radiation from the nascent stars is exciting and ionizing the gas; as the ionized electrons recombine with hydrogen nuclei, electrons cascade down energy levels and emit that excess energy as red photons. In the foreground, the dark silhouetted horsehead shape is a dense absorption nebula, blocking light from the red emission nebula in the background. Slightly below the Horsehead Nebula to the left is a blue reflection nebula, where blue starlight is scattering off gas particles and illuminating the cloud. The Flame Nebula in the bottom left glows with pink light (emission) threaded with dark filaments (absorption). (Image: Ryan Steinberg & Family, Adam Block, NOAO, AURA, NSF.)

Emission: A hot star or a white dwarf can emit powerful UV radiation that is so energetic as to excite electrons in the surrounding gas. Some UV wavelengths are even energetic enough to cause electrons to become unbound from their atoms, resulting in ionized gas (free-floating electrons, ions, and nuclei). As those electrons lose energy and recombine with nearby nuclei, they emit light at a cascade of different wavelengths, causing the gas to shine. This situation is known as an

emission nebula, because the gas in the cloud is emitting its own light. Frequently, emission nebulae appear burgundy red, a wavelength (656 nm) corresponding to the $n = 3 - 2$ energy transition (Hα) common to hydrogen, which is usually the primary ingredient in interstellar clouds. However, the exact color of an emission nebula depends on the degree of ionization and the chemical composition of the cloud.

Reflection: If the star is slightly less energetic, or a little farther away, its light might simply be scattered off the cloud's gas particles (rather than ionizing them) and sent in a new direction like a ping pong ball bouncing off a paddle. This is called a reflection nebula, because a cloud is reflecting (scattering) light from a nearby source. Reflection nebulae are generally bluish in color, since blue (short) wavelengths are preferentially scattered by atoms (e.g., Rayleigh scattering). In that sense, Earth's atmosphere can be thought of as a reflection nebula because the gas particles in the air scatter blue light from the Sun into all directions, making the sky appear bright with blue light. The air is not a light source in itself, but it is visible to us because it reflects light from the Sun.

Absorption: If the cloud is in front of the light source, and the cloud's gas is cool enough that its electrons get excited to higher energy levels but are not ionized, the cloud can become visible in a *negative* sense by *removing* the background light from the line of sight. This is known as an absorption or "dark" nebula because it appears as a shadow on the sky.

2.1.1 Looking for Cloud Shadows

When it comes to the LISM cloudscape, we are most interested in the third type of observational mechanism: absorption. The other two varieties – emission

and reflection – are common in the cold, dense molecular clouds found in "stellar nurseries," where hot, new stars are being born and pumping out UV radiation energetic enough to ionize the surrounding gas. In comparison to those cold, dense, star-forming cloudscapes, the LISM is relatively warm and diffuse. The LISM is not an active star-forming region, so the gas has no external source to (a) reflect off it, or (b) ionize it and turn it into its own light source. Thus, we expect the LISM to be dark. Our best chance at spotting LISM clouds is if they absorb light from the sky behind them, creating cloud-shaped silhouettes against the ambient galactic background.

2.2 Choosing the Wavelength of Observation

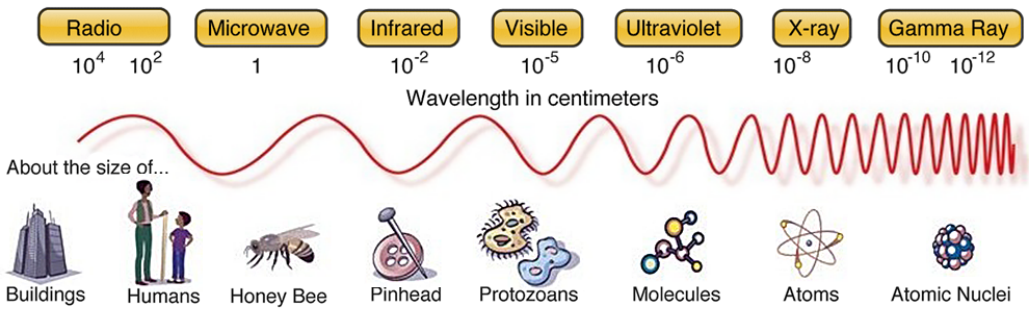

Figure 2.2: The electromagnetic spectrum. When we talk about "light," we're referring to electromagnetic radiation, which comes in a variety of wavelengths. Ultraviolet wavelengths are optimal for observing ISM clouds in absorption because they are on the same scale as the molecules in the clouds. (Image: NASA.)

2.2.1 Ants & Elephants

For light to be blocked by a medium, its wavelength needs to be on the same scale as the size of the particles in the medium. For reference, various wavelength regimes of light are compared with objects of equivalent sizes in Figure

2.2. Imagine an elephant and an ant standing side-by-side. The elephant does not care about the ant because it is too small to notice. The ant does not know the elephant is there because it is too large. Analogously, light only interacts with matter that exists on the same spatial scale. This is why the radio in your car continues to play music when you are driving downtown, because the radio waves (with long wavelengths of 10s to 100s of feet) do not "see" the buildings, they just weave around the skyscrapers to reach your car stereo. This is also why x-rays (0.01 to 10 nm) pass easily through skin, but get stopped by denser materials like tumors or bones, which have more atoms per unit volume than the surrounding tissue.

Infrared light, for example, has a long wavelength that can pass unhindered by gas and dust, allowing it to penetrate through media like the LISM. UV light, however, has a shorter wavelength, and is readily blocked and scattered by gas and dust. Most of the strong absorption lines of common LISM elements are found in the UV and far UV (Fig. 2.3). For this reason, UV radiation is an optimal wavelength for observing gas in absorption. Thus by using *NH*'s UV instruments to measure the Milky Way's ambient UV radiation, we can hope to look for the shadows of LISM clouds appearing against that UV backdrop.

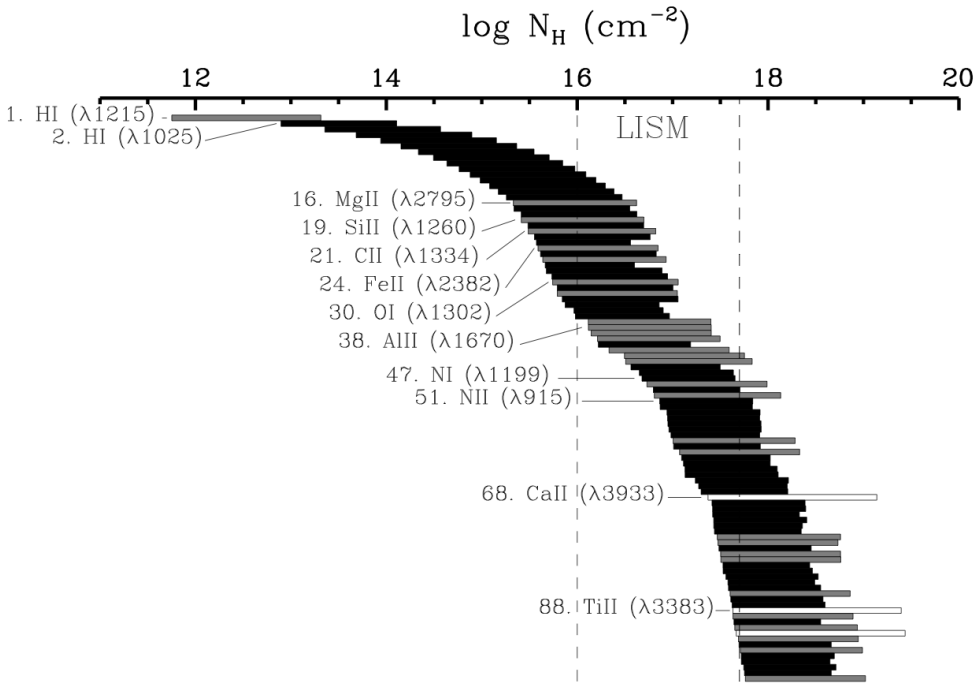

Figure 2.3: The 100 strongest resonance lines, ranked in order of their hydrogen column density sensitivity. Elements that fall in the optical (3000-10000 Å) are indicated by white bars, UV (1200-3000 Å) in grey, and far-UV (900-1200 Å) in black. The typical range of hydrogen column densities observed for warm LISM clouds is demarcated by vertical dashed lines. (Image: Redfield (2006).)

2.2.2 Lyman-alpha Glasses

This study is particularly interested in UV light with a wavelength of 1216 Å (121.6 nm), commonly referred to as Lyman-alpha (Lyα). It is the type of light emitted when an electron transitions from the $n = 2$ to $n = 1$ energy state within a neutral hydrogen atom. This is the most fundamental energy transition in the most abundant element in the cosmos, and it is therefore a powerful spectral signature for probing the presence of nearby hydrogen gas.

Lyα is produced in abundance across the Galaxy in recombination cascades, in which ionized hydrogen reabsorbs an electron which then spontaneously cascades

down to lower energy levels. Recombination cascades are ubiquitous in the H II regions surrounding young stars. When a high-mass star is born in a star-forming nebula, the new star emits powerful UV photons that ionizes the surrounding hydrogen gas, resulting in a singly ionized hydrogen (so-called H II) region. As free electrons in the cloud collide with the ionized hydrogen nuclei, some electrons are re-absorbed into the atom and then cascade down to lower energy levels. All of the possible cascade chains eventually end with the $n = 2$ to $n = 1$ Lyα transition, emitting a Lyα photon. Theory predicts that for every Hα ($n = 3$ to $n = 2$) photon produced, 1.61 Lyα ($n = 2$ to $n = 1$) photons are also produced (Lallement et al. 2011).

Depending on the density of the gas that surrounds the new star, these Lyα photons can get caught in the nebula, continually scattered, absorbed, and re-emitted. Each time a photon scatters off an atom, it has the opportunity to exchange energy, such that the atom loses/gains a little momentum while the photon shifts slightly up/down in wavelength (or frequency). The further the photon's wavelength is shifted away from 1216 Å, the less susceptible it is to being scattered or absorbed again, and the better chance it stands at escaping the cloud. Consequently, the Lyα radiation that successfully escapes an H II region or an ISM cloud has usually been shifted slightly away from its original central wavelength (known as "line center"). This results in characteristically double-peaked emission line shapes (see example in Figure 2.4), where most of the radiation at line center has been shifted to slightly shorter or longer wavelengths. Emission line profiles will be discussed more in Chapter 3.

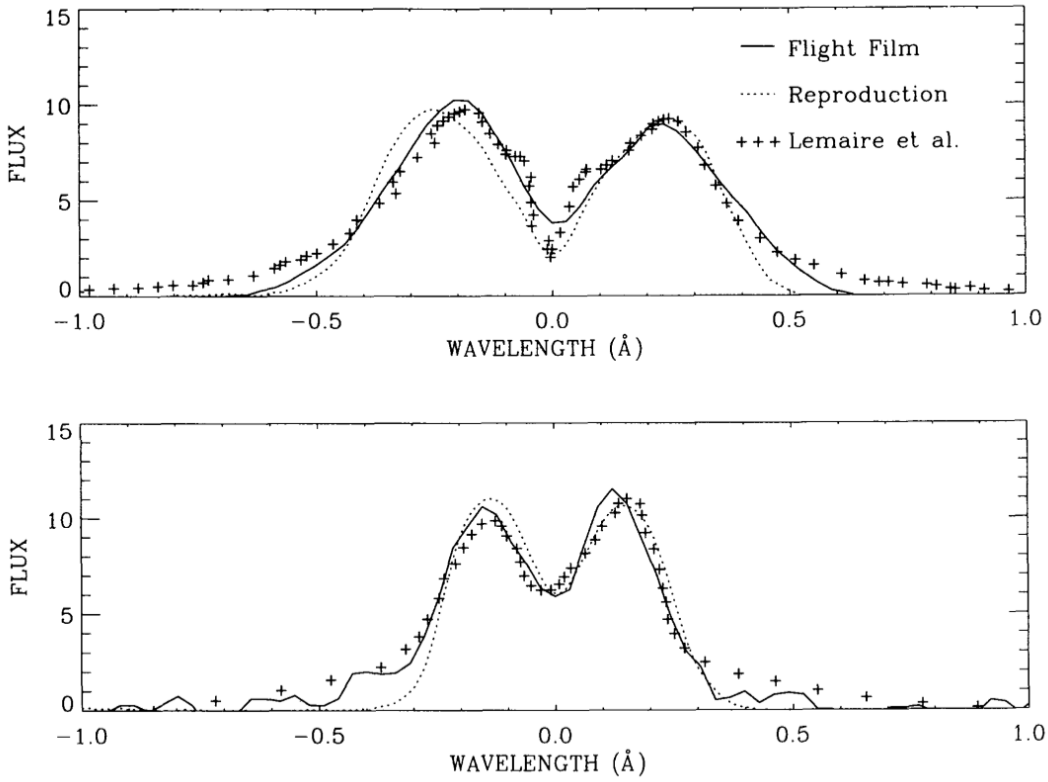

Figure 2.4: Solar Lyα (upper) and Lyβ (lower) emission lines, comparing data collected from a 1962 rocket test flight (solid) with a later study by Lemaire et al. (1978). The x-axis indicates the distance in wavelength space of the emergent radiation from the relevant line center, where zero corresponds to 1215.67 Å (upper) and 1025.72 Å (lower). The available electron energy transitions of hydrogen (present in the Sun's atmosphere) make it good at absorbing and scattering Lyman-series photons. The photons that successfully escape the solar atmosphere are thus shifted away from Lyα and Lyβ line centers, giving these emission lines their characteristic double-peaked profiles. (Image: Meier (1995).)

In addition to photoionization and recombination cascades in H II regions, there are many more mechanisms by which Lyα photons are produced, including collisions in the shock waves generated by supernovae and stellar winds. As a result, the presence of Lyα photons is nearly ubiquitous across the Universe. If we could put Lyα glasses over *New Horizons*' eyes, we would expect to see light coming from every direction in the Galaxy. And yet, Lyα is readily absorbed by

hydrogen, which is the main ingredient of ISM clouds. These qualities make Lyα the ideal diffuse background light source upon which to look for shadows cast by the nearby LISM cloudscape.

2.3 Alice UV Spectrograph

At its launch, *NH* was outfitted (Fig. 2.5 and 2.6) with many instruments to characterize the surface and atmospheric properties of Pluto and other Kuiper Belt objects (KBOs), including a UV spectrograph to detect gas species in their tenuous atmospheres. But what is an atmosphere if not a planet-hugging gas cloud? As *NH* travels further from the inner Solar System and transitions its planetary objectives into astronomical ones, the UV spectrograph is being repurposed to look for interstellar clouds as well.

Figure 2.5: *NH* being assembled in the lab. (Image: Johns Hopkins APL.)

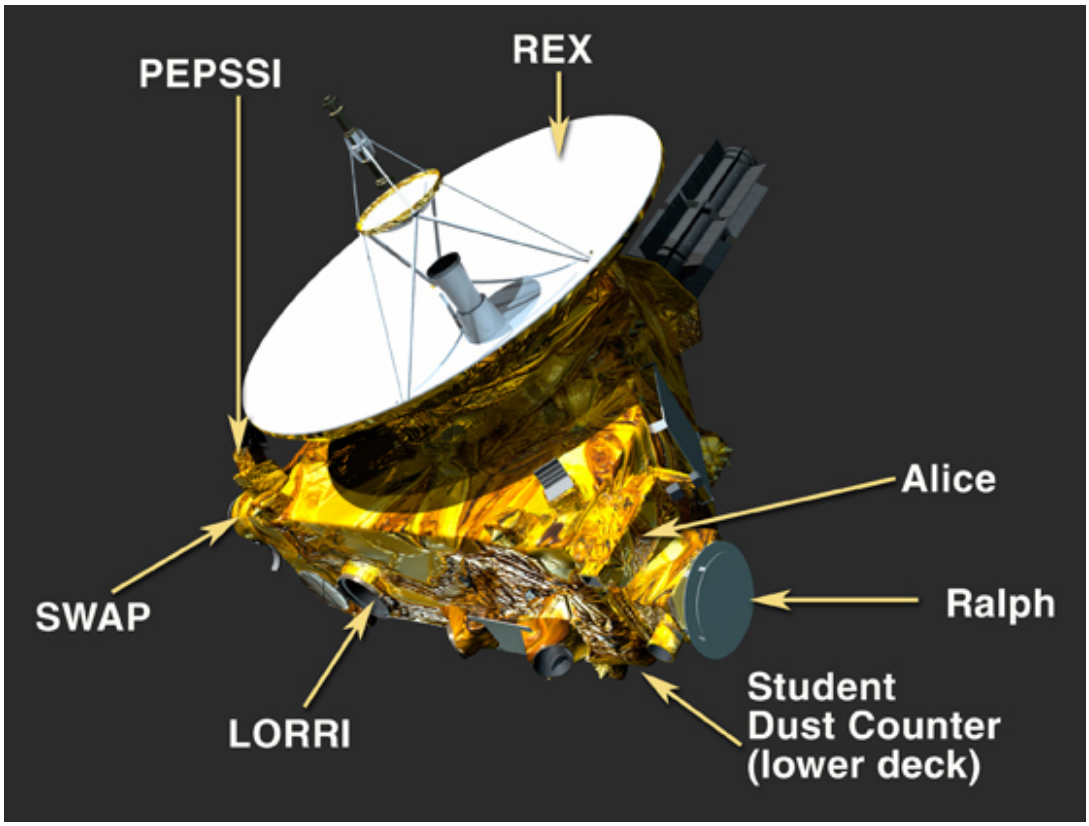

Figure 2.6: Diagram showing the various scientific instruments aboard *NH*. (Image: Johns Hopkins APL.)

2.3.1 Purpose

The instrument used in this thesis is the P-ALICE UV Spectrograph (Alice) aboard *NH*. The specs of Alice summarized in this chapter can be found in detail in Stern et al. (2008).

The primary purpose of Alice was to characterize Pluto's atmosphere during its flyby, including optical depth, escape rate, airglow brightness, relative abundances of elements, vertical temperature, and density structure. Secondarily, it was intended to search for atmospheres around Charon and other KBOs, and measure the albedo of all surfaces, including Nix and Hydra (Pluto's small moons). Alice was designed to observe light in the ultraviolet range (UV) at 520 - 1870 Å,

and the spectral passband was measured pre-flight to be even better than anticipated (465 - 1881 Å). In general, the spectral point spread function (resolution) was measured to be 3 - 6 Å full width half max, and the spatial resolution was measured to be $\sim 0.6°$ (see the 6° long field of view in Fig. 2.8). During the first several months after *NH*'s launch, commission tests showed everything on Alice to be functioning nominally.

Secondary to studying Pluto's atmosphere, Alice additionally serves as a tool for taking sweeping UV measurements of the sky throughout the voyage, recording changes in ambient UV radiation as a function of distance from the Sun. Alice's all-sky UV observations provide a canvas upon which the shadows of LISM clouds might be imprinted.

2.3.2 Systems & Components

The major components of Alice include a telescope, a Rowland-circle spectrograph, a detector at the focal plane, and associated electronics and mechanisms (see Fig. 2.7 for schematic of the system components).

Alice has 2 different apertures for light to enter the telescope: (1) the Airglow Channel (AGC) and (2) the Solar Occultation Channel (SOC). The combined aperture slit has become known as the "lollipop" (Fig. 2.8). The 40×40 mm^2 square SOC slit ($2° \times 2°$ field of view) sits atop the stem-like AGC slit which is 60 mm tall and 1 mm wide ($6° \times 0.1°$ field of view). The thin AGC slit is the primary detector. The square SOC was added specifically to ensure the Sun could be encompassed inside the field of view during the solar occultation observations of Pluto and Charon's atmospheres.

Light enters both apertures and is focused by a f/3 off-axis paraboloidal (OAP)

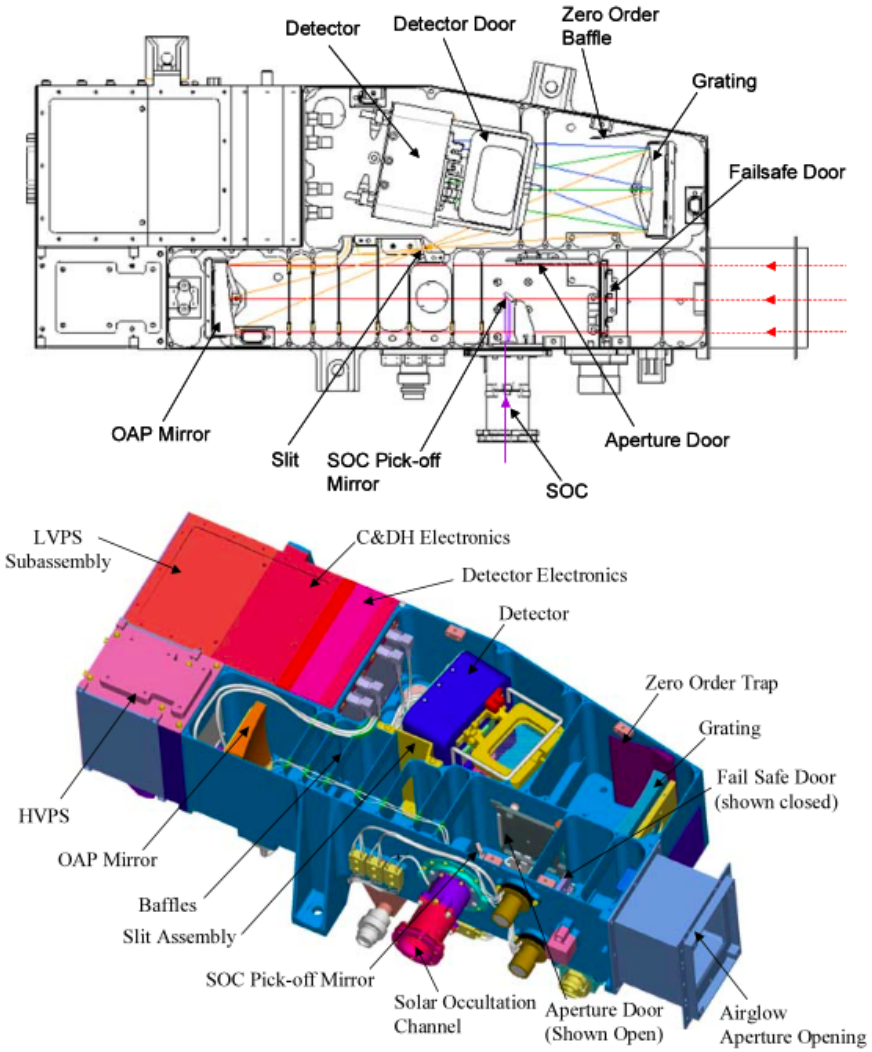

Figure 2.7: Schematic of Alice. Light enters through the AGC aperture (right) and the SOC aperture (bottom). A mirror redirects the SOC beam 90° to join the AGC beam. Both beams then reflect off the OAP mirror and are redirected through a slit to the diffraction grating. The diffracted light is then sent to the detector where it is recorded. (Image: Stern et al. (2008).)

primary mirror onto a toroidal holographic diffraction grating, dispersing the light before directing it to a double-delay line (DDL) microchannel plate (MCP) detector. The MCP has back-to-back photocathodes coated with potassium bromide (KBr) and cesium iodide (CsI).

The active portion of the detector is 35 mm in the dispersion (horizontal)

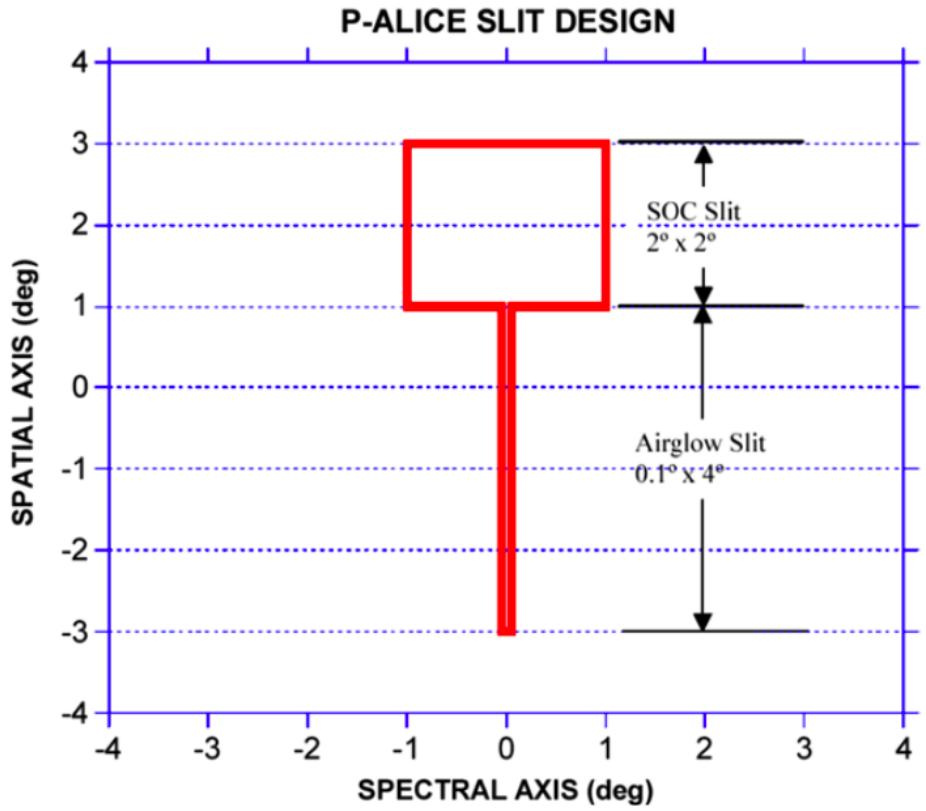

Figure 2.8: The Alice aperture is called the "lollipop." (Image: Stern et al. (2008).)

direction by 20 mm in the spatial (vertical) direction. The pixel format (1024×32 pixels) allows for Nyquist sampling with a spectral resolution of 3.6 Å.

When looking at "empty" sky (avoiding stars or extra-galactic objects), Lyα is exceedingly bright compared to other UV emission, so Alice was intentionally given a reduced sensitivity to LyA along its main slit, such that the detector is not saturated at Lyα line center. The maximum count rate capacity of the detector electronics is 3×10^4 counts s^{-1}, so they needed to attenuate the Lyα emission brightness by at least an order of magnitude to prevent saturation. To accomplish this, they masked the MCP region around Lyα while the photocathode was being coated with KBr. The bare MPC glass has 10% the quantum efficiency of KBr at

1216 Å, effectively lowering the sensitivity by one order of magnitude. This effect can be seen in a sample Alice histogram observation in Figure 2.9 and sample spectrum in Figure 2.10.

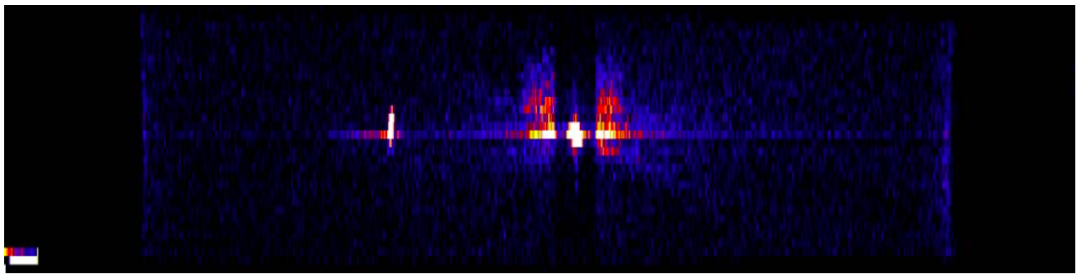

Figure 2.9: Sample Alice histogram observation of Lyα, showing the characteristic diminished sensitivity around 1216 Å in the center of the slit, flanked by the relatively bright (un-diminished) wings of the Lyα line, and a ghost of the Lyα line on the left. (Image: Stern et al. (2008).)

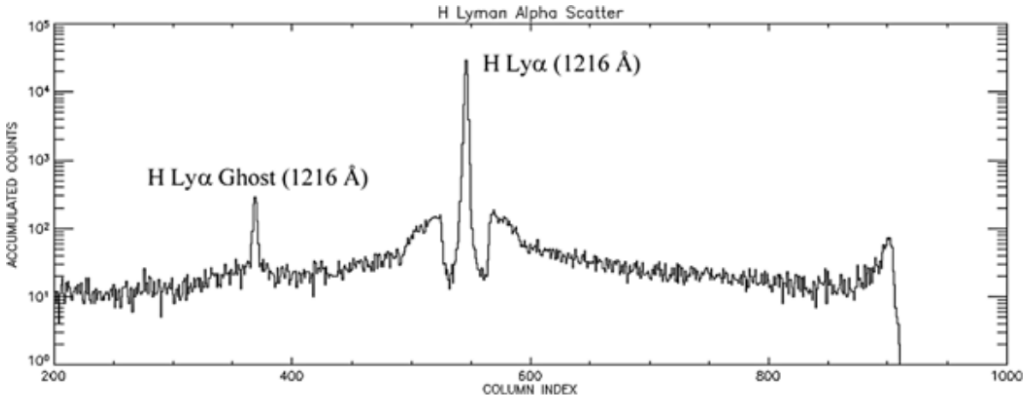

Figure 2.10: Sample Alice spectrum, showing Lyα emission centered in the photocathode gap, and the Lyα ghost at 893 Å on the left. (Image: Stern et al. (2008).)

The reduced sensitivity bare glass runs up the entire AGC slit, extending through the center of the SOC box. However, the left and right wings of the SOC box were coated with KBr to enable full sensitivity, and consequently the SOC lets in off-axis Lyα light. Due to the addition of the SOC, Alice ended up being very sensitive to diffuse off-axis Lyα photons in the box. Alice's sensitivity for

diffuse Lyα is 4.92$\pm$0.09 counts s^{-1} per Rayleigh (see Section 2.3.5 for a discussion of Rayleighs), which is 500 times that of the *Voyager* missions (Gladstone et al. 2021).

A ghost of the Lyα emission appears left of line center. The source of the ghost was determined to be an artifact of the diffraction grating: the Lyα emission line reflects off the surface of the MCP detector back towards the diffraction grating, where it is diffracted a second time back onto the detector.

2.3.3 Resolution

The spectral resolution of the instrument is 3.6 Å. Spectral resolution corresponds to how fine a wavelength measurement Alice can make. The capacity in which I will be using Alice is as a simple photometer (counting photons, not taking spectra), so I will be primarily concerned with spatial resolution, not spectral.

There are 20 pixels going up the stem of lollipop, and each pixels provides 0.3° of spatial resolution. When the lollipop scans left to right (perpendicular to its length), each pixel makes a 0.3° high swatch across the sky. Spatial resolution in the horizontal direction depends on the scan rate and how they bin the data. For example, using the new HCCR mode (described in Section 2.3.4), Great Circle observations (360°) are taken by sweeping the detector horizontally (perpendicular to the stem) at a scan rate of roughly 2 hours per circle, which results in a spatial resolution of $\sim$ 0.05° s^{-1}. If they bin the data every second while scanning the sky, they achieve a spatial resolution of 0.05° in the horizontal direction but 0.3° in the vertical direction along the stem, so generally the spatial resolution is 6 times better in the horizontal direction than the vertical. It is estimated that a future orthogonal all-sky survey could improve the resolution $\sim$ 20-fold (Gladstone

2024).

2.3.4 Data Collection Modes

Alice was built to collect data in one of two modes: Histogram Imaging and Pixel List mode. In the Histogram Imaging mode (primary), the detector integrates over a specific period of time and reads out the entire 2D array as an image. The Histogram observations are spatial in the y-direction (noting where each photon lands vertically, along the length of the slit, and counting up the total number of photons that land in each pixel) and spectral in the x-direction (recording the wavelengths of the incumbent photons, which are spread out into a horizontal spectrum). An example of a Histogram observation is shown in Figure 2.11. The Pixel List mode (secondary) does everything the Histogram mode does (y spatial, x wavelength), but in addition, the detector records *when* each photon arrives, adding the extra dimension of time. As a result, Pixel List outputs a 3D data cube where each x-y layer is a histogram, and the z-axis is time. The trade-off for providing detailed time resolution is that Pixel List mode uses a lot of memory. As a result, the Histogram mode is preferred if time resolution is not needed. Alice is also capable of filtering out selected regions of the detector, which can be useful for suppressing hot pixels or blocking certain bright features that might otherwise take up a lot of memory.

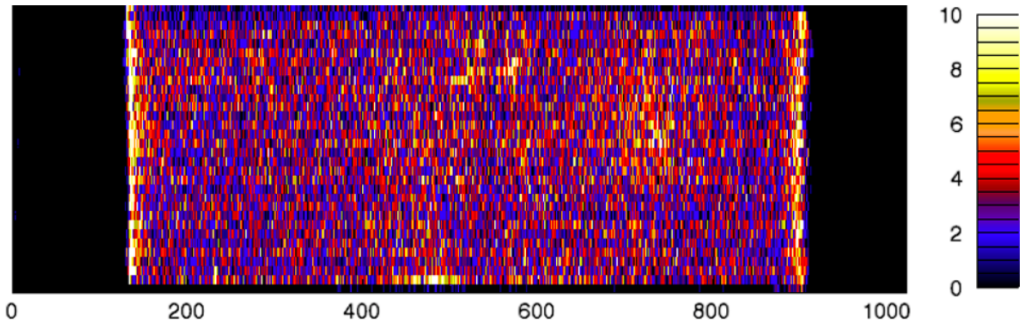

Figure 2.11: This is a sample histogram observation, showing spatial data along the y-axis and wavelength on the x-axis, for a 9.1-hour accumulated dark count exposure. The colorbar is in units of accumulated counts per pixel over the entire 9.1-hour exposure. (Image: Stern et al. (2008).)

In both modes, data are downlinked back to Earth along with "housekeeping" packets. These auxiliary packets include a slew of system status information so the Science Team can continually monitor proper functioning of the instrument. The frequency with which housekeeping packets are sent can be adjusted (i.e., each second, minute, etc.). Among the housekeeping data is the most current value of the count rate, which is to say, the total number of photons that hit across the entire detector during that time interval. Ingeniously, the Science Team found that this housekeeping data could serve a secondary, unintended function. Every year they made six additional observations, slowly rotating *New Horizons* to sweep six Great Circles across the sky. They kept only the housekeeping packet, specifically for the count rate data. By programming the binning and data return frequency for a constant rate, this essentially functioned as simplified photometer, counting the total number of photons hitting the detector without worrying about where they hit. This was used to take broad swath Lyα readings of the sky in a relatively efficient manner. The detector picks up all wavelengths in the 520 - 1870 Å passband, but under the assumption that the vast majority of the incoming flux

is Lyα (when not looking directly at a star), the photon count can be used as a proxy for Lyα photon count.

The Science Team wrote an additional software package for the instrument in the last couple years to install a new, third mode. Since 2021, they are able to use the photometer functionality on its own through the new High Cadence Count Rate mode (HCCR). The HCCR mode gives them a count rate without needing to command the housekeeping packets. By avoiding the housekeeping packets, which enclose a lot of excess information, this new mode can function much faster and with greater efficiency. This new mode only tells them how many counts they got in some time interval, which can be adjusted from 2.5 seconds down to 10 milliseconds. With this new mode installed, they have achieved a level of efficiency that has made it possible to move from six Great Circles to doing all-sky observations.

2.3.5 Units

Alice's UV intensity observations are reported in Rayleighs (R). As a unit, the Rayleigh was originally introduced by Hunten et al. (1956) to measure the scattering of light by Earth's atmosphere, and later was recognized as being useful as a unit for surface brightness and the apparent radiance of extended light sources (i.e., photon flux emitted per solid angle in a given direction by a unit of surface area of the source).

One Rayleigh corresponds to an emission rate of 1 million photons s^{-1} from an extended column of 1 cm cross section (Baker & Romick 1976),

$$1\mathrm{R} = 10^{10}\ \mathrm{photons\,s^{-1}(m^2\,col)^{-1}}.$$

A Rayleigh can equally be defined as apparent photon radiance, where

$$1\text{R} = \frac{\pi}{4}(10^{10}) \text{ photons s}^{-1}(\text{m}^2 \text{ str})^{-1}.$$

Rayleighs only cover *apparent* emission from a source and do not take into account scattering or absorption that may be occurring. Rayleighs are scaled to be useful for faint, extended, gaseous sources, with the Rayleigh ideal for sky glow and the kilo-Rayleigh for auroras. To give a sense of scale, the night sky at zenith is ~ 250 R, twilight can range from $\sim 100 - 1000$ R, and auroras can reach 1000 kR (Hunten et al. 1956). As a measure of photon flux for faint sources, Rayleighs are a convenient unit for recording Alice's Lyα photon counts.

2.4 Alice Observations

For the majority of *New Horizons*' journey, the Alice spectrograph has been in hibernation to preserve power and reduce stress on the instruments. Once a year during an "Annual Checkout" (ACO), instruments were woken up and tested to ensure proper functioning. During these ACOs, *NH*'s thrusters fired to spin the spacecraft in a circle, allowing Alice to take one thin strip of data sweeping across 360° of sky, forming what is called a Great Circle.

Great Circles are the largest circles that can be drawn on the surface of a sphere, where the center of the circle is also the center of the sphere. If the entire sky from *NH*'s vantage point is imagined as a giant sphere of celestial proportions, a plane that intersects that sphere and goes through its center would trace a Great Circle across the sphere's surface.

As *NH* approached its first target in 2015 – the Pluto-Charon system – Alice woke up again. Alice took three Great Circle observations during the approach to

Pluto (at −28 days), and another three Great Circles after passage (at +1 day). After completing its primary mission at Pluto, *NH* proceeded into the Kuiper Belt for its first Extended Mission (KEM). Every several years since 2016, Alice has again done another set of six Great Circles. To take these observations, Alice spins 360° to carve out one circle, then pivots left or right before spinning out another circle, as if tracing the wedges of an orange. Dates and details about the Great Circle observations are found in Table 2.1 and depicted in Figure 2.12. The latest Great Circle observation is explained in Section 2.4.1, and the science derived from these observations follows in Section 2.4.2.

In 2021, Alice's software was updated to introduce the HCCR mode, in which Alice integrates over the passband (520 - 1870 Å) and sends down the total photon count rate. This simplified mode allows for more efficient data transfer and enables the spacecraft to move on from simple Great Circles to observing larger patches of the sky. As a result, in 2021 Alice was able to observe a 30° swath of the sky as a proof-of-concept using the new HCCR mode. This observation is explained in Section 2.4.3. Thanks to a successful proof-of-concept, in 2023, Alice was approved to perform its first all-sky observation. Using the HCCR mode, the entire observation took 10 days to complete, and is detailed in Section 2.4.4.

Table 2.1: Circumstances of *New Horizons* Alice Great Circle Lyα Observations

Lyα Observation	ACO-1	ACO-2	ACO-4	P-28	P+1
Date	2007 Oct 07	2008 Oct 18	2010 Jun 19	2015 Jun 16	2015 Jul 15
Start UTC (hh:mm:ss)	02:13:46	11:48:31	09:08:36	19:38:03	19:05:04
End UTC (hh:mm:ss)	03:10:44	13:51:51	11:13:41	20:24:01	19:51:01
Scan Duration (s)	3418	7400	7505	2758	2757
Scan Rate ($^\circ s^{-1}$)	0.1	0.1	0.1	0.1	0.1
r_{NH} (au)	7.624	11.337	16.991	32.679	32.919
λ_{NH} ($^\circ$)	259.32	269.33	276.56	284.02	284.09
β_{NH} ($^\circ$)	1.17	1.50	1.72	1.91	1.91
l_{NH} ($^\circ$)	2.04	7.34	11.14	15.12	15.16
b_{NH} ($^\circ$)	9.86	1.35	-4.81	-11.14	-11.20
NH-Sun-Earth angle ($^\circ$)[a]	+114.00	+116.00	-8.88	-18.99	+8.88

Lyα Observation	KEM-1	KEM-2	KEM-3	KEM-4	KEM-5
Date	2017 Jan 28	2017 Sep 19	2019 Mar 03	2019 Aug 30	2020 Apr 27
Start UTC (hh:mm:ss)	13:07:58	07:48:09	15:28:10	23:46:24	12:02:40
End UTC (hh:mm:ss)	19:18:37	13:59:00	21:39:16	29:57:38	18:13:57
Scan Duration (s)	22239	22251	22266	22274	22277
Scan Rate ($^\circ s^{-1}$)	0.1	0.1	0.1	0.1	0.1
r_{NH} (au)	37.561	39.472	43.775	45.229	47.161
λ_{NH} ($^\circ$)	285.15	285.52	286.25	286.46	286.73
β_{NH} ($^\circ$)	1.93	1.94	1.96	1.96	1.96
l_{NH} ($^\circ$)	15.74	15.94	16.34	16.46	16.60
b_{NH} ($^\circ$)	-12.10	-12.41	-13.02	-13.20	-13.43
NH-Sun-Earth angle ($^\circ$)[a]	-156.56	+70.77	-123.73	+50.61	-69.33

[a] Angles are negative from solar conjunction until opposition and positive from opposition until solar conjunction.

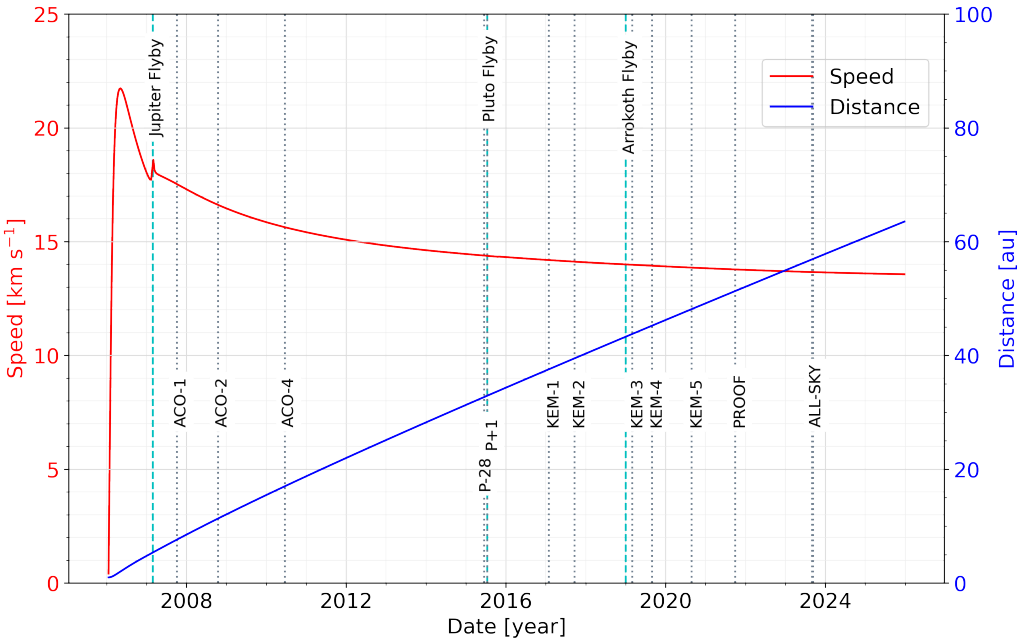

Figure 2.12: Trajectory of *New Horizons* spacecraft, with speed indicated in red and distance from the Sun shown blue. Major milestones are marked by dashed cyan lines, and the dates of key Alice observations are marked in grey dots. The NASA/JPL Horizons On-Line Ephemeris System[1] was used to project *NH*'s trajectory out to 2026 (Giorgini et al. 1996; Giorgini & Yeomans 1999; Giorgini et al. 2001).

2.4.1 Great Circles

The latest six ACO Great Circle observations were completed in August 2019 and are shown in Figure 2.13 (Gladstone et al. 2021). The Great Circles form an intersecting, spiderweb-like pattern when viewed as a rectangular projection. Alice repeatedly passed over the same two regions on opposite sides of each sweep, resulting in higher resolution at the intersection points where all the strands of the web come together. The deep red spots in the data can be attributed to stars, which appear as point sources in UV. These red points are concentrated around galactic longitude of $l = 0°$, which makes sense because most stars in the

[1]Giorgini, JD and JPL Solar System Dynamics Group, NASA/JPL Horizons On-Line Ephemeris System, `https://ssd.jpl.nasa.gov/horizons/`, data retrieved 2023-JUN-14

Milky Way lie in the galactic mid-plane. The background of the figure shows a composite model of the expected Lyα radiation from scattered solar and Galactic origin (discussed in Section 2.4.2).

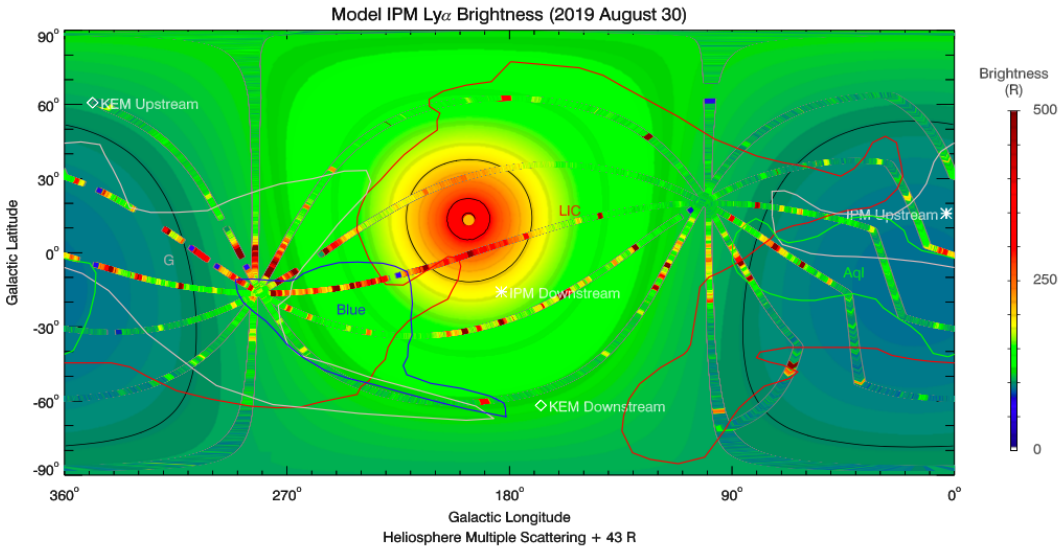

Figure 2.13: Six-Great-Circle scan of August 30, 2019 overlaid on Wayne Pryor's model background (which includes heliosphere multiple scattering of solar Lyα and a 43 R offset). The location of the Sun is marked by an orange dot. The outlines of the four nearest LISM clouds (LIC, G, Blue, and Aql, as described by Redfield & Linsky (2008)) are overlaid for comparison. (Image from: Gladstone et al. (2021).

Aside from pollution from stars across the mid-plane, it is expected that the Lyα resultant from scattered solar radiation should produce a smooth exponentially declining gradation moving outwards from the Sun. The relatively good fit between the background model and data suggests that any brightness variations due to the LISM cloudscape will likely be occurring at the 10 - 20 R level. In a first effort to account for those low-level deviations between the background model and data, Gladstone et al. (2021) cross-checked these Great Circle observations against the outlines of several nearby clouds (see comparison with LIC, G, Blue, and Aql in Figure 2.13). They found no obvious signs that the data's variation

from the model could be attributed to those specific cloud boundaries, except possibly in the lower left quadrant around $(l, b) = (290, -80)$ where a Great Circle dims as it passes into the LIC. This curious occurrence, and the otherwise unexplained deviation of the data from the background model, inspired the *NH* Science Team to propose observations of larger swaths of the sky to look for more mottled patterns that might be attributable to LISM cloud shadows.

2.4.2 Sources of Lyman-alpha

Although the Great Circles observed during ACOs captured only small slices of the sky, these observations led to significant scientific findings that both confirmed and challenged prevailing assumptions about the origins of local Lyα emission.

Stars emit light at the full range of UV frequencies, so when Alice directly passes over a star, the detector is saturated with stellar UV emission across the entire passband (520 - 1870 Å). This is apparent in the Galactic mid-plane of Figure 2.13 where Great Circle observations show high UV fluxes in the 200 - 500 R range at latitudes around $b = 0°$. However, when observing patches of sky devoid of stars, such as at high and low galactic latitudes where no apparent stellar UV sources are present, the brightness across the passband should be dominated specifically by Lyα at 1216 Å. For this reason, in directions away from the Galactic mid-plane (i.e., high and low galactic latitudes), we can make the simplifying assumption that any flux received by Alice can be attributed solely to Lyα. Only those Alice observations free from stellar contamination are of use for analysis in this thesis. Consequently, when Alice observations are described, it is with the assumption that 100% of the observed flux is due to Lyα and any UV emission from the rest of the passband is negligible. But if not originating from stars, where

exactly does the ambient Lyα flux come from?

Solar Lyman-alpha

The Sun is the most obvious source of Lyα observed within the Solar System. If the only source of Lyα is the Sun, then when Alice points directly at the Sun, it should record diminishing levels of Lyα emission the further *NH* travels according to an inverse square law. In this way, it was expected that Alice's measurements of direct solar Lyα should decrease as $1/r_{\mathrm{NH}}^2$, where r_{NH} is *NH*'s radial distance from the Sun.

Analysis of Great Circle observations across a decade of ACOs revealed that Lyα flux was decreasing as *NH* traveled further from the Sun (Gladstone et al. 2018, 2021). Since light becomes diluted the further it spreads out from its source, this result was expected, but the exact rate of change did not match predictions, suggesting other factors were at work.

Scattered Solar Lyman-alpha

In addition, the Lyα coming from the Sun will scatter off any particles along its path. The space between planets is inhabited by many varieties of particles – including neutral hydrogen blown in from the ISM, and charged particles blown out by the solar wind – which are collectively known as the interplanetary medium (IPM). Solar Lyα scatters off the IPM like a lamppost scattering off fog, causing the entire sky to glow with redirected Lyα. This scattered light is found empirically to diminish as *NH* moves away at a rate of $1/r$ (Gladstone et al. 2021).

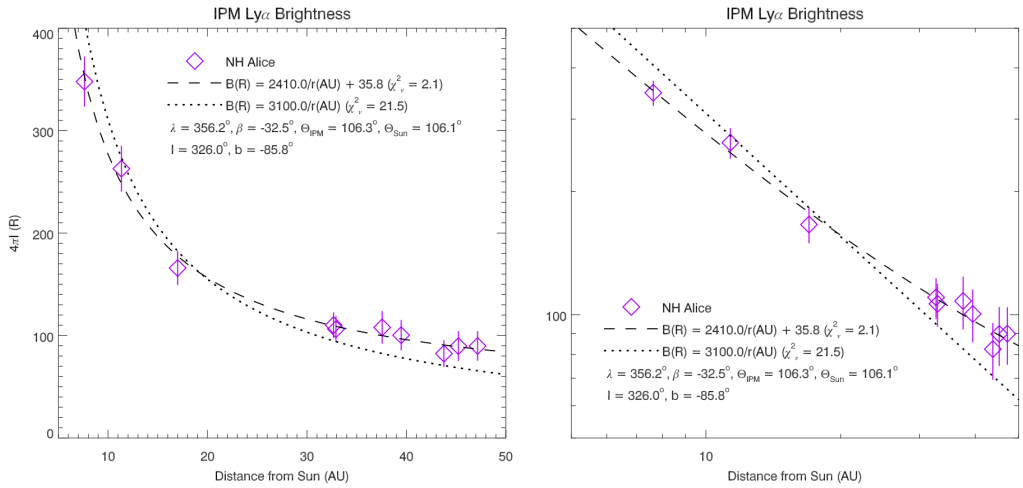

Figure 2.14: Lyα brightness of the IPM in the direction (l = 326.0°, b = -85.8°) as a function of *NH*'s distance from the Sun (r_{NH}). The panels are identical aside from the scaling of the x-axis, linear (left) and logarithmic (right). The brightnesses in this figure have been scaled by $2.4 \times 10^{12}/\pi F_0$ (photons cm^{-2} s^{-1} nm^{-1} at 1 au), where πF_0 values given in Table 1 of Gladstone et al. (2021) account for temporal variations of the line-center solar Lyα flux. Empirical models indicated by dashed lines have been fitted to the data. The data is found to be best fit by a $1/r_{NH}$ profile plus a constant 35.8 R background. (Image: Gladstone et al. (2021).)

In Figure 2.14, Gladstone et al. (2021) try to fit a line to the decay rate of Alice's Lyα brightness as a function of r_{NH}. The observations cannot be solely explained as direct solar light (which would decrease as at rate of $1/r^2$), so IPM-scattering must play a significant role. However, the observations are not fit by a simple $1/r$ IPM-scattered solar model either (dotted line), and the measurements appear to drop off slower than expected. They find the data is best fit if a constant 35.8 R Lyα flux is added to the model (dashed line). In later works, Gladstone shows that data from *Pioneers*, *Voyagers*, and *New Horizons* all appear to be asymptoting to a background emission level around 43 ± 3 R (Gladstone et al. 2021).

This was an exciting and surprising result, suggesting a low-level Lyα source exterior to the Sun, originating from the surrounding Milky Way. Scattered solar

light was dominant in observations from the inner Solar System due to proximity to the Sun, but as scattered solar light fades the further away *NH* travels, the Lyα of Galactic origin has become increasingly prominent. Beyond Neptune, the Galactic Lyα signal became dominant, and it now constitutes $\sim 50\%$ of the observed Lyα flux (Gladstone et al. 2021). Based on Great Circle observations, it was suggested that this Galactic Lyα is isotropic, originating equally from all directions. However, with more comprehensive surveys of the entire sky, directional dependence might be revealed.

In order to characterize the solar contributions to the observed Lyα flux, a theoretical model was created by Pryor et al. (2024). Pryor's scattered solar model is based on Ajello et al. (1987) for the inner heliosphere and Hall (1992) for the outer heliosphere (outside optical depth 1).

At its basis, Pryor's model computes how solar Lyα photons should scatter off particles in the IPM, resulting in sky glow that changes as function of distance from the Sun (r_{NH}). The model neglects any potential impact of solar radiation back-scattering off structures in the outer Solar System (namely, the Hydrogen Wall, a theorized region of hot hydrogen predicted to lie between the heliopause and bow shock). This assumption is known as a "hot" model because it assumes that solar radiation is only disturbed by IPM close to the Sun. Hot models assume a Maxwellian velocity distribution of particles at infinity, where infinity is defined to be inside the termination shock. Thus it should be noted that hot models will not work once *NH* passes the termination shock, and are not relevant for the *Voyager* spacecrafts since they have surpassed this boundary. Very little sunlight reaches as far as the Hydrogen Wall, so we would expect the solar scattering off the Hydrogen Wall to be modest, contributing at most 10 - 20 R to the overall Lyα background.

Initial comparisons between the Great Circle observations and Pryor's IPM scattering model showed the observed Lyα falling off faster than the predicted $1/r$, which indicates the Galactic emission may be even more important that we realized. The scattered solar model depicts a Lyα sky glow that is brightest near the Sun and smoothly declines towards its minimum at the anti-solar pole. The minimum of the scattered solar model is currently 47 R, which is roughly equivalent to the Galactic background.

The most recent Great Circle data is compared against Pryor's IPM scattering model *plus* a 43 R offset in Figure 2.13, which results in a better fit (Gladstone et al. 2021). However, the data deviates from the model seemingly randomly, at scales on the order of 10 - 20 R, suggesting subtle structure to the Galactic Lyα emission that could indicate other emission and absorption factors at work.

Other Sources

For our purposes, the most intriguing potential source of these data-model deviations is the LISM cloudscape, which may be blocking incident Galactic radiation from reaching *NH* along certain sight lines. Other non-solar Lyα sources have been suggested that could contribute to the mottled Galactic Lyα background, including solar Lyα back-scattering off the Hydrogen Wall (Baliukin et al. 2022) and two-photon production generated by shocks in the LISM (Kulkarni & Shull 2023), which could originate from fast-moving stars (Shull & Kulkarni 2023) or even cloud-cloud collisions (Linsky et al. 2008). Several of these factors will be discussed and incorporated into our models in Section 4.2.

2.4.3 Proof-of-Concept

To test the idea of doing an all-sky Lyα observation with Alice, the *NH* Science Team first conducted a proof-of-concept observation at 51.3 au on September 29, 2021 that covered a 30° swath of the sky. Figure 2.15 shows the data from the observation, overlaid on the Pryor et al. (2024) scattered solar background model plus a 43 R offset.

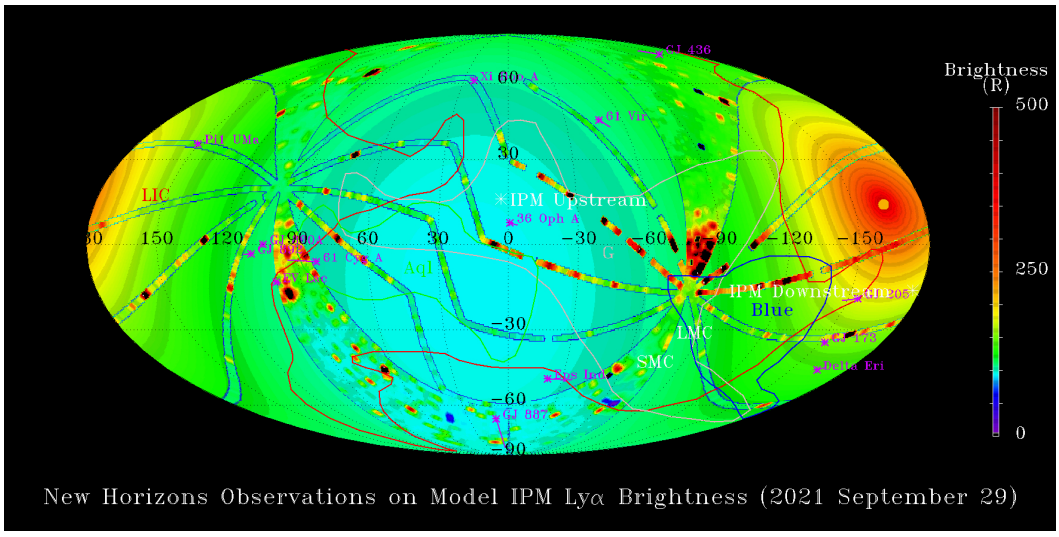

Figure 2.15: Lyα brightness as observed by *New Horizons* at 51.3 au, displayed in Mollweide projection using galactic coordinates. The upstream and downstream directions of the IPM are indicated, as well as locations of the Large and Small Magellanic Clouds (white text), and various fast-moving stars (purple text). The Sun's location is indicated by an orange dot. The outlines of three LISM clouds (LIC, G, Blue) are included (in red, pink, and blue respectively). (Image: G. Randall Gladstone.)

The proof-of-concept observation was a success, setting the stage for one of *NH*'s most complex maneuvers to date – capturing the entire sky.

2.4.4 The Entire Sky

From September 2 - 11, 2023 at 56.9 au, Alice spent 10 days to do its first all-sky observation. Ninety Great Circles would be required to completely cover the

sky. In order to preserve the detector from damage when pointing directly at the Sun, they limited the observation to 75 Great Circles, avoiding the 15 circles that passed closest to the Sun. Using the HCCR mode, Alice collected the total photon count integrated across the passband. Figure 2.16 shows the results plotted over Pryor's background scattered solar model, and residuals after they are subtracted from one another.

The top panel of Figure 2.16 shows Lyα observations from across the sky. Taken two years after the 30° proof-of-concept observations and ~ 5.6 au further from the Sun, it is apparent how the Lyα flux has decreased across the board. Note, however, that the scaling of the colorbar was changed between Figures 2.15 and 2.16, exaggerating this impression. There is no data for the 30° swath that passes through the Sun, and instead Pryor's scattered solar model is shown for comparison, plus a 43 R offset to approximate the Galactic Lyα contribution.

Upon detailed comparison of the scattered solar model with the data, Gladstone found that the model fits better on one side than the other, with a roughly 20% difference between the two. This appears to be an observational artifact rather than something physical. The difference may be a result of the fact that *NH* was moving during the 10 days required to complete all 75 sweeps, resulting in a roughly 0.08 au difference between the first and final sweeps. Pryor plans to rerun the scattered solar model using data specific to the day that each observation was done (across the 10 days), rather than using one day's data for the whole model, with hope that this will improve the fit.

As was expected from earlier observations, the all-sky view reveals a Galactic mid-plane dominated by stellar UV sources. In the second panel of Figure 2.16, black dots are placed over UV-bright stars identified in the CUBS catalog (Velez et al. 2023), with sizes according to their expected Alice photon count rates. These

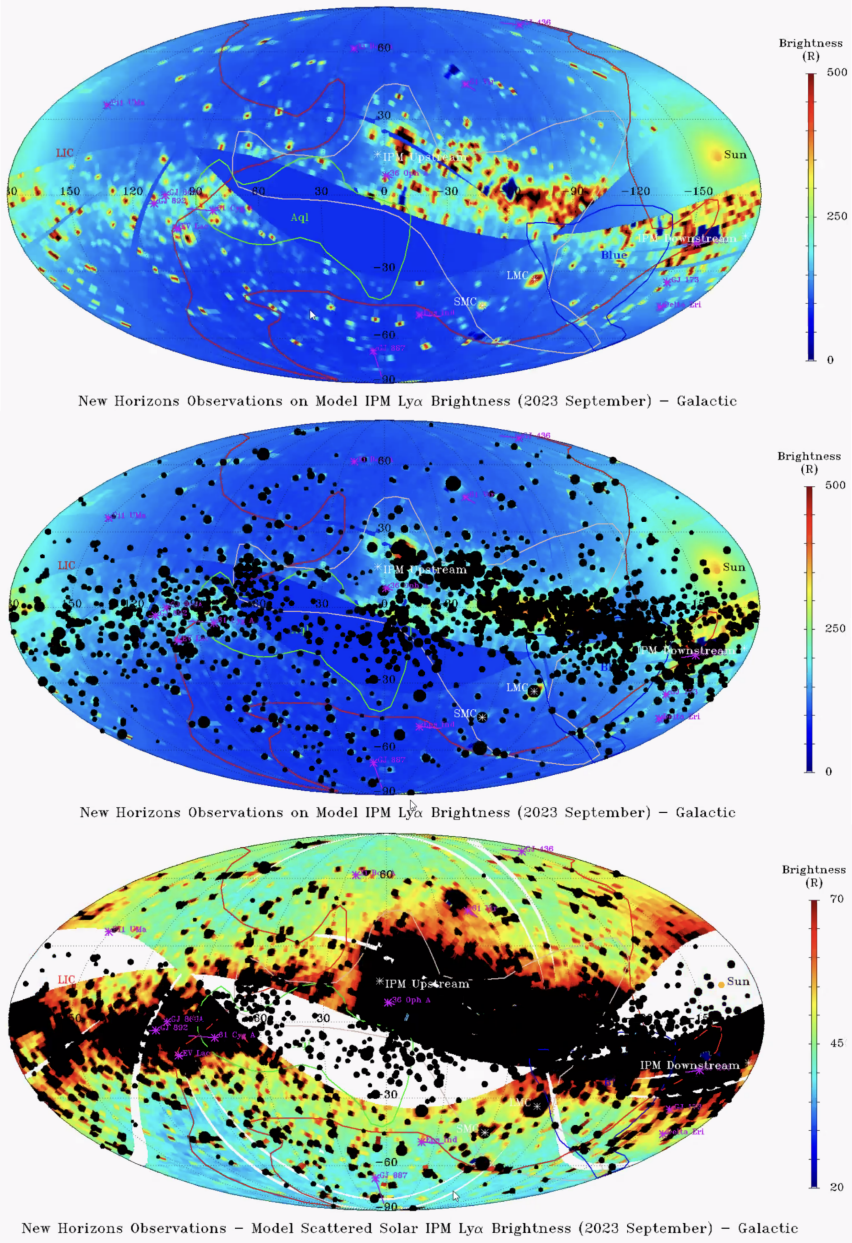

Figure 2.16: Upper: Lyα brightness as observed by *New Horizons*, displayed in Mollweide projection using galactic coordinates. The upstream and downstream directions of the IPM are indicated, as well as locations of the Large and Small Magellanic Clouds (white text), and various fast-moving stars (purple text). Colored outlines mark the boundaries of four LISM clouds (LIC, G, Blue, Aql) in red, pink, blue, and cyan respectively. Data was not taken for the 30° swath that passes through the Sun, and instead a scattered solar model with a 43 R offset is shown. **Middle:** All known UV-bright stars are blotted out with black dots. **Lower:** The scattered solar background model has been subtracted from the data, leaving only residuals. (Image: G. Randall Gladstone.)

CUBS stars are predominantly clustered in the galactic plane, where hot, young A and B stars populate the Milky Way's disk. Ignoring these obvious stellar UV sources, the surrounding Lyα flux matches Pryor's scattered solar model fairly well when an additional 43 R offset is included, as in the upper and middle panels.

In the lower panel of Figure 2.16, the scattered solar model alone has been subtracted from the data, and the residuals are plotted. These residuals are attributable to a roughly isotropic Galactic Lyα contribution of around 43 R, plus possible diffuse sources and sinks due to nearby shocks, the Hydrogen Wall, and LISM clouds. The residuals span 20 - 70 R, which means that possible contributions even as small as 10 R could be significant. It is at this level that we hope to tease out the impact of the LISM cloudscape.

Chapter 3

Methods

3.1 Mapping the LISM

The first step in determining whether *New Horizons* has observed the shadows of LISM clouds is to create a comprehensive map of the cloudscape.

3.1.1 Coordinate System

When *NH* observes the sky, it registers information as if laid upon the interior surface of a vast celestial sphere. It is not obvious how to depict the interior surface of a 3D sphere on a flat page, requiring approximations and transformations, as well as a choice of coordinate system. To match the way *NH* data has been processed, we created our LISM cloud map in galactic coordinates using a Mollweide projection.

Galactic coordinates (Fig. 3.1) are based on a sphere enclosing the Milky Way with the origin at the Sun. Galactic longitude (l) and latitude (b) work similarly to RA and Dec in the equatorial coordinate system. Galactic longitude (l) measures the angle (in degrees) eastward along the galactic equator, and latitude (b) is the angle (in degrees) above the galactic mid-plane. In the example shown in Figure 3.1, galactic longitude lies in the plane of the Milky Way disk, starts at 0° pointing towards the central bulge, then progresses counterclockwise in a circle

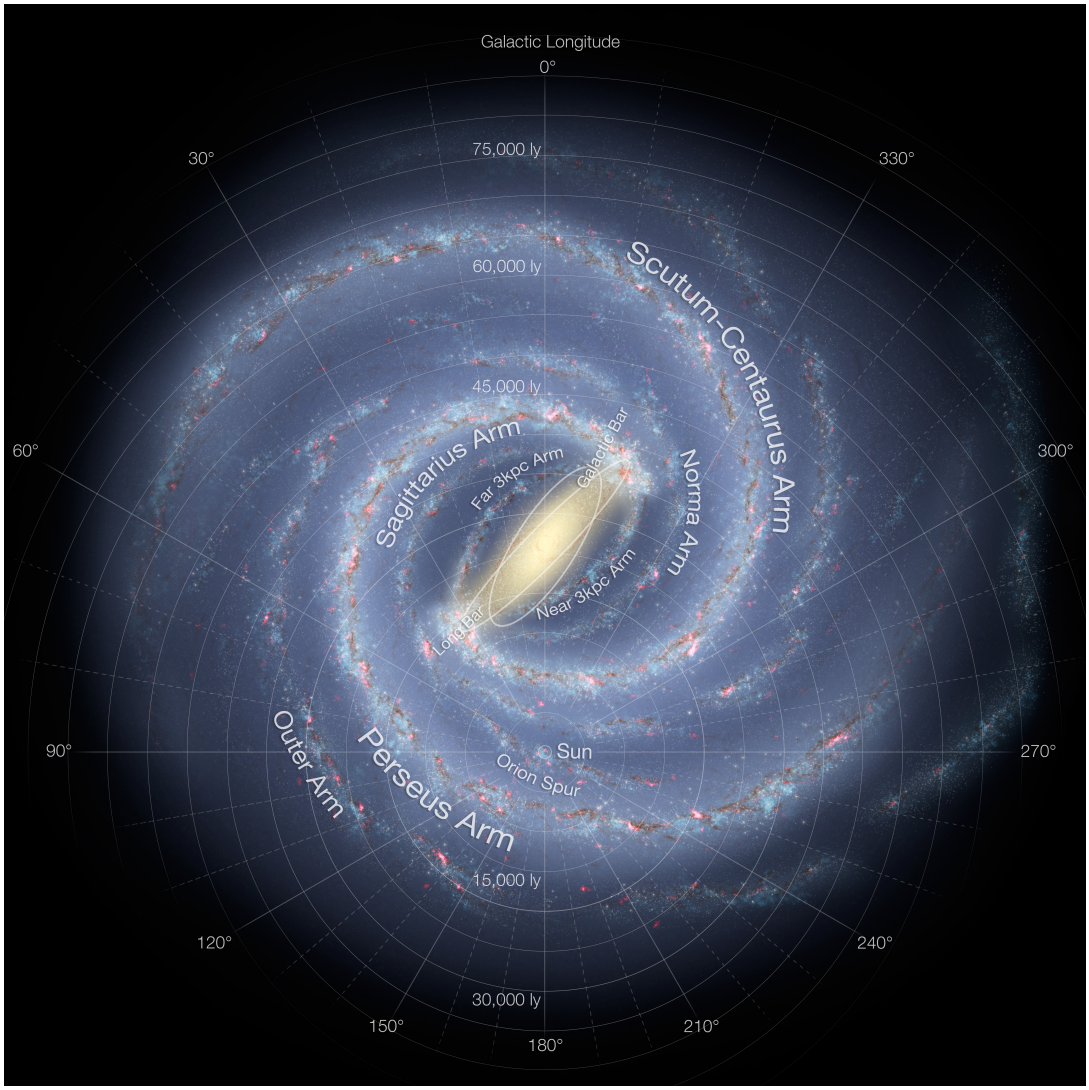

Figure 3.1: Artists depiction of the Milky Way Galaxy overlaid by the galactic coordinate system. A detailed depiction of the locations of spiral arms is included, last updated in 2013 using survey data from ESO's VISTA telescope at the Paranal Observatory. The Sun lies at the center of the coordinate system. A vector of 0° galactic longitude points directly from the Sun to the center of the galactic bulge. Galactic longitude 180° points in the opposite direction, towards the outskirts of the Milky Way. The longitude values increase in the counterclockwise direction. Perpendicular to galactic longitude is galactic latitude (not pictured), which points into (−) and out of (+) the page. (Image: NASA/JPL-Caltech/ESO/R. Hurt.)

until it returns to where it began at 360°. Galactic latitude is not depicted in Figure 3.1, as it moves perpendicular to longitude in/out of the page. The zero of galactic latitude lies flush with the page, centered in the mid-plane of the Milky Way. +90° galactic latitude comes out of the page (called the North Galactic Pole), and −90° goes into the page (toward the South Galactic Pole).

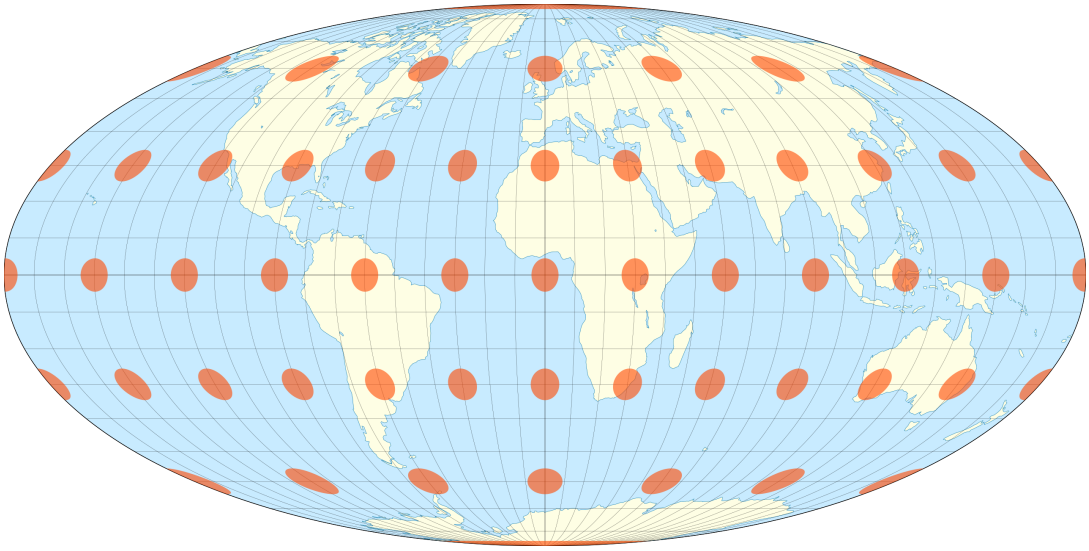

Figure 3.2: Depiction of Earth in a Mollweide projection. The spherical surface of the Earth has been flattened into a 2:1 ellipse, with distortion most pronounced at the perimeter. Tissot's indicatrix of deformation is shown in orange; the amount to which the orange shapes vary from circular indicates the degree of distortion caused by the projection. (Image: Justin Kunimune[1].)

The Mollweide projection is commonly used to map the celestial sphere into a 2D grid while minimizing distortions. Mollweide is an equal-area pseudocylindrical projection, meaning that each grid box is made to encompass the same area. The equator is drawn with a straight horizontal line, and is bisected by a perpendicular, straight central meridian that is half the length of the equator, resulting in a 2:1 ellipse. The meridians are all equally spaced at the equator and compress at the

[1]Creative Commons Attribution-ShareAlike 4.0 International License, `https://creativecommons.org/licenses/by-sa/4.0/`

poles. The meridians at 90° east and west form a perfect circle.

For the following maps and models, we superimpose the galactic coordinate system on a Mollweide projection of the sky, such that the center of the Milky Way bulge from our point of view is located at $(l, b) = (0, 0)$, galactic longitude increases moving to the left, and galactic latitude increases moving up.

3.1.2 Cloud Locations

With our grid system in place, we now have a structure upon which to map the LISM cloudscape. For each of the 15 LISM clouds identified in Redfield & Linsky (2008), we have coordinates that define the boundary of the cloud, and a second set corresponding to points that fall within the cloud. The coordinate points given in these sets did not exactly match my grid system, so my next step was to map them to each other and fill in the gaps.

To do so, I produced a vector running from *NH* through each given line of sight, one sight line at a time, and determined which clouds the vector would intercept. For a given sight line (l, b), I checked the spherical distance ($d_{\rm sph}$, given by Equation 3.1)[2] between that sight line and each coordinate in the first LISM cloud, then I pulled out the minimum value ($d_{\rm sph,min}$),

$$d_{\rm sph} = 2\arcsin\left(\sqrt{\sin^2\left(\frac{b_1 - b_2}{2}\right) + \cos(b_1) * \cos(b_2) * \sin^2\left(\frac{l_1 - l_2}{2}\right)}\right) \quad (3.1)$$

where (l, b) **is** in the cloud if $d_{\rm sph,min} < 1^\circ$

and (l, b) **is not** in the cloud if $d_{\rm sph,min} \geq 1^\circ$.

[2] Astrolib, `https://crossfield.ku.edu/python/_modules/astrolib.html#sphdist`

If the minimum spherical distance between my sight line and the cloud was less than 1°, I considered the sight line to intercept the cloud. We selected 1° as the limit because the original cloud coordinate points are roughly 1° apart. So although my grid of sight lines is spaced much closer together than 1°, as long as they are within 1° of a cloud coordinate point, they can be considered to lie within the cloud. I then repeated this process for every cloud and every sight line, until I could list all the clouds traversed by each sight line. A given line of sight might pass through one cloud, many clouds, or none at all, and so these calculations allowed me to account for the apparent overlapping positions of the clouds on the celestial sphere from the perspective of *NH*. The result (Fig. 3.3) is my reconstruction of the classic *Psychedelic Easter Egg* from Redfield & Linsky (2008) (seen previously in Fig. 1.7).

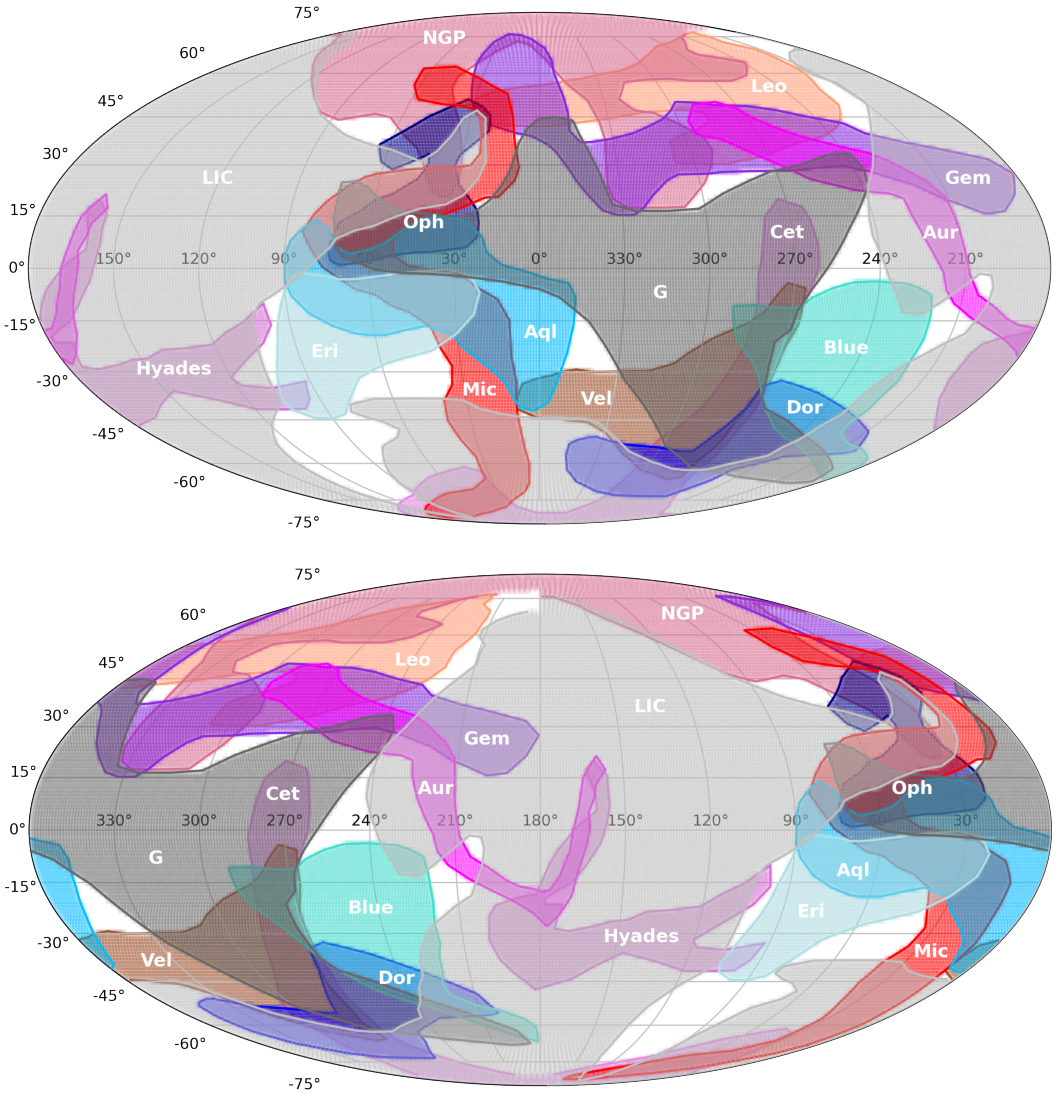

Figure 3.3: These maps take the entire sky and uncurl it onto a flattened Mollweide projection in galactic coordinates (upper panel centered at 0°, lower at 180°). The positions of 15 LISM clouds are shown. Color is used to differentiate between clouds. Data is derived from LISM absorption line measurements made on 157 sight lines using *HST*, courtesy of Redfield & Linsky (2008)

3.1.3 Cloud Column Densities

With knowledge of the locations of LISM clouds across the sky, I next construct an all-sky map of the total column density of hydrogen gas in those LISM clouds.

The LISM clouds are comprised predominantly of hydrogen (with trace amounts of heavier elements), and so we are interested in characterizing the amount of interstellar hydrogen gas contained in the clouds. Density is a measure of the number of particles per unit volume, and is an important parameter for determining how effective the clouds will be at blocking light.

Thinking back to our discussion in Section 1.1.1, we know the locations of the LISM clouds because researchers have looked at the spectra of hundreds of nearby stars, and measured absorption lines that indicate there is gas between us and the star. By examining the relative depths of different absorption lines for a given line of sight, it is possible to determine the total absorption experienced by a beam of light traveling on that line of sight, and consequently, the total density of particles traversed by that beam during its entire journey. For LISM sight lines, we can measure the total number of particles it passed en route. We call this value the "column density" because it can be thought of as the total number of particles contained along a column of space with length equal the star-Earth distance and an area of 1 cm^2. Thus we measure column density as a proxy for sight line averaged density. In this study, column densities are given as the number of neutral hydrogen atoms per square-centimeter.

I gathered all hydrogen column density measurements taken across all LISM clouds from Redfield & Linsky (2008), and calculated the average column density $\langle \log N(\mathrm{HI}) \rangle$ cm^{-2} for each cloud, which is recorded in Table 3.1. The number of available data points per cloud varies significantly due to the angular diameters they each take up on the sky. The Solar System is currently peering out from inside the edge of the LIC, thus the LIC covers more than half of our sky, and LIC absorption lines are visible in the majority of stars observed (79/157). Other clouds take up smaller areas on the sky, which could be the result of the clouds

LISM Cloud Column Densities

Cloud Name	Total Number of Sight Lines	Number of H I Sight Lines	Individual Measurements $\log N(\mathrm{H\,I})$ [cm^{-2}]	Weighted Averages $\langle \log N(\mathrm{H\,I}) \rangle$ [cm^{-2}]
LIC	79	33	17.2, 17.6, 17.8, 17.9, 18.0, 18.0, 17.8, 17.8, 17.9, 17.5, 18.0 18.0, 18.3, 18.2, 18.3, 18.2, 17.7, 18.0, 18.1, 17.8, 18.1, 18.2 18.5, 17.9, 17.9, 18.0, 18.0, 18.2, 18.2, 17.8, 17.9, 18.2, 18.1	17.9
G	21	6	17.6, 17.6, 17.8, 17.8, 18.8, 18.5	17.8
Blue	10	4	17.2, 17.8, 17.9, 18.5	17.6
Aql	9	4	17.8, 17.9, 17.1, 18.1	17.5
Eri	8	4	17.8, 17.9, 18.4, 17.9	17.9
Aur	9	3	17.6, 17.8	17.7
Hyades	14	6	18.0, 17.5, 17.8, 17.6, 17.4, 17.4	17.6
Mic	15	4	17.5, 18.2, 16.9, 18.1	17.4
Oph	6	1	17.5	(17.5)
Gem	10	3	17.9, 17.8, 17.7	17.8
NGP	15	7	17.9, 18.2, 18.2, 17.9, 18.0, 17.9, 18.0	18.0
Leo	7	1	18.6	(18.6)
Dor	4	1	18.1	(18.1)
Vel	7	2	18.8, 18.3	18.5
Cet	5	1	18.5	(18.5)

Table 3.1: Properties of the 15 LISM clouds within 15 pc of the Sun, provided by Redfield & Linsky (2008). As in Table 1.1, clouds are listed in order of their proximity to the Sun. The number of sight lines used to identify each cloud is given. All column density measurements are listed, followed by the weighted average column density, given as the log of the number of neutral hydrogen atoms per square-centimeter. Those clouds with only one sight line with an H I measurement are indicated in parentheses. Since a weighted average is not possible, the listed properties should be considered uncertain. The LIC has the most measurements because the Solar System is believed to currently lie inside the LIC, thus most sight lines pass through the LIC.

being intrinsically smaller, more distant, or just that they happen to be positioned such that we observe them from angles where they appear narrowly confined, like looking at a door edge-on instead of face-on. For example, we observe clouds like Oph and Dor from angles such that they take up only small areas on the sky, and therefore fewer stars exhibit absorption features from those clouds (5 - 6 stars each). Thus, some clouds have few data points due to the available number of sight lines on which stars were observed. Additionally, not all sight lines result in a hydrogen column density measurement. To mitigate this, I take weighted averages where possible, since the values span an order of magnitude and it is easy for a single value to drastically skew the average. Values where only one measurement is available are listed in parenthesis, to indicate they should be considered uncertain.

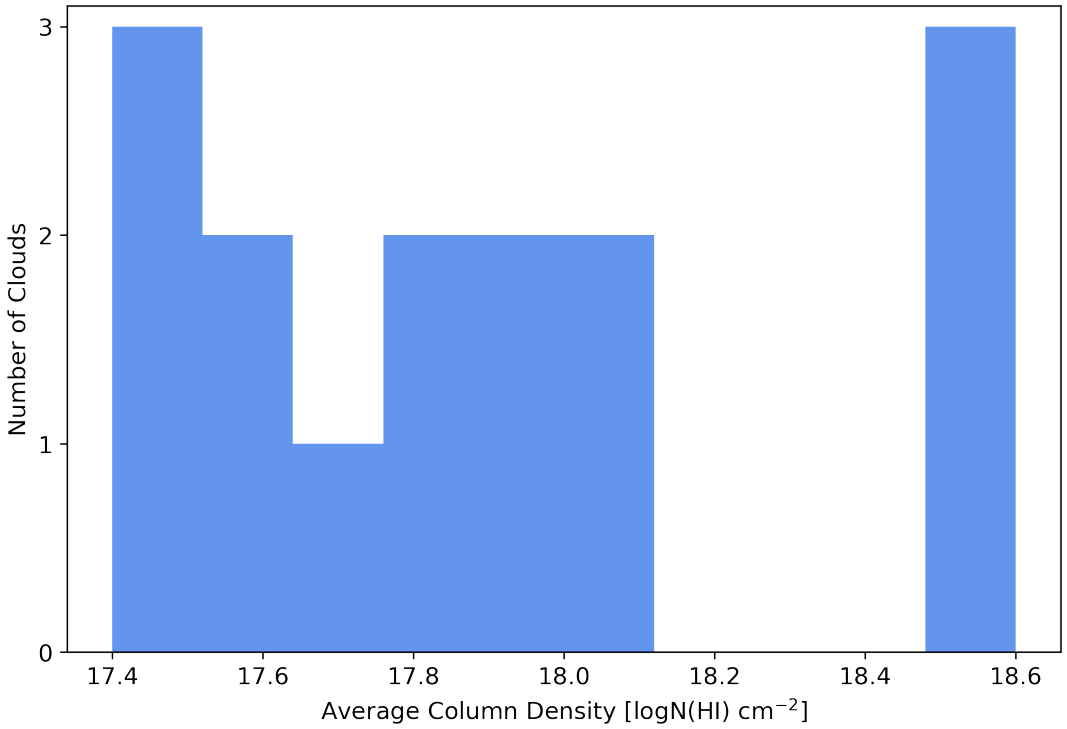

Figure 3.4: Histogram of the average column densities of LISM clouds. The values are closely clustered between log(17.5) and log(18.1), corresponding to a range of $3.16 \times 10^{17} - 1.26 \times 10^{18}$ hydrogen atoms per square-centimeter, as is common for ISM clouds.

Figure 3.4 shows a histogram of the distribution of the LISM clouds' weighted average column densities. They span over an order of magnitude from $10^{17.4} - 10^{18.6}$ N(H I) cm^{-2}, with most clustered at the lower end of the range, and three of the most distant clouds (Leo, Vel, Cet) anchoring the higher end of the range. These hydrogen column densities are much higher than the weighted average LISM column densities for other ions, which range from $\sim 10^{12} - 10^{14}$ (e.g., log(D I) = 13.01, and 13.82 for C II, 13.51 for N I, 14.00 for O I, 12.45 for Mg II, 11.93 for Al II, 13.08 for Si II, and 12.45 Fe II; Redfield & Linsky 2004), confirming the assessment that the LISM is comprised primarily of hydrogen.

An upper limit on the distance to each LISM cloud is shown in Figure 3.5, with color indicating their average column densities. These distances are maximum

limits, set by the distance of the nearest star that exhibits absorption from the cloud. The cloud could extend farther on either side of the star in question, but must at some point lie between the star and the Sun. The closest star to the Sun that shows LIC absorption is 2.6 pc away. However, rather than listing the LIC at a distance of 2.6 pc, it is listed at a distance of 0 pc because it is believed the Sun currently lies inside the LIC. It is interesting to note that the densest clouds are also the furthest.

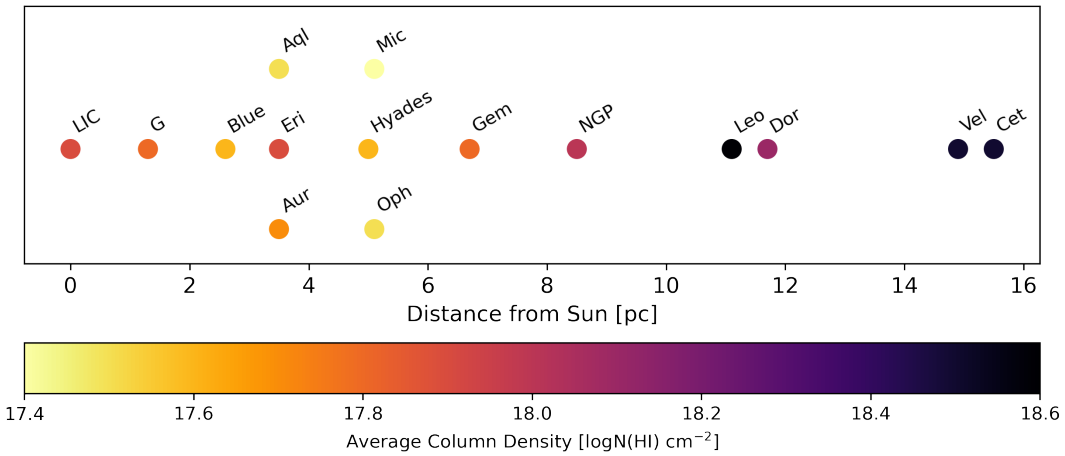

Figure 3.5: Approximate distances to all 15 LISM clouds, with their average hydrogen column densities indicated by color. Distances are set by the distance of the nearest star that exhibits absorption from the cloud, and thus represent maximum limits.

Finally, to map the total column density across the sky, I iterate through every sight line on the sky, summing the column densities of the clouds along each sight line. The results are plotted on a Mollweide projection in galactic coordinates (Fig. 3.6). Total column densities range from $0-10^{18.9}$ N(HI) cm^{-2}. The highest-density regions occur along lines of sight that traverse Leo, Vel, and Cet. Moderate densities are visible where clouds pile up at the boundaries between the LIC and G Cloud, roughly along longitude lines 60° and 270°. At these interaction zones, it is likely that cloud-cloud collisions are creating turbulence and forming smaller,

fragmentary clouds, which will be discussed more in Section 4.2.

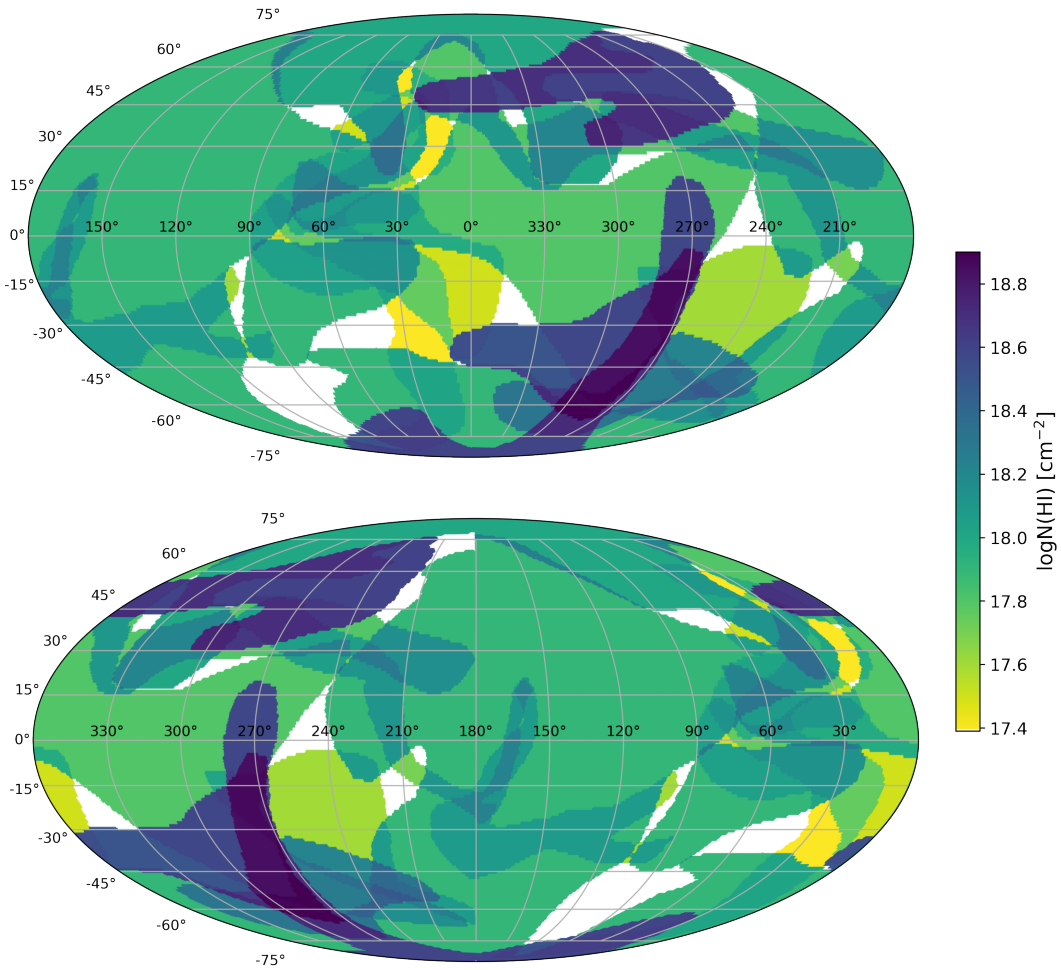

Figure 3.6: These plots model the total hydrogen column density of the sky in Mollweide projection in galactic coordinates, based on observed locations and average column densities of LISM clouds. The upper map is centered at 0°, lower at 180°. Regions where no LISM clouds have been observed appear in white. Sight lines that traverse multiple clouds are depicted in darker shades of green-blue.

3.2 Modeling Radiative Transfer of Lyman-alpha

The next step is to model how light should be affected as it filters through this cloudscape. This is what is known as a *radiative transfer* problem, as it has to do with the physics of photons (electromagnetic radiation) as they move

(transfer) through a medium. The goal of our radiative transfer models will be to determine what the sky will look like from *NH*'s perspective, given a certain quantity and spatial distribution of incident Lyα photons, the number of clouds traversed by each photon, and the column density of each cloud traversed. With these properties known, you can calculate how the photons will interact with the interceding medium.

When a photon enters a medium, its passage through the medium can get blocked in one of two main ways: (1) absorption and (2) scattering. (1) If the photon's frequency corresponds to an energy that exactly matches the energy needed to facilitate an electron transition in the atoms present in the medium, then the atoms may absorb the photon. For this reason, a given medium may be particularly prone to absorbing photons of a specific frequency, while letting photons of different frequencies pass undisturbed. Alternatively, (2) the incident photons may get scattered off electrons in the medium like colliding billiard balls, changing their direction and speed. This exchange of momentum between the photon and electron may result in the photon losing or gaining some amount of energy, which causes a shift in the photon's frequency. In general, a medium that is good at blocking photons is said to have a high opacity (i.e., low transparency), and a medium that lets photons pass easily through has a low opacity (i.e., high transparency).

To explain how these two processes (absorption and scattering) come together, we can use the example of the simplest energy transition of the most abundant element in the universe: hydrogen (which is also the element that makes up the bulk of the LISM clouds). A neutral, ground-state hydrogen atom consists of one proton and one tightly-held electron (in the $n = 1$ orbital). A hydrogen atom can transition into an excited state when it moves its electron up from the $n = 1$

to $n = 2$ orbital (increasing the system's potential energy by 10.2 eV). To obtain the energy necessary to make this transition, the hydrogen atom must absorb a photon with exactly 10.2 eV of energy. This amount of energy corresponds to a photon of wavelength 1215 Å ($E = \frac{hc}{\lambda}$). Thus, when light encounters a cloud of hydrogen, most of the photons of wavelength 1215 Å get absorbed, while the rest of the light passes through relatively unhindered.

The spectrum of light that emerges on the other side of the cloud will not be a full rainbow; it will have a dim patch in the UV range around 1215 Å due to the preferential absorption of those photons. This spectral feature is called an absorption line, because only the photons with the relevant frequency get absorbed, resulting in a dark gap in an otherwise bright spectrum of light. However, some of those 1215 Å photons may also be impacted by scattering, shifting their frequencies each time they scatter. They can scatter tens of thousands of times as they bounce around the cloud. If they are able to scatter enough that their frequency gets pushed substantially far from 1215 Å (i.e., shifting away from the resonant frequency of the absorption line, known as "line center"), then they might be able to escape from the medium after all. Thus, scattering serves to both block light from escaping (by diverting light from its path through the medium, effectively slowing it down or even trapping it) and help light escape (by shifting light away from line center so it can avoid absorption).

In the next section, we explore the theory behind how light is attenuated by absorption while passing through a medium. In Section 3.2.2, we compute the absorption line profile for Lyα. And lastly in Section 3.2.3, we complicate this scenario by introducing the impact of multiple scattering. As a simple starting point, let us assume the clouds are located at the distance of the closest star exhibiting their absorption, and have a uniform thickness with a given average

column density. Instead of the amorphous billowing clouds we see in Earth's skies, picture a rigid, finite slab of gas. This is a gross oversimplification, but is the best approximation we can make given our (current) inability to measure the variation of density and precise dimensions of the clouds. Our radiative transfer model will iterate through every point in our spatial grid of galactic coordinates and determine (1) the amount of galactic Lyα light coming in, (2) the clouds it passes through on its path to *NH*, and (3) the total column density traversed. Our ultimate goal is to perform calculations to determine the amount of galactic Lyα that should survive passage through the cloudscape and arrive at *NH*.

3.2.1 Absorption Theory

As a reminder, absorption occurs when a photon is subsumed into an atom in order to raise an electron to a higher energy level, attenuating the light in the process. We are interested specifically in the Lyα energy transition in hydrogen, which requires a type of absorption called *bound-bound* absorption, in which the electron begins and ends the process bound to the atom (as opposed to ionized). Other types of absorption exist, including *free-free* and *bound-free* absorption, but only become relevant when dealing with hot, ionized media (which our LISM clouds are not) and thus they will not be addressed in this thesis. Our model of bound-bound Lyα absorption uses the following classic radiative transfer equations from Rybicki & Lightman (1979).

The main parameters that determine how opaque a medium will appear to a given photon of frequency ν in terms of absorption alone (ignoring scattering) are: (1) number density of particles *in the appropriate energy state* and (2) the cross section σ of the interaction. A material's opacity due to absorption κ_ν [cm^2 g^{-1}]

is expressed as

$$\kappa_\nu = \sigma_\nu n/\rho, \tag{3.2}$$

where σ_ν is the cross section of the interaction, n is the number density of relevant particles, and ρ is the mass density.

(1) *Number density.* Generally, if a gas has a high density, a photon is more likely to be absorbed; however, the energy state of those atoms is crucial. For a Lyα photon to be absorbed by a hydrogen atom, the atom must have an electron present in the ground state, ready to make the jump up to the first excited state. Even if a Lyα photon is passing through a gas of extremely high density, if all the atoms are completely ionized, then the Lyα photon will pass through unhindered by absorption because there were no bound electrons to do the absorbing. Since number density here is defined as the number of relevant particles per volume ($n = N/V$) and density is mass per volume ($\rho = M/V$), by dividing n by ρ we get the number of relevant particles per unit mass of material.

(2) *Cross section.* The cross section of the interaction is a parameter that describes how likely it is for a photon and an atom to interact. Imagine trying to walk across a crowded subway platform. Aside from the number density of people on the platform, the likelihood of your journey being hindered by other travelers depends on a combination of how big those people are and whether you know any of them (and thus would want to stop and chat). These are the same factors that go determine how easily a photon can move through a gas: number density of gas particles, effective area of each particle, and the strength of the attraction between those particular particles and the photon in question. Cross section is a convenient way to group together effective area and strength of attraction into a single measure of the likelihood of the photon getting stopped en route. A higher

σ_ν means there is a higher probability the photon will interact with the particle, either being absorbed or scattered.

We can describe the amount by which the intensity of a beam of light is attenuated while traveling a distance ds through a medium as

$$dI_\nu = -\alpha_\nu I_\nu ds, \tag{3.3}$$

where I_ν is the intensity of light at frequency ν, and α_ν [cm^{-1}] is the absorption coefficient, defined as

$$\alpha_\nu = n\sigma_\nu \tag{3.4}$$

according to number density and cross section. The absorption coefficient can also be written in terms of mass density and the opacity coefficient κ_ν,

$$\alpha_\nu = \rho\kappa_\nu. \tag{3.5}$$

The classic radiative transfer equation

$$\frac{dI_\nu}{ds} = -\alpha_\nu I_\nu + j_\nu \tag{3.6}$$

describes the rate of change of the light intensity as a function of path length through a medium. For now, we will assume our medium is not emitting light of its own in the UV range, although this will be revisited in Section 4.2.2. We can thus simplify the radiative transfer equation for absorption only by setting the emission coefficient j_ν equal to zero, giving us

$$\frac{dI_\nu}{ds} = -\alpha_\nu I_\nu \tag{3.7}$$

which has the solution

$$I_\nu(s) = I_\nu(s_0)\exp[-\int_{s_0}^{s} \alpha_\nu(s')ds']. \tag{3.8}$$

This formulation shows how incident light (I_ν at the start of the path, when $s = s_0$) is attenuated along its passage through a medium according to the exponential of the absorption coefficient α_ν integrated along the path. From this, we have built intuition for understanding how galactic Lyα radiation incident upon the LISM cloudscape will be exponentially attenuated on its path due to absorption, as characterized by the number density of neutral, ground-state hydrogen atoms and their probability of interaction.

Now we move on to explain how we calculate the resultant intensity that will exit the LISM cloud as an absorption line spectral feature.

3.2.2 Absorption Lines

We are taught that for an atom to move its electron to a higher energy state, it needs to absorb a photon of *exactly* the correct wavelength to provide the needed energy. We would expect, then, that the spectral line for the Lyα energy transition should look completely vertical – a thin, dark delta function excised neatly from the broader spectrum. Spectral lines, however, are never delta functions, but instead appear broadened according to many factors, including (1) natural broadening, which is imposed by quantum mechanics, and (2) Doppler broadening and (3) pressure broadening, which are both functions of the properties of the gas.

(1) *Natural broadening* of the line occurs due to the inherent uncertainty in the quantum energy state of the particle at any given moment. Due to the degeneracy between position and momentum according to the Heisenberg Uncertainty Princi-

ple ($\Delta E \Delta t \geq \hbar/4\pi$), we cannot know the exact energy state of a particle (E) at a precise moment in time (t). This creates an inherent uncertainty ΔE in the energy level. The shape of a naturally broadened line is described by what is known as a *Lorentz profile*. A Lorentz profile is narrow at its peak and slopes steeply down on either side, but never quite hits zero, resulting in extensive (although vanishingly small) wings. It is characterized by the parameter γ, the profile's half width at half max (HWHM).

(2) *Doppler broadening* (also known as thermal broadening) is the result of the thermal movement of particles in the medium. The hotter a gas is, the higher the kinetic energy of its particles, and the larger the spread in their velocities. The frequency of an absorption line will be shifted by a factor of $\Delta\nu/\nu = v/c$ depending on whether a given particle is moving towards or away from the observer, as a result of the Doppler effect. Because a gas cloud is a collection of many particles with slightly different velocities (with a distribution given by the Maxwell-Boltzmann distribution), it results in a superposition of many different Doppler-shifted lines, which causes apparent broadening in the spectral line.

(3) *Pressure broadening* is a function of the density of the material. A dense gas will exert a higher internal pressure on its particles, leading them to bump into each other more frequently, which can change both the exact energies associated with different electron orbital states, and the effective lifetime that an electron can remain in those states. Both Doppler and pressure broadening are described by a *Gaussian profile*, which is a bell-shaped curve characterized by its HWHM, σ. (Note, this is different than σ_ν from Section 3.2.1.)

The foundational shape of all spectral lines is the Lorentzian profile, due to natural broadening caused by intrinsic quantum effects. Depending on the density and temperature of the gas, this underlying Lorentzian profile may then be con-

volved with a Gaussian profile due to additional Doppler and/or pressure broadening. The convolution of these two profiles is known as the *Voigt profile*, an example of which is pictured in Figure 3.7.

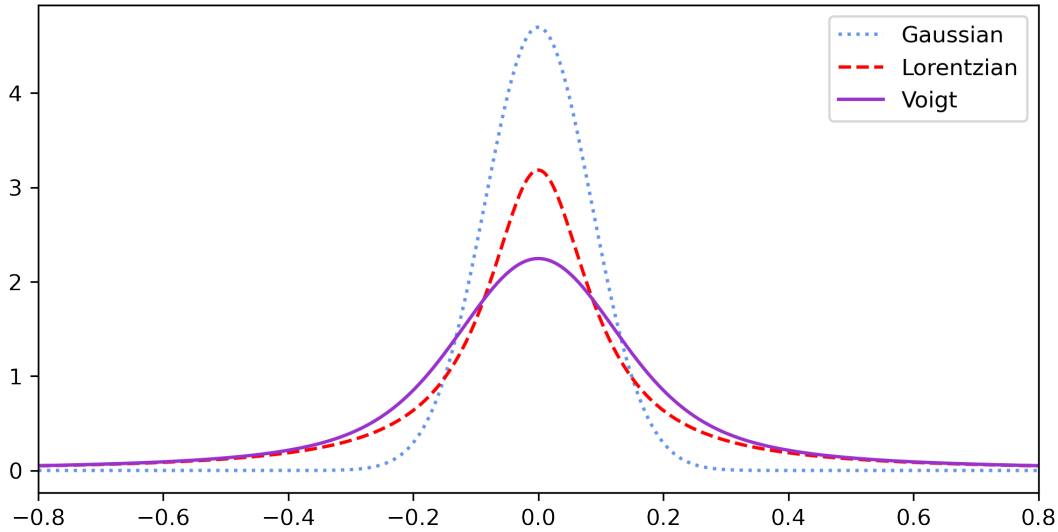

Figure 3.7: Comparison of Lorentzian, Gaussian, and Voigt profiles. The Voigt profile is a convolution of the other two.

The Voigt function,

$$H(a,u) = \frac{a}{\pi}\int_{-\infty}^{\infty} \frac{e^{-y^2}}{a^2+(u-y)^2}dx, \tag{3.9}$$

is used to compute the intensity of an atomic absorption line profile, according to the Voigt profile, which is written

$$\Phi(a,u) = \frac{H(a,u)}{\Delta v_D\sqrt{\pi}}. \tag{3.10}$$

The Voigt profile is dependent on damping parameter $a = \frac{\Gamma}{4\pi\Delta v_D}$ and Doppler width frequency offset $u = \frac{v-v_0}{\Delta v_D}$.

We use the `VoigtAstroP()` method from the `PyAstronomy`[3] (Czesla et al. 2019) model suite in order to model the Voigt profile of a Lyα emission line, shown in Figure 3.8. The calculation is parameterized in terms of central wavelength, damping parameter, oscillator strength, and Doppler width frequency. We use the following values from the literature:

- Average central wavelength $\lambda = 1215.67$ Å from Morton (2004). Note, Lyα is technically a doublet: 2 transitions with wavelengths 1215.6736 Å and 1215.6682 Å, which are very close together and not resolvable. Consequently, we use the doublet mean (average wavelength 1215.6700 Å) as our central wavelength.

- Damping parameter $2\gamma = 6.172 \times 10^{-12}$ cm, the full width at half max (FWHM) of the Lorentzian profile. This is derived from the spontaneous decay rate $\gamma = 6.265 \times 10^{8}$ s^{-1} from Morton (2004), which can be re-expressed as the HWHM of the Lorentzian profile, $\gamma = 3.086 \times 10^{-12}$ cm.

- Oscillator strength $f = 4.164 \times 10^{-1}$ from Morton (2004). The oscillator strength of Lyα is a quantity expressing the probability of hydrogen absorbing or emitting light as its electron transitions between the first and second energy levels. It is an indicator of the strength of the spectral transition. Every possible transition has a unique oscillator strength. Usually labeled f_{lu} (lower to upper for absorption) or f_{ul} (upper to lower for emission), it is related to the statistical weights in each state: $(g_u)(f_{ul}) = (g_l)(f_{lu})$. The larger the value of f, the more likely the transition will occur.

- Doppler width frequency $b = 10.82$ km s^{-1}. Redfield & Linsky (2004) observe the mean b-value for deuterium in the ISM to be $b_{\text{deuterium}} = 7.65$

[3] `https://github.com/sczesla/PyAstronomy`

km s^{-1}. Knowing that the mass of deuterium is twice that of hydrogen, we multiply the deuterium b-value by $\sqrt{2}$ to get the b-value for hydrogen ($b_{\text{hydrogen}} = 10.82$ km s^{-1}), as shown below:

$$b_{\text{deuterium}} = \sqrt{\frac{2kT}{m_{\text{deuterium}}}} = \sqrt{\frac{2kT}{2m_{\text{hydrogen}}}} \rightarrow b_{\text{hydrogen}} = \sqrt{2} b_{\text{deuterium}}$$

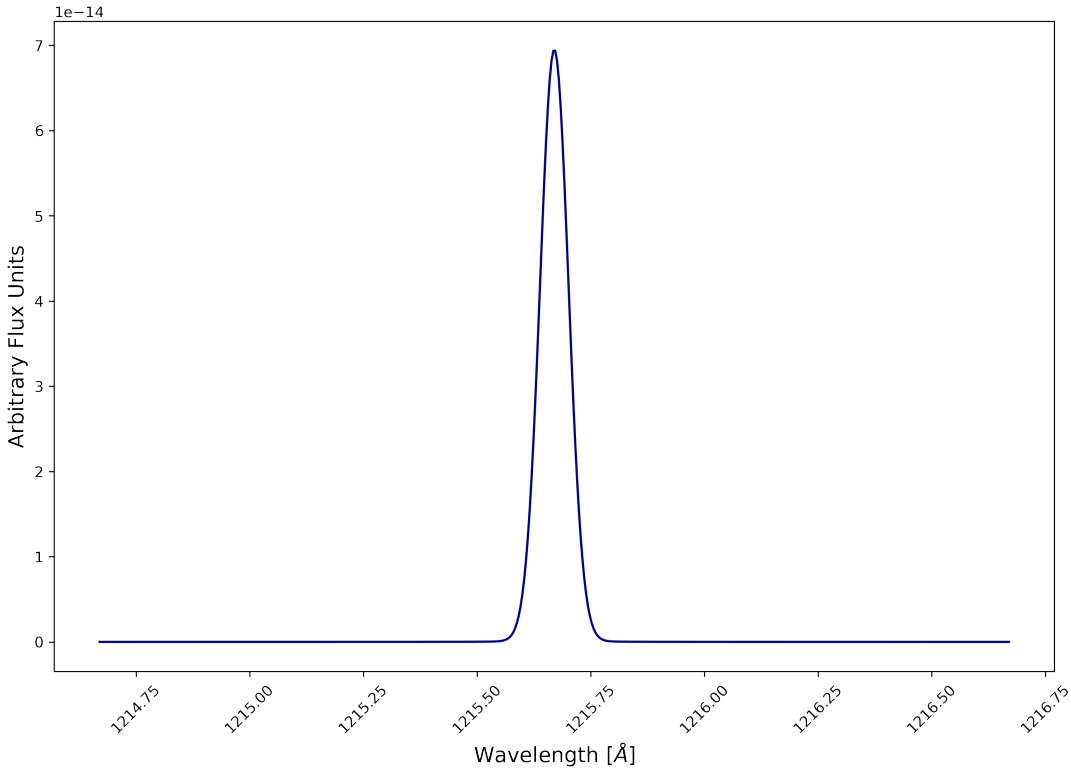

Figure 3.8: Sample Lyα emission line generated using the `VoigtAstroP()` method from `PyAstronomy`.

To turn the Voigt emission profile into an absorption profile, we start by assuming an incident flux of $F_i = 43$ R from the literature (Gladstone et al. 2021) and compute the final flux,

$$F_f = F_i e^{-\tau} \tag{3.11}$$

according to the exponential of τ, where $\tau = \Phi(a, u) N_j S$ brings together the Voigt profile $\Phi(a, u)$, the total LISM column density along the line of sight N_j, and the integrated absorption cross section S. In Figure 3.9, we plot a range of sample modeled absorption features. In this toy model, we assume a narrow ($\sim$ 1 Å) "top hat" emission spectrum centered on 1215.67 Å with a radiative flux of 43.1 R, depicted by a thick line. This radiation is incident on hypothetical LISM clouds with neutral hydrogen column densities ranging from of $10^{17.4} - 10^{18.9}$ N(H I) cm^{-2}, and the transmitted flux F_f is plotted as narrow lines. In general, absorption features are initially dominated by the Gaussian component of the Voigt profile, growing deeper as column density increases, until the point where they saturate and flatten at the bottom, and then they start to grow outwards as the Lorentzian wings become more prominent. In this example plot, a deep Lyα absorption feature is apparent at every column density, with a flat base indicating saturation and total absorption of those wavelengths. As the column density of the medium increases, the Lorentzian wings grow stronger, and the integrated transmitted flux decreases.

As we calculate the absorption from each cloud, we can expect the absorption lines to trough at slightly different wavelengths depending on the cloud, because each cloud has a unique bulk velocity relative to us, and thus the spectral line as a whole will be Doppler shifted (Note: this is different than Doppler broadening due to internal thermal motion of atoms inside each cloud). I could have adjusted for this Doppler shift by converting the central wavelength of the line from $\lambda_0 =$ 1215.67 Å into a Doppler-shifted λ using the formula for Doppler shift: $v/c = \Delta\lambda/\lambda_0$. With typical cloud velocities of $\pm$20 km s^{-1} (Redfield & Linsky 2008), we can estimate a Doppler shift of $\Delta\lambda \approx \pm 0.08$ Å. The resolution of Alice is so poor in comparison (3.6 Å) that a Doppler shift of this magnitude would not be

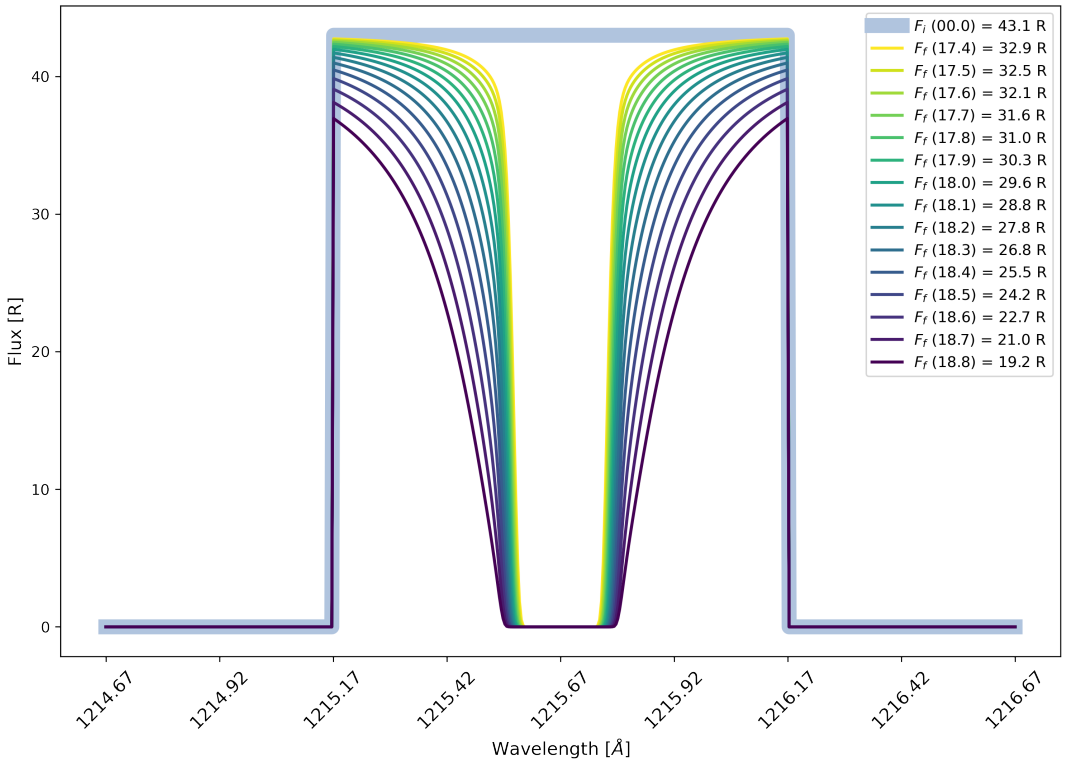

Figure 3.9: Sample Lyα absorption lines (thin) resultant from a top-hat emission source (thick) of $F_i = 43.1$ R that has passed through a medium of a given column density. Column densities range from $17.4 - 18.9$ $\log N(\mathrm{H\,I})$ cm^{-2} and are differentiated by color. The legend gives final integrated flux values (F_f) as a function of column density.

noticeable, and is therefore not accounted for in our calculations. The absorption models resulting from these calculations are provided in Chapter 4.

3.2.3 Multiple Scattering

In our basic absorption model, we made the assumption that there are only two ways that incoming Lyα photons will interact with ISM clouds: either being absorbed or transmitted. However, we can approach a more realistic model if we include a third option: being scattered. Lyα photons that encounter atoms frequently bounce off the atoms into new directions. Sometimes they lose or gain small amounts of energy during the collision, changing their wavelength.

Since collisional probability (cross section) is wavelength-dependent, the change in energy that occurs with each collision in turn changes the likelihood of that photon interacting with the next hydrogen atom. Photons that get absorbed by hydrogen are eventually re-emitted, so essentially all hydrogen can do to photons is scatter them. Dust, on the other hand, can both absorb (permanently) or scatter photons. Any individual photon could experience one scattering or millions of scatterings before it finally gets absorbed by an atom or reaches the edge of the cloud and escapes. This process is called *multiple scattering*, and it results in major uncertainty as to how many Lyα photons incident on a cloud will actually escape the cloud, and in what directions they will be traveling when they do.

Figure 3.10 shows a sketch of the geometry of the LISM as a 2D slice through the Galactic mid-plane, centered on the Solar System. The yellow arrows represent isotropic galactic Lyα photons incident on the LISM cloudscape, while the red, green, and blue arrows show possible photon paths through the cloudscape. Incident light may be transmitted directly through the clouds to arrive at *NH*'s detector, as shown by the green arrow. Light may also be attenuated due to absorption, stopped in its tracks like the right-most red arrow (upper right quadrant near Mic). These two options – transmission and absorption - are well characterized in the preceding sections on basic absorption-only radiative transfer. However, photons may also experience scattering, which can remove incident photons from the line of sight (e.g., red arrow in the Blue Cloud, lower left quadrant), or bumping new photons from off-axis trajectories *into* the line of sight (e.g., blue arrow in Hyades Cloud, upper left quadrant). The arrows are grossly exaggerated in scale, but the premise remains: scattering processes need to be taken into account, in addition to absorption/transmission, to achieve a more physical radiative transfer model. We can anticipate that scattering would blur the boundaries

seen in Figure 3.6 by sending photons into lines-of-sight where they would not otherwise have been found.

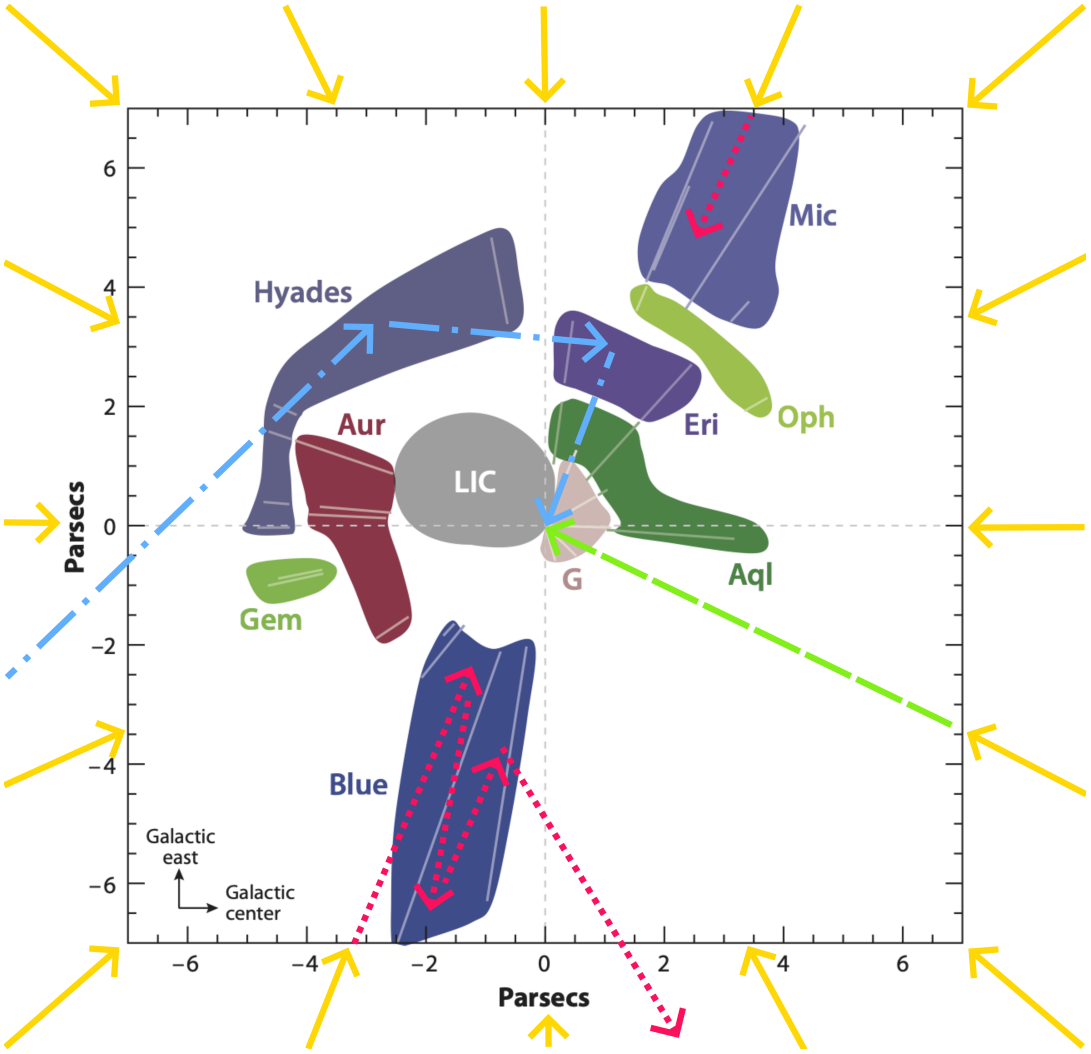

Figure 3.10: A schematic of the geometry of our model, with the Sun located at (0,0). Ambient Lyα radiation arrives isotropically from all directions in the Galaxy (yellow arrows), filters through the LISM cloudscape, and either (i) travels unobstructed to *New Horizons* on a direct line of sight (green dashes), (ii) is absorbed or scattered away (red dots), or (iii) is scattered from an indirect line of sight into a direct line of sight (blue dot-dash). All three must be accounted for by the model. Plot modified from Frisch et al. (2011).

Thoroughly modeling the radiative transfer of Lyα can be complex because it depends on the kinematics, composition, temperature, and geometry of the

medium the light travels through. Early analytical works were confined to highly simplified models, such as Osterbrock (1962), Harrington (1973), and Neufeld (1990), which compute the emergent spectrum of Lyα photons escaping an optically thick, homogeneous, static, dust-free, infinite slab. Later numerical attempts at incorporating multiple scattering sought to estimate the fraction of incident photons that eventually exit a medium, known as the *escape fraction*. Used mostly in extragalactic contexts, models of this variety have been highly successful in explaining observations of Lyα escaping from galaxies at a variety of redshifts and luminosities; however, they encounter a degeneracy between the fraction of neutral hydrogen in the cloud and the escape fraction assumed (e.g., Dayal et al. 2010a,b). To break this degeneracy, it becomes necessary to actually incorporate scattering into radiative transfer calculations, instead of just assuming a fixed escape fraction. Numerical methods were developed throughout the 1960s which, through iteration and application to different geometries, have led to the standard usage today of Markov Chain Monte Carlo (MCMC) algorithms to perform the multiple scattering. MCMC makes it possible to follow the unique path of each individual photon, calculating its unique probability of scattering that changes with each step through the medium, until it eventually escapes or is absorbed. The early 2000s have seen the proliferation of MCMC models, but many are applicable only to certain geometries or regions of parameter space (e.g., spherical symmetry, clumpy/inhomogeneous media, 1D geometry, low column densities, no dust, etc.).

Markov Chain Monte Carlo Codes

We initially explored the MCMC code `LyaRT` from Orsi (2010), which models multiple scattering through a gaseous medium for extragalactic contexts, drawing

upon previous work by Zheng & Miralda-Escudé (2002), Verhamme et al. (2006), Dijkstra et al. (2006), and Laursen et al. (2009). The parameters input into the code are emission frequency, central frequency of the Lyα line, the thermal velocity of the gas in the ISM cloud, the gas temperature, and the scattering cross section (which is based on the oscillator frequency and Einstein coefficient for the Lyα transition). They convolve the cross section with the velocity distribution of the gas to get the cloud's optical depth for Lyα. With knowledge of the hydrogen cloud column density, they create a Voigt scattering profile, representing the probability that photons of a given frequency will experience scattering. The Voigt profile has a central Gaussian core and power-law damping wings. This form indicates that photons with frequencies near line center have a high scattering cross section, whereas photons with frequencies in the wings are more likely to escape. Scattering events are coherent (meaning the photon frequency is the same both before and after scattering) only in rest frame of the atom, not for the observer.

At the base of a MCMC simulation is a 3D grid, where each cell has been filled with gas of some assigned neutral hydrogen density, temperature, bulk velocity, and emissivity (probability of emitting Lyα photons). You can send photons into the grid with a random distribution of directions and frequencies, and the code follows each photon's path from scattering to scattering and records its final frequency if the photon escapes. In the case of Orsi (2010), they assume solar metallicity to obtain the mass of dust in the cloud. This allows them to estimate the albedo of the dust grains, which determines the likelihood of scattering or absorption.

Computing whether and how the photons scatter off hydrogen atoms is complicated by the fact that all gas atoms in the cloud are moving with a Maxwell-Boltzmann distribution of velocities and directions, so each atom "sees" the in-

coming photon moving with a different frequency due to a unique Doppler shift. The cross section for scattering is frequency dependent, thus the probability of scattering will depend on the frequency of the incident photon and the relative velocity of the hydrogen atom. This code assumes the incoming and outgoing frequency is the same in the rest frame of the photon, although in reality a little energy is sometimes lost during the collision as the photon transfers momentum to the atom. However, this *recoil effect* is determined to be negligible for the applications being studied.

Once the velocity of the atom is chosen, the code performs a Lorentz transform to put the direction and frequency of the photon into the rest frame of the atom; then at the end of the scattering interaction, the direction and frequency of the photon is transformed back into the lab frame. The code tracks one photon at a time, following its path from scattering to scattering until it is finally absorbed or escapes. Then the process is repeated with the next photon, up to several hundred thousand photons until one is satisfied with the realism of the result. The number of scatterings could be tens to hundreds of millions. This is quite computationally expensive.

The final output of the code includes the frequency and position of all photons at the moment they escape or are absorbed. This allows one to calculate the emergent spectrum and escape fraction of photons. The results of `LyaRT` were tested and validated against analytical solutions from Harrington (1973) and Neufeld (1990).

New Geometries

We aimed to use the methodology of `LyaRT` to compute multiple scattering through the LISM cloudscape, but the geometries available (e.g., Fig. 3.11) in

the code were relevant only to extragalactic targets, which generally consist of a point-like emission source (e.g., an AGN) propagating through a spherical shell of gas (e.g., the surrounding galaxy and intergalactic medium), as seen by a distant external observer. In contrast, our desired geometry (Fig. 3.12) reverses this picture, with a shell of emission (i.e., isotropic Galactic Lyα) propagating inwards through discrete clouds (the LISM) to a point-like observer at the center of the cloudscape (NH). To apply the MCMC-based methods used in `LyaRT` to our unique geometry, we needed to find a code that would allow full customization.

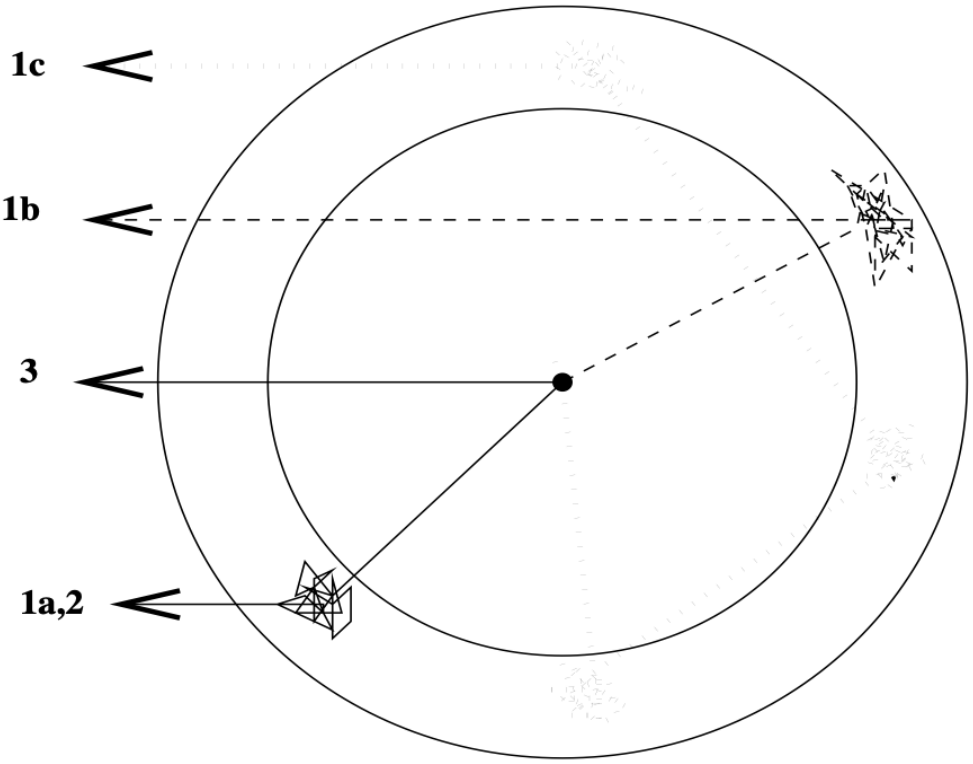

Figure 3.11: Example of a typical extragalactic geometry for a MCMC Lyα scattering code, in which a centrally-located source propagates through a spherical shell of gas. Various pathways of individual photons are depicted, ranging from no scattering (3) to maximal scattering (1c). In this scenario, the observer is located on the left at infinity. (Image: Verhamme et al. (2006).)

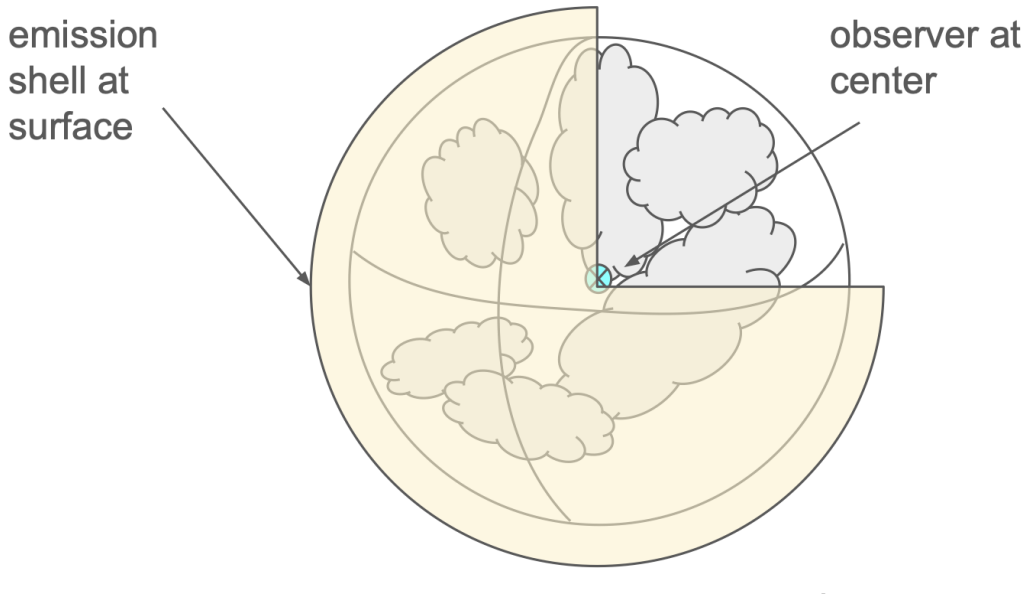

Figure 3.12: A simplified sketch of the geometry of our LISM cloudscape, from the perspective of an MCMC code. We aim to model an isotropic, homogeneous emission source originating from a spherical shell around the cloudscape, propagating inwards to meet an observer located at the center of the cloudscape.

Tiny Lyman Alpha Code

We continue our investigation using a multiple scattering MCMC code known as the Tiny Lyman Alpha Code (`tlac`) from Gronke & Dijkstra (2014) because, although built for modeling extragalactic sources, it allows full configurability. The parameters accepted by `tlac` include hydrogen number density, gas temperature, dust content, emissivity, and bulk motion. The code allows for the custom construction a 3D grid, enabling you to fill each cell with gas by assigning it values for the above parameters.

The pipeline for `tlac` is as follows: (1) Emit photons in random directions according to some emission source distribution in frequency-space and physical space. (2) Calculate optical depth τ from a distribution, then convert τ to a distance the photon travels before interaction. (3) Calculate the probability of

interaction. (4) If interacting with dust, determine if the photon is scattered or absorbed. (5) If scattered, generate a new random direction for the photon, and determine its change in frequency. (6) Return to Step 2 and repeat until the photon is absorbed or exits the grid. The outputs of `tlac` include the position of last scatter (in cm), direction of escape (normalized to 1), frequency at escape (given as $x = (\nu - \nu_0)/\Delta\nu$), distance since last scatter, total number of scatterings until escape, and frequency of emission (same units as x above).

`tlac` combines previous radiative transfer algorithms which (a) treat each cloud as a virtual particle with its own phase function and redistribution and (b) actually track the path of the photons through the clouds. The code has been tested extensively, comparing results to analytical solutions from Neufeld (1990) and results of other MCMC codes.

We have yet to fully implement `tlac` to incorporate into our models, but we present our initial explorations in Section 4.3.

Chapter 4

Models

Here we present our models of galactic Lyα emission after passage through the LISM cloudscape as seen from *NH*'s vantage point. We begin by working with the simplest case, line of sight absorption-only radiative transfer. By this, I mean that we are considering only the light that is removed from the line of sight (whether through absorption or being scattered away), and not worrying about light that might be scattered into the line of sight (such as would require a multiple scattering MCMC model). Since the exact source and intrinsic brightness of Lyα emission is not known, we explore two different scenarios: isotropic emission (Section 4.1) and anisotropic emission (Section 4.2). In the isotropic scenario, we vary the distance of the emission source to explore how far away the background emission may be originating from. In the anisotropic scenario, we vary the location of Lyα emission to account for the possibility that, in addition to a distant, isotropic background source, Lyα may also be originating within the cloudscape itself due to cloud-cloud collisions. We conclude the chapter by discussing our ongoing inquiry into the effects of multiple scattering (Section 4.3).

4.1 Isotropic Emission

The argument for isotropic Galactic emission is based on the Great Circle Lyα measurements obtained from *NH*'s Alice UV spectrograph (Gladstone et al. 2015,

2018, 2021), which revealed a small Lyα flux in excess of the flux expected from scattered solar light, apparent in roughly equal measure in all directions. This apparently isotropic flux could indicate isotropic emission. This assumption is questionable for multiple reasons.

- The Great Circle ribbons covered only a small range of latitudes and longitudes. To generalize these strips of measurement to the entire sky is a big leap. In fact, the long awaited all-sky measurements measured anisotropy in flux across the sky on the order of 10 - 70 R.

- If we do assume that the same flux is seen in all directions, then for an isotropic flux to make it through a decidedly anisotropic, clumpy cloudscape, the emission source must have been clumpy as well (in opposite measure).

That said, here we begin with the simplest model possible, one that assumes an isotropic incident flux, just to get a sense of what the clouds do to a smooth background source, before we add complicating factors.

Using the latest *NH* Great Circle measurements (Gladstone et al. 2021), **Model 1** assumes a 43 R isotropic flux of Galactic Lyα incident upon the LISM cloudscape from a distance of 16 pc (just exterior to the cloudscape). We model how much of the incident light should be removed via radiative transfer processes as it filters through the cloudscape, allowing us to estimate the magnitude and spatial distribution of light that should ultimately escape the cloudscape and reach the Alice detector. We treat each cloud as a homogeneous stationary slab of hydrogen gas with known borders and an average column density given by Table 3.1.

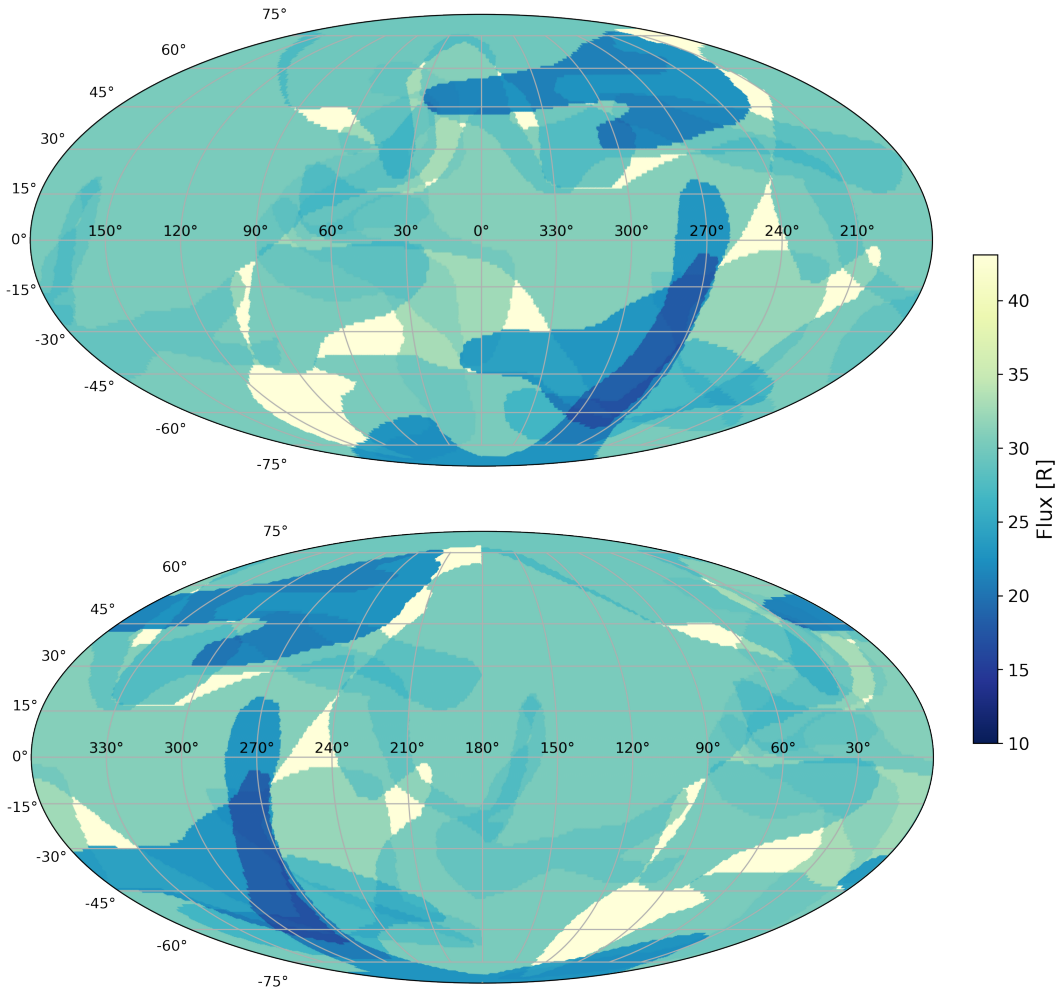

Figure 4.1: Model 1. These plots show the results of applying our line of sight absorption-only radiative transfer model to a Galactic Lyα flux of 43 R incident upon the LISM cloudscape from just exterior to the cloudscape. The upper map is centered at 0°, lower at 180°. The level of absorption depends on the total line of sight column density.

This model of the transmitted Lyα flux exiting the cloudscape is plotted in Mollweide projection in galactic coordinates in Figure 4.1. Flux values are given in Rayleighs. Passage through one cloud reduces the flux by $\sim$ 10 - 20 R. Darker regions where less flux escapes correspond to areas where multiple LISM clouds overlap, resulting in high line of sight column densities which increase the prob-

ability of absorption. Sharp boundaries between cloudy and non-cloudy regions are noticeable on the 10 - 20 R level.

4.1.1 Varying Distance of Emission

The average distance Lyα travels before interacting with a particle (known as its *mean free path*) is short, and it may be unrealistic to assume much Lyα radiation from the Galaxy even makes it to the vicinity of the Sun. In **Model 1**, we assume isotropic emission just exterior to the cloudscape, as if there were a spherical shell of emission centered on the Sun with a radius of 16 pc. To explore the impact of emission originating *within* the cloudscape, in **Model 2** we pull in the radius of the emission shell $1 - 2$ parsecs at a time (Fig. 4.2) and plot the resulting hydrogen column densities encountered by that radiation (Fig. 4.3) and the final transmitted fluxes (Fig. 4.4).

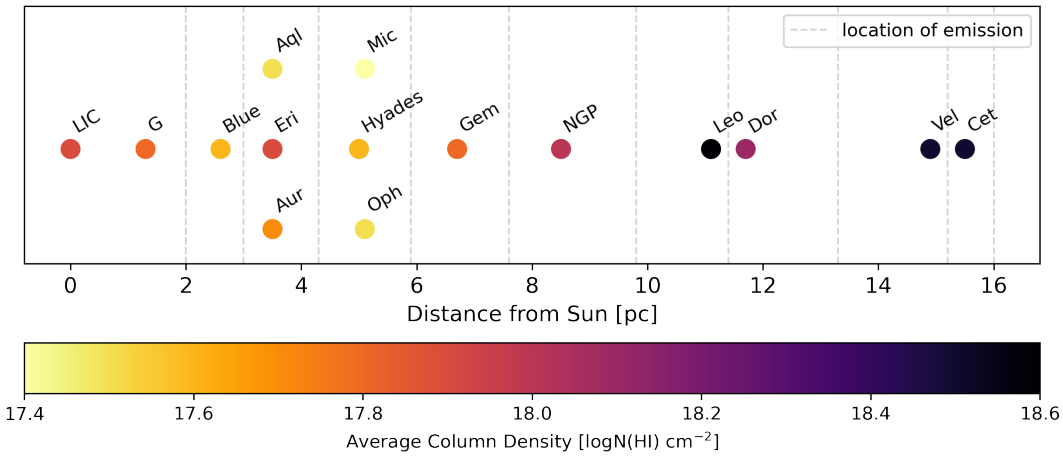

Figure 4.2: Approximate distances to all 15 LISM clouds, with their average hydrogen column densities indicated by color. Distances are set by the distance of the nearest star that exhibits absorption from the cloud. The radii of emission used in **Model 2** are indicated by gray dashed lines.

We begin with a radius of emission at $r = 2$ pc, just exterior to the LIC and G

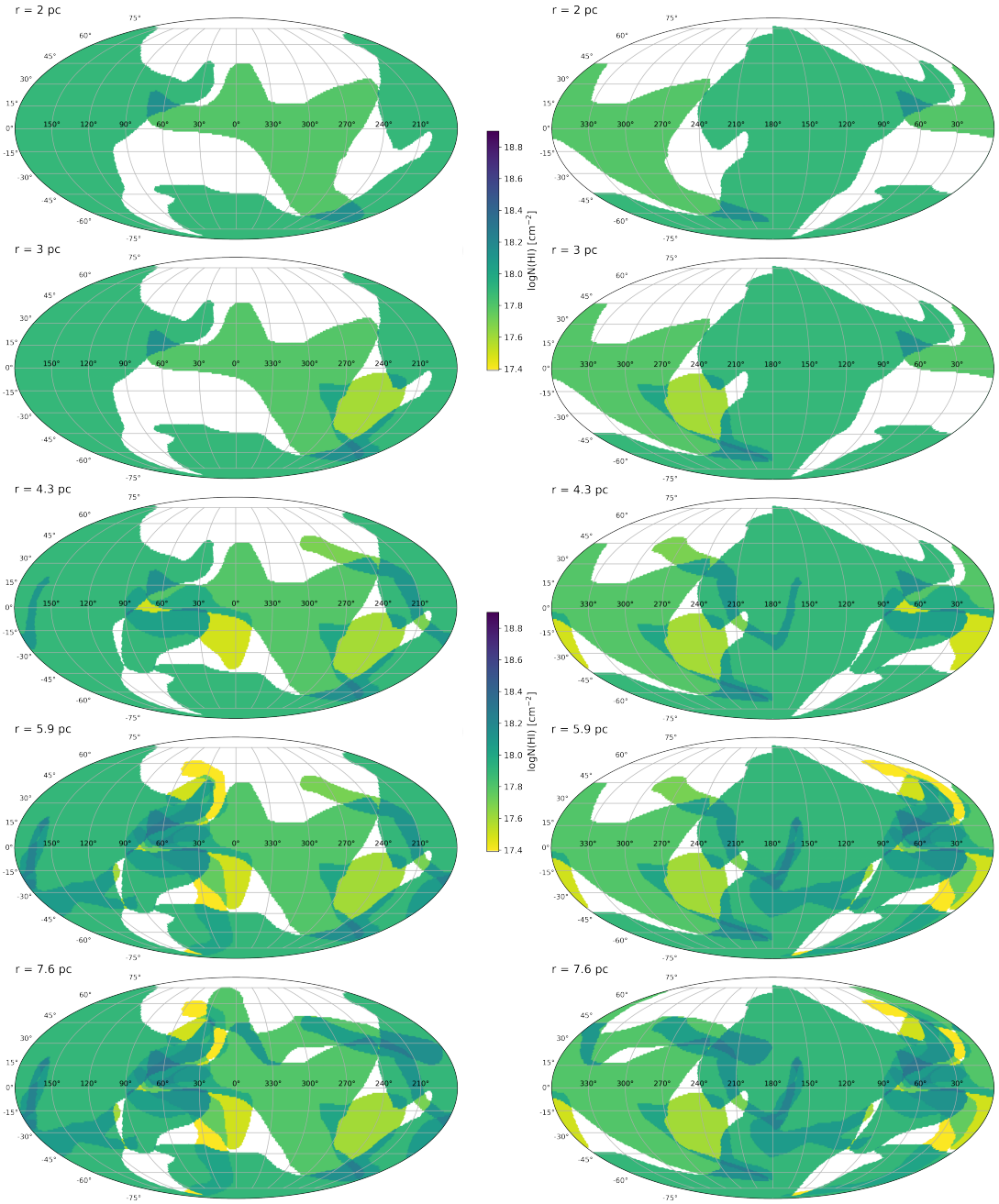

(a) Radius of screen of emission at $r = 2, 3, 4.3, 5.9, 7.6$ pc.

Figure 4.3: These plots show the total column density of LISM clouds encountered by an isotropic spherical shell emission source at a radial distance given by r. Maps in the left column are centered at 0°; right column at 180°. The total line of sight column density increases as the emission source moves to larger radii, enclosing more clouds.

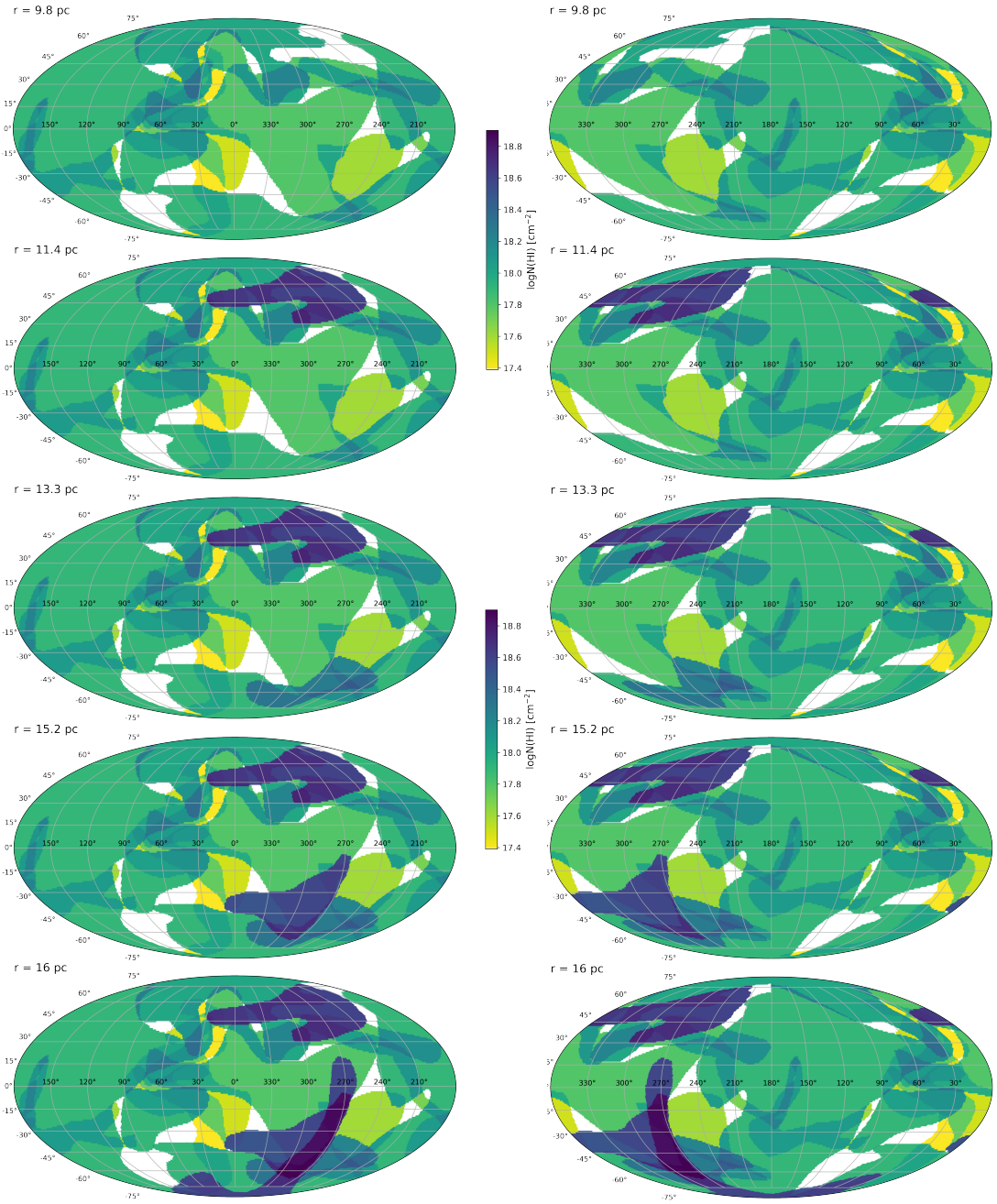

(b) Radius of screen of emission at $r = 9.8, 11.4, 13.3, 15.2, 16$ pc.

Figure 4.3: These plots show the total column density of LISM clouds encountered by an isotropic spherical shell emission source at a radial distance given by r. Maps in the left column are centered at 0°; right column at 180°. The total line of sight column density increases as the emission source moves to larger radii, enclosing more clouds.

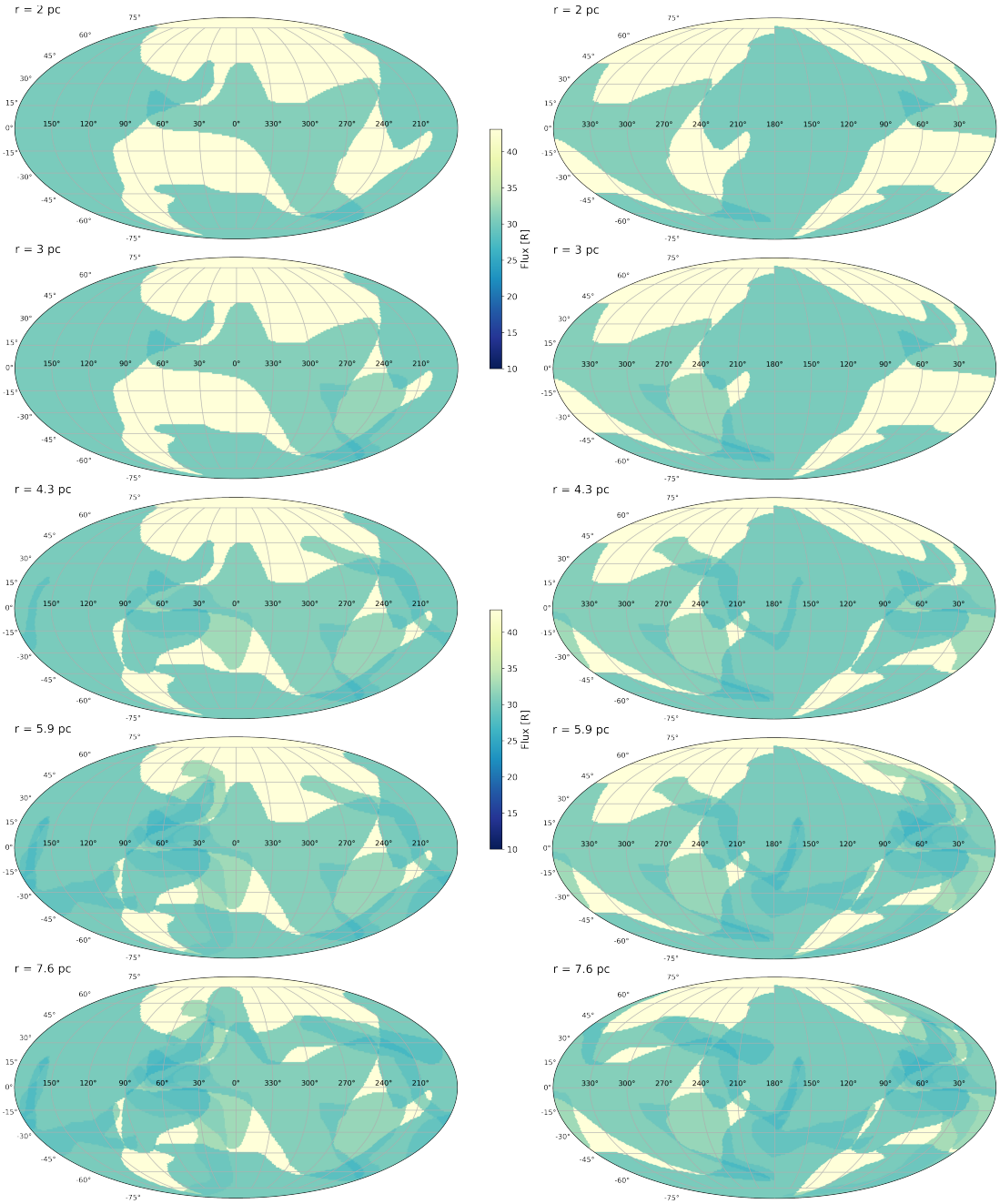

(a) Radius of screen of emission at $r = 2, 3, 4.3, 5.9, 7.6$ pc.

Figure 4.4: Model 2. These plots show the Lyα flux escaping the LISM cloudscape due to a 43 R isotropic spherical shell emission source at a radial distance given by r. Maps in the left column are centered at 0°; right column at 180°. The number of clouds included in each line of sight increases as the emission source moves to larger radii, leading to greater attenuation of the source emission.

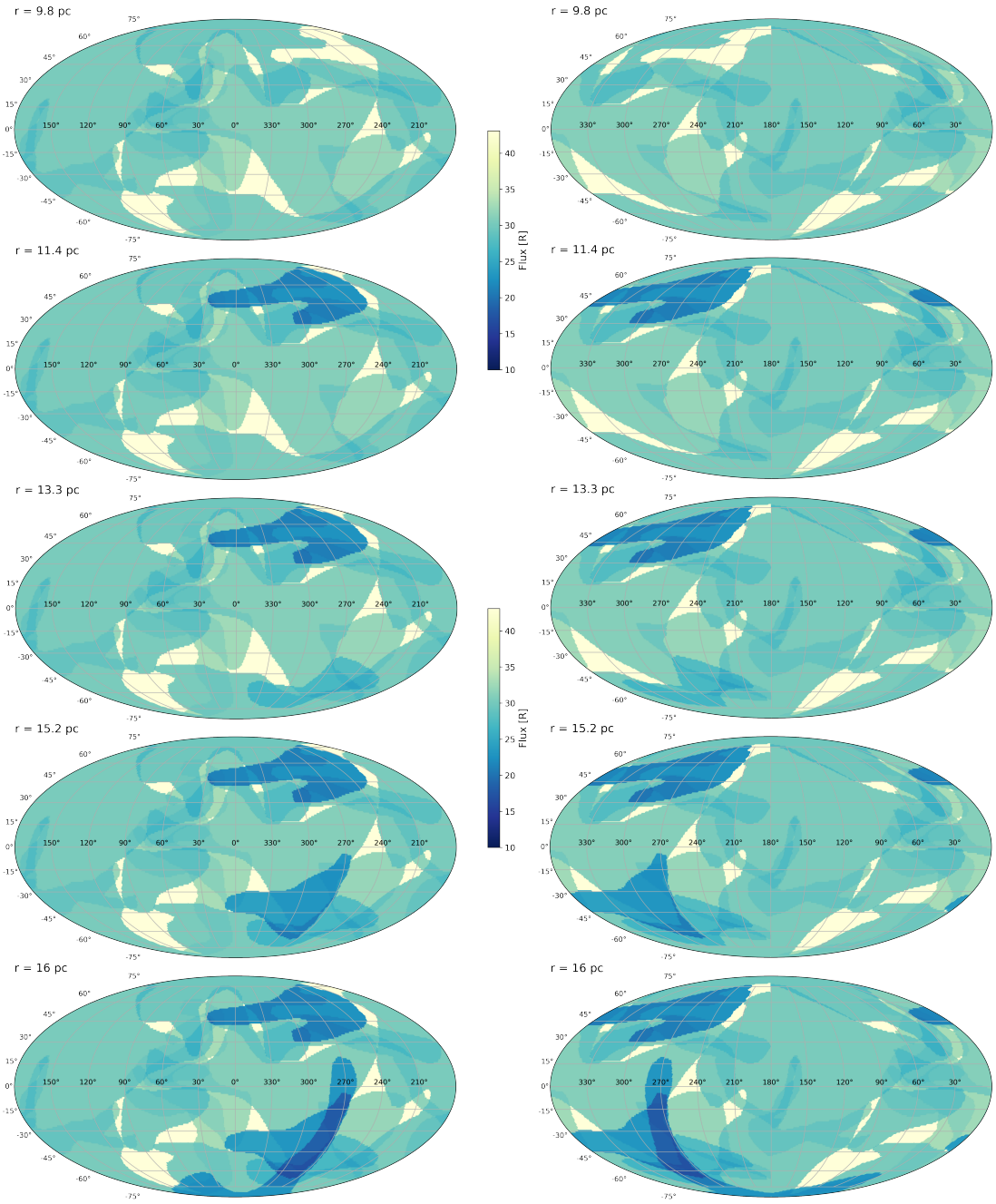

(b) Radius of screen of emission at $r = 9.8, 11.4, 13.3, 15.2, 16$ pc.

Figure 4.4: Model 2. These plots show the Lyα flux escaping the LISM cloudscape due to a 43 R isotropic spherical shell emission source at a radial distance given by r. Maps in the left column are centered at 0°; right column at 180°. The number of clouds included in each line of sight increases as the emission source moves to larger radii, leading to greater attenuation of the source emission.

Cloud. Because the Sun is understood to lie somewhere on the edge of the LIC, or within the LIC/G interface, we wanted to include at least these two clouds. As r increases, more clouds are included, and as expected, greater absorption occurs. We placed emission screens equidistant between adjacent clouds, at $r = 2$, 3, 4.3, 5.9, 7.6, 9.8, 11.4, 13.3, 15.2, 16 pc. At $r = 16$, finally all LISM clouds lie within the sphere, and we witness the most extreme absorption, and only small slivers of the sky are free from any cloud cover.

Shortcomings of **Model 2**: Lacking information about the density and thickness of the LISM clouds, we model clouds as if they are 2D slabs located at the position of the closest star showing absorption from them. But actual ISM clouds have depth in the radial direction and may extend in front of and behind the star in question. Were the true thickness of the clouds known, it is possible that some would extend across the spherical emission shells of our models, resulting in more/less absorption than depicted in these models.

4.2 Anisotropic Emission

These simple models of isotropic Lyα emission have given us a sense of the effect of LISM absorption on a level playing field; but to actually recreate *NH*'s Lyα observations, we need to consider a plurality of realistic emission sources. We were motivated to investigate the possibility of anisotropic emission due to observational evidence of collisional processes occurring between LISM clouds that could lead to the production of very local, direction-dependent Lyα photons from within the cloudscape (Redfield & Linsky 2008; Linsky et al. 2008; Swaczyna et al. 2022).

In comprehensive surveys of the sky, the LIC and G Cloud are found to domi-

nate, often the only cloud present on a given sight line (Redfield & Linsky 2008). But at the boundary of LIC and G, many overlapping clouds appear packed together. These may be regions where collisions between the LIC and G Cloud are generating new clouds with different motion. The Mic Cloud – a filimentary cloud wedged between the LIC and G – has the highest temperature and one of highest turbulences of all the LISM clouds, supporting the hypothesis that it is a shock from a LIC-G collision. Average turbulent velocities within a cloud are too low to cause shocks, but macroscopic velocity differences between clouds can be much greater than the speed of sound and result in shocks. The LIC-G interface has been called the "Ring of Fire," like that in the Pacific Ocean where tectonic plates collide (Redfield & Linsky 2008). Such collisions of LISM clouds could produce heating, turbulent flow, or shocks that generate two-photon emission, and may be the explanation for the observations of scintillation in radio sources whose lines of sight traverse interaction zones in the LISM cloudscape.

4.2.1 Radio Scintillation Sources

Strong evidence that LISM clouds are colliding has been provided by observing the scintillation of distant quasars emitting in radio wavelengths (Linsky et al. 2008). It was unexpected for there to be screens of material in the ISM that would cause scintillation like that which the Earth's atmosphere causes for all non-solar system objects. But the radio flux of very distant galaxies with bright active nuclei (quasars) have been observed to fluctuate $1 - 10\%$ on timescales of less than a day (called intraday variability, or IDV) because their light is passing through a turbulent region of the ionized, warm ISM of the Milky Way. Turbulence creates sub-regions of higher and lower electron density, resulting in different refractive

indices that bend the passing light and cause it to twinkle. These regions of turbulence are called interstellar scintillation screens (ISS). On rare occasions, a few quasars have been observed that even vary on the scale of an hour (intrahour variability, or IHV), which means their light must be passing through significantly denser regions, such as a turbulent cloud.

Redfield & Linsky (2008) identified 3D velocity vectors for 15 LISM clouds within 15 pc of the Sun. The cloud boundaries were drawn to enclose regions where gas velocity vectors were largely parallel, suggesting a common bulk motion. But the velocities between the clouds themselves vary vastly (0 - 50 km s^{-1}) relative to the local standard of rest (Fig. 4.5), which indicates the clouds will likely collide with each other, which will in turn shape the physical properties and dynamics of the LISM. Collisions cause shearing which is known to generate turbulence.

In a relevant study, Linsky et al. (2008) studied three quasars (PKS B1257-326, QSO B1519-273, and QSO J1819+385) that exhibited IDV of the largest known amplitude with the highest quality data sets available and fit the ISS timescale observations. These sources lie behind regions where the warm, partially ionized LISM clouds identified by Redfield & Linsky (2008) may be colliding, and this interaction of clouds with very different transverse and radial velocities could cause turbulence that would explain the scintillation.

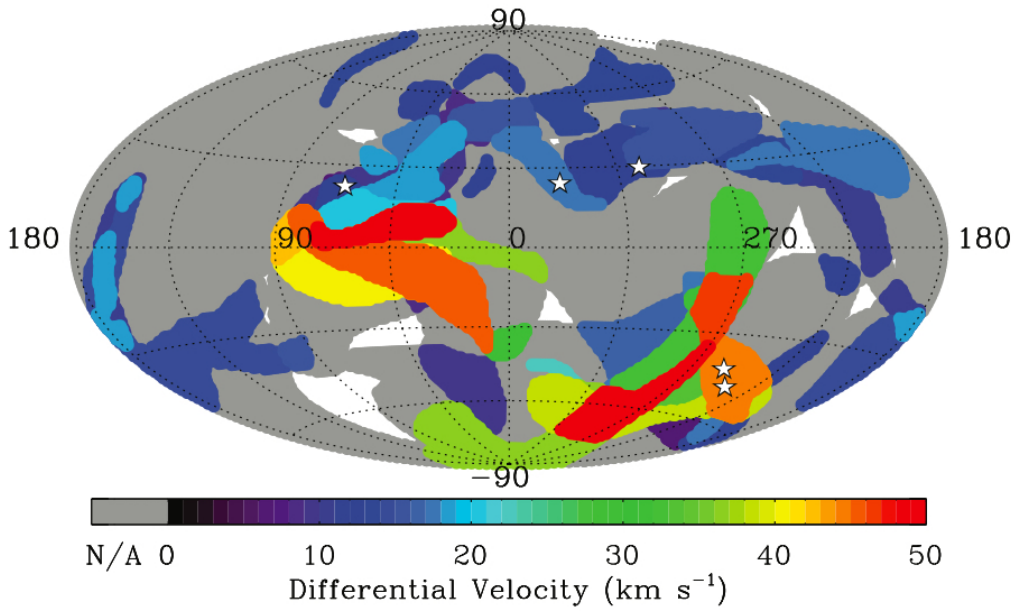

Figure 4.5: Regions of possible interaction between LISM clouds. Colors indicate the maximum differential velocities between LISM clouds on a given line of sight, ranging from 0 - 50 km s^{-1}. There are no clouds detected within the white regions, one cloud within grey regions, and multiple in the colored regions. It is predicted that the colored regions are where large-amplitude IDV radio scintillation sources will be discovered. Star symbols indicate the locations of five known IDV sources. The three sources in the northern hemisphere are PKS B1257-326, QSO B1519-273, and QSO J1819+385 discussed in this section. The two southern hemisphere sources have insufficient data and are not discussed. (Image: Linsky et al. (2008).)

One would expect there to be annual variation in quasar scintillation timescales because the Earth changes velocity relative to the ISM as it orbits the Sun. First, Linsky et al. (2008) considered a wide variety of ISS velocities, and found a narrow range that were compatible with the known annular variation of ISS data. Then the paper compared IHV ISS velocities with those of the warm LISM clouds within the line of sight, predicting that the turbulence may be generated by cloud-cloud interactions at the boundaries of the LISM clouds. The edges of clouds are less shielded than their centers, resulting in higher ionization levels and enhanced electron densities, giving them prime properties to serve as scintillation screens.

They found that each quasar's line of sight crosses at least two LISM clouds

with velocities that match that of the ISS within a chi-squared value of ≤ 1.2 (indicating a good fit), meaning the transverse motion from the scintillation was very close to the transverse motion of the LISM clouds (Linsky et al. 2008). In each case, their analysis suggested that the scattering screen is located at the edge of one of the clouds. Ultimately, distances to the scattering screens are constrained to be < 6.7 pc for B1257-326, < 5.1 pc for J1819+385, and < 3 pc for B1519-273 (Linsky et al. 2008). In the past, it was assumed that the local standard of rest (i.e., the motion of the Sun around the Galaxy) was causing the ISS, but the authors concluded its transverse velocity is not sufficient upon deeper inspection. Overall, the evidence strongly suggests that these radio sources are scintillating due to the turbulent motion of colliding LISM clouds.

B1257-326, J1819+385, and B1519-273 are all situated on lines of sight that pass through 2 - 3 LISM clouds with differential velocities ranging from 10 - 17 km s^{-1}. Figure 4.5 shows that nearly *all* lines of sight passing 2+ clouds have differential velocities greater than 10, which leads us to hypothesize that collision zones may be occurring at nearly *all* cloud boundaries. A larger study sample of quasars exhibiting IDV could help ground this hypothesis, but we are unaware of any such studies at this time.

4.2.2 Two-Photon Production

This led us to consider whether the interaction zones between LISM clouds could provide a local source for anisotropic Lyα radiation. It has been predicted that collisions occurring at the boundaries between LISM clouds could generate shocks that might produce two-photon radiation in the Lyα range (Kulkarni & Shull 2023).

Shock waves are produced when material moves at a velocity higher than the local speed of sound in the surrounding medium. Because the surrounding medium does not have time to dynamically respond, the high velocity material comes to an abrupt halt, converting its kinetic energy into heat. The shock wave compresses and accelerates the media it propagates through. Kulkarni & Shull (2023) show that Lyα and two-photon UV continuum emission is produced by low-velocity shocks of the kind that may be generated at LISM interaction zones. Hydrogen atoms are excited by collisions generated by the passing wave, raising their electrons to high energy levels, and sometimes ionizing them entirely. Excited atoms will return to their ground state by emitting Balmer-series or Lyman-series photons in recombination cascades that end with Lyα ($n = 2$ to $n = 1$). It is also possible they may find themselves in a metastable state. If the metastable $2s$ $^2S_{1/2}$ level is inhabited for a certain period of time (for a ~ 0.12 second timescale), two-photon continuum will be emitted as the electron returns to the ground state. Kulkarni & Shull (2023) calculate the production of Lyα, Hα and two-photon continuum from excited hydrogen atoms, and conclude that two-photon continuum may account for 50% of observed Lyα, but is only useful when observed far from the Galactic plane to avoid ISM dust attenuation, and in conjunction with careful modeling of reflected light.

4.2.3 Varying Location of Emission

In **Model 3**, we include nearby Lyα emission sources localized to potential LISM cloud collision zones (see black outlines in Fig. 4.6) in addition to an isotropic, distant, Galactic background source. We begin with a 43 R isotropic background sphere of emission at 16 pc, then we inject additional Lyα emission

at four regions (A, B, C, D) corresponding to locations of suspected cloud-cloud collisions based on high differential velocities, high column densities, and/or the presence of radio scintillation sources, as reported by Linsky et al. (2008). Although it is apparent that Lyα could be produced due to shocks in these regions, the expected quantity of Lyα emission is unknown. As a starting place, we add 5 R of emission in each region. We generate the emission in region A at a radial distance of 2 pc from the Sun, in region B at 5.1 pc, region C at 3 pc, and region D at 6.7 pc.

In Figure 4.7, I have overlaid the LISM cloudscape map with the five radio scintillation sources listed in Linsky et al. (2008) and outlined the regions where I am placing emission screens. The regions I have selected are very blocky, following grid lines to simplify implementation. These are meant only to serve as examples of the kind of effect that localized emission might have; more physically realistic models will become possible once we have a 3D model of the LISM cloudscape.

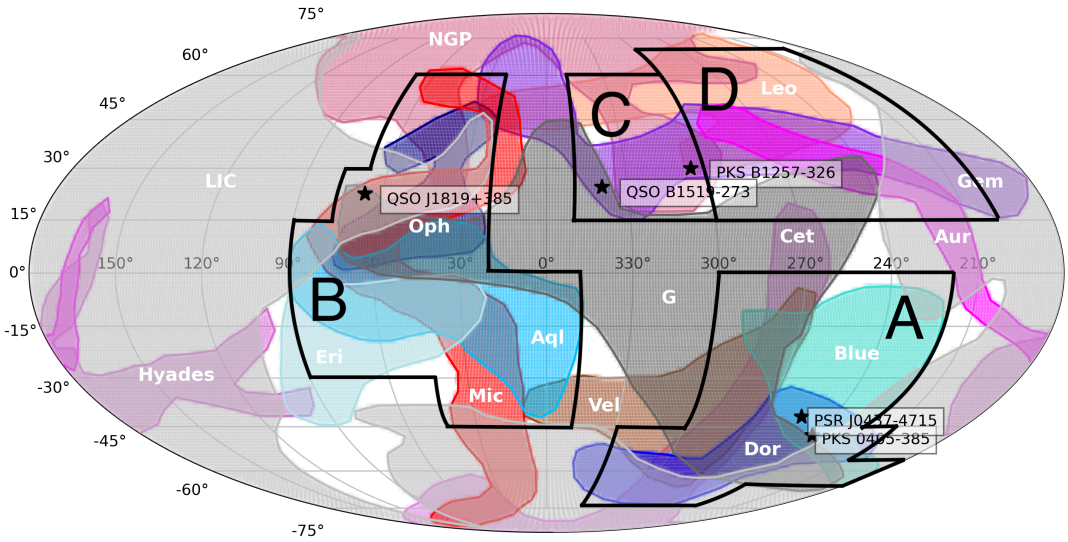

Figure 4.6: Schematic for **Model 3**. 5 radio scintillation sources are labeled by black stars, plotted over a map of the LISM cloudscape. Black boundaries indicate regions (A-D) of possible localized Lyα emission resultant from cloud-cloud collisions and associated shocks.

The criteria for choosing the lines of sight and distances of each region are listed:

- *Region A:* One of the regions of the cloudscape with the highest column densities and the highest velocity differences is the region where Blue, Dor, Cet, Vel, LIC, and G overlap, roughly around $l = 210$ to 200, $b = -15$ to -75. There are two known radio scintillation sources (PSR J0437-4715 and PKS 0405-385) in this region, suggesting turbulence in the LISM (Linsky et al. 2008). Dor, Vel, and Cet are all quite far from the Sun ($r > 11$ pc), making it unlikely they are actively interacting with the clouds closer-in ($r < 3$ pc). They are also some of the densest clouds, casting dark shadows in our models that do not appear in the data. We would expect their dark shadows to be lessened if the closer clouds – Blue, G, LIC – were interacting and generating shock-based emission closer in, in front of those distant shadows. To test this, I place a screen of emission (A) at a distance of 2 pc (between Blue and LIC/G) across the following ranges of longitudes and latitudes to cover this region of possible interaction:

  - $240° < l < 330°$ & $-75° < b < -45°$
  - $180° < l < 240°$ & $-65° < b < -55°$
  - $210° < l < 240°$ & $-55° < b < -45°$
  - $220° < l < 300°$ & $-45° < b < 0°$

- *Region B:* Another place with exceedingly high velocity differences is the region where LIC, G, Oph, Eri, Mic, and Aql overlap, roughly centered on $l = 50$, $b = 15$. A radio scintillation source has been found in this region, QSO J1819+385, which Linsky et al. (2008) estimate is caused by a turbulent

scintillation screen around 5.1 pc from the Sun. That places the screen at the interface of Oph and Mic, two warmer, low-density clouds that Linsky et al. (2008) posits are likely being stirred up by the collision of LIC and G. Eri and Aql also fall on this line of sight in between LIC/G and Mic/Oph. Many signs point to this being a region of turbulence generated by colliding clouds, which would make it a prime location for the production of shock-induced Lyα emission. To test this, I place a screen of emission (B) at a distance of 5.1 pc (just outside Oph and Mic) across the following range of longitudes and latitudes:

- ▷ $350^\circ < l < 360^\circ$ & $-45^\circ < b < 0^\circ$
- ▷ $0^\circ < l < 40^\circ$ & $-45^\circ < b < 0^\circ$
- ▷ $40^\circ < l < 90^\circ$ & $-30^\circ < b < 15^\circ$
- ▷ $20^\circ < l < 40^\circ$ & $0^\circ < b < 60^\circ$
- ▷ $40^\circ < l < 75^\circ$ & $15^\circ < b < 30^\circ$
- ▷ $40^\circ < l < 65^\circ$ & $30^\circ < b < 60^\circ$

- *Regions C & D:* A third place of interest is the region where Aur, Gem, Leo, and NGP overlap. Although not a region of particularly high velocity differences, it does have high column densities (thanks to Leo), and hosts two radio scintillation sources (QSO B1519-273 and PKS B1257-326) which are thought to be the result of turbulent scintillation screens around 3 pc and 6.1 pc respectively (Linsky et al. 2008). To test this, I add two more screens of emission: (C) at a distance of 3 pc, and (D) at a distance of 6.7 pc (between Gem and NGP) across the following ranges of longitudes and latitudes.

- ▷ (C) at 3 pc: $300° < l < 350°$ & $15° < b < 60°$
- ▷ (D) at 6.7 pc: $200° < l < 300°$ & $15° < b < 70°$

Results are shown in Figure 4.7. Focusing on regions A and B, whereas **Model 1** showed highest extinction in these regions due to high column density, **Model 3** replenishes some of that extinction with emission, leading to a more smooth spatial distribution of flux and less harsh boundaries at the edges of clouds.

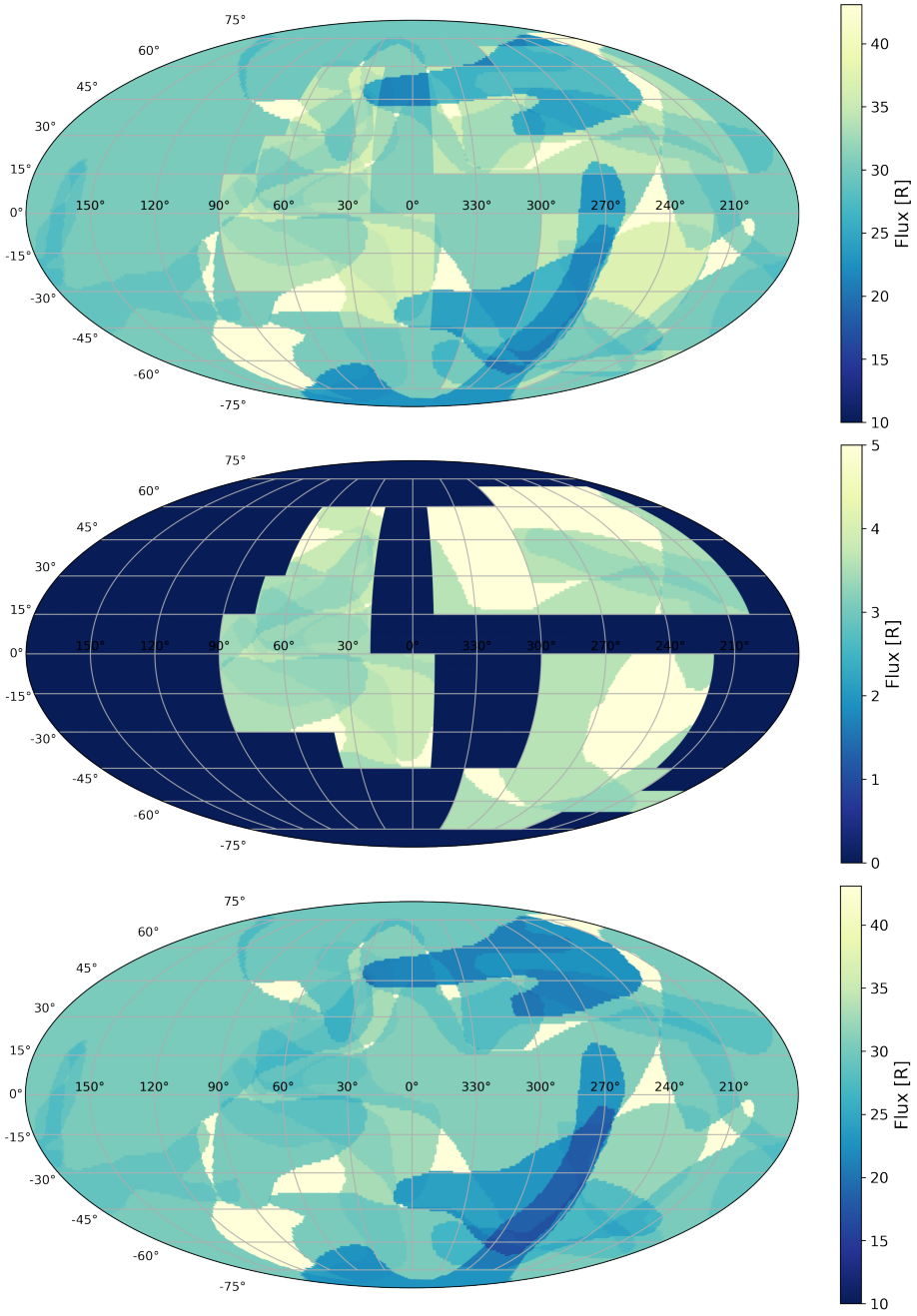

Figure 4.7: Model 3. Results of applying our absorption-only radiative transfer model to a background Galactic Lyα flux of 43 R incident upon the LISM cloudscape from just exterior to the cloudscape, plus localized emission of 5 R in regions A, B, C, and D at radii of 2 pc, 5.1 pc, 3 pc, and 6.7 pc respectively. The upper map is **Model 3**, showing a combination of the middle map (localized emission) and the lower map (isotropic background emission reproduced from **Model 1** in Figure 4.1 for reference).

4.3 Multiple Scattering

Models 1-3 take into account the removal of photons from the line of sight due to absorption or scattering. They do not, however, consider photons that may be scattered *into* the line of sight from off-axis angles. To explore the more realistic scenario of multiple scattering occurring within the clouds, we share some basic experiments using the MCMC code `tlac`.

Geometry & Setup

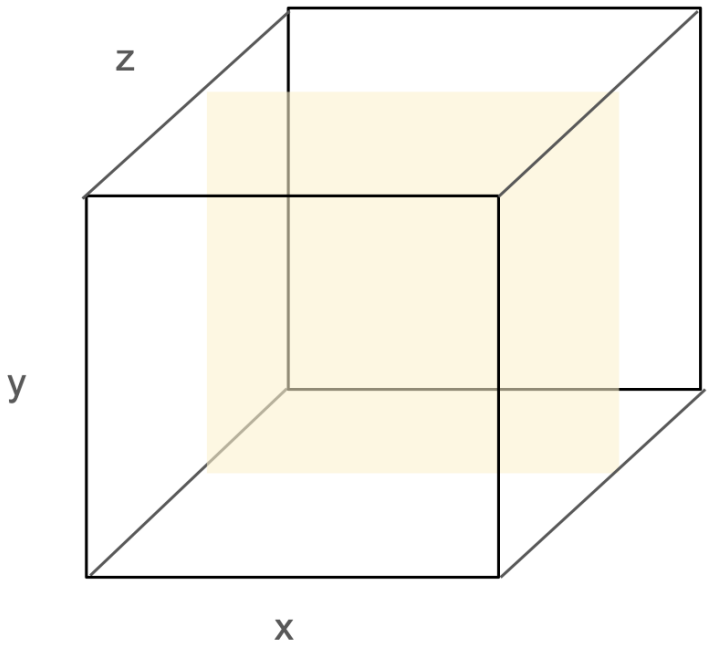

Figure 4.8: Geometry of our `tlac` cube model. The cube has dimensions $30 \times 30 \times 30$ pc, with a plane of Lyα emission located parallel to the XY plane in the center of the box.

The region of space the LISM clouds occupy is generally approximated as a sphere with a radius of 15 pc. We construct a toy model of this space and imagine it is filled entirely with only one medium, as if a single, stationary, homogeneous

cloud extends across the entire region. We then vary the properties of that medium (to match different LISM clouds), and see how the trajectories, destinations, and frequencies of Lyα photons moving through the space are impacted by multiple scattering according to `tlac`. While not a realistic scenario, this is a step towards understanding what to expect should we add multiple scattering into our models.

To accomplish this, we build four 3D cartesian grids (cubes), each $30 \times 30 \times 30$ pc in size, and fill each cube with homogeneous, dust-free, neutral hydrogen with a temperature and column density corresponding to that of the LIC, G, Vel clouds, or the inter-cloud medium (ICM) respectively (see Table 4.1). We choose to focus on LIC and G due to their importance as our closest neighbors, Vel as an example of a high-density LISM cloud, and the ICM as the connective tissue between the clouds. We embed an emission source of 10^7 Lyα photons emitted from a plane parallel to XY in the center of the cube, as pictured in Figure 4.8. The photons are released from the emission plane and then tracked as they travel through the cube until they are either absorbed or escape.

Properties of `tlac` Cube Models

Medium	Temperature [K]	Number Density [cm^{-3}]	Column Density [cm^{-2}]
ICM	10^6	0.005	-
LIC	7.5×10^3	-	10^{18}
G	5.5×10^3	-	$10^{17.8}$
Vel	1.06×10^4	-	$10^{18.5}$

Table 4.1: Properties of gas inside the `tlac` cube models. The temperature of the ICM is given by Frisch et al. (2011), and the number density comes from Streitmatter & Jones (2005). Temperatures and column densities for LIC, G, and Vel are based on average values from Redfield & Linsky (2008).

Number of Scatterings

The number of scatterings n experienced before escape is depicted in Figure 4.9. Most photons escape after just a few scatterings, showing exponential decline towards higher values of n. The number of scatterings for photons in the ICM and G cubes exhibit a steeper decline, and overall, photons in these cubes escape in few scatterings, whereas the LIC and Vel Clouds have more scatterings on average. The total and average number of scatterings is closely tied to the density of material, with LIC and Vel having higher column densities than G and the ICM.

Various analytical and numerical solutions have been posited to estimate the number of scatterings for low opacity and high opacity media (e.g., Osterbrock (1962), Adams (1972)), suggesting photons will escape after τ^2 or τ scatterings, where τ is the material's opacity to Lyα, dependent on the Voigt profile for Lyα and the line of sight column density (see Equation 3.11). However, we are most interested in the end result: where these photons end up and what frequencies they have when they escape. Specifically, will they be in our line of sight, and if so, will they still have frequencies recognizable to our UV detector?

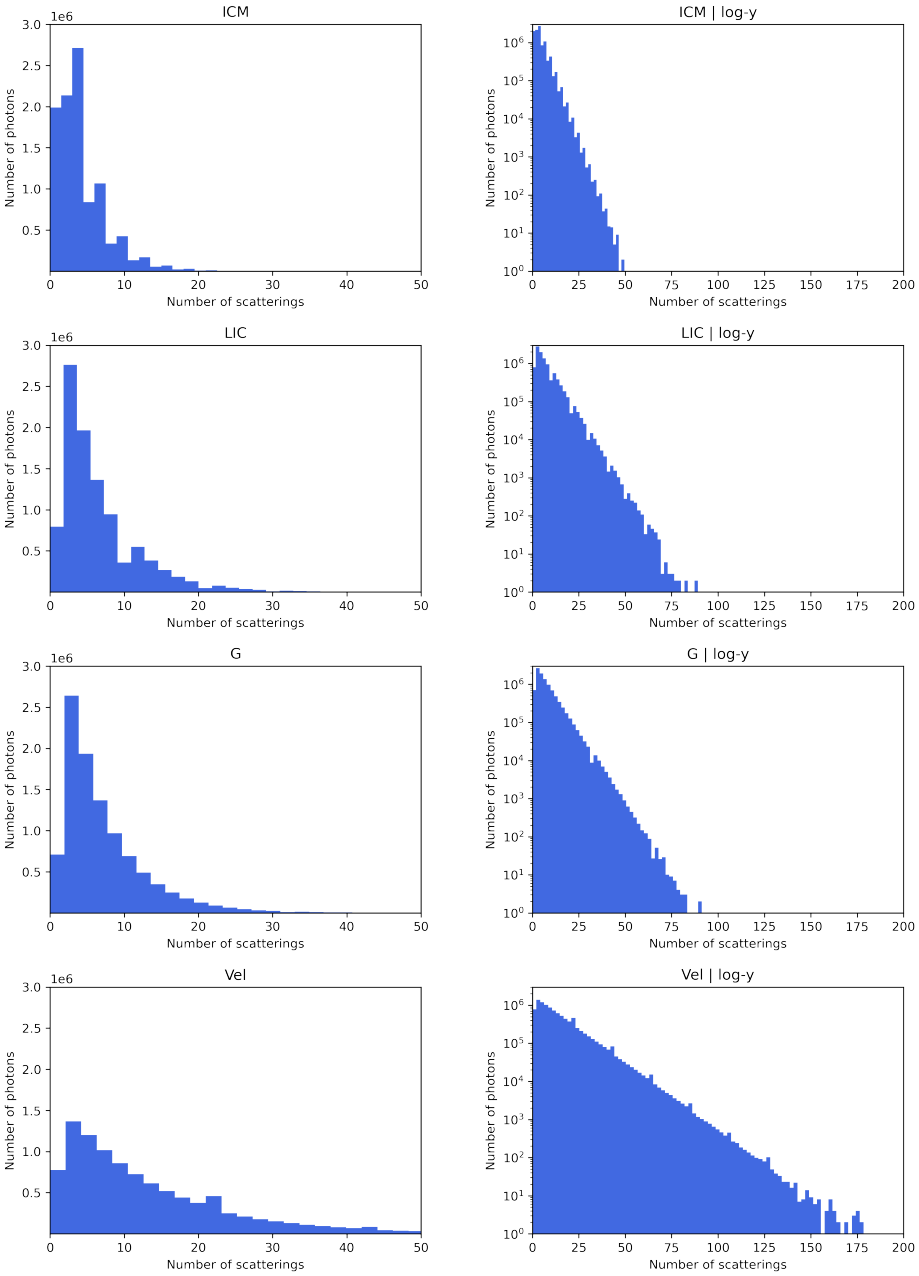

Figure 4.9: Histogram showing distribution of number of scatterings experienced per photon in the `tlac` cube models. The y-axis is linear for the left plots and log for the right plots.

Frequency Distribution

At each scattering, the photon exchanges momentum with the particle, which may result in an exchange of energy. Thus these interactions can change the frequency of the scattered photon. The larger the frequency change, the lower the probability the photon will have to endure another interaction, and the farther it is able to travel (i.e., its mean free path grows). The frequency distributions for escaping photons for each `tlac` cube model are shown in Figure 4.10. The frequency at escape is given in units of $x = (\nu - \nu_0)/\Delta\nu$, which quantifies the offset from the line-center $\nu_0 = 1215.67$ Å (where $x = 0$).

We find the frequencies of the escaping photons are all shifted away from Lyα line center ($x = 0$). Because the path length of Lyα is so short within a hydrogen cloud, the only photons that successfully escape in physical space are those that have also been shifted in frequency-space. At low opacities, all photons of the central frequency ($x = 0$) have been blocked by the medium, but photons that are shifted slightly off resonance ($x > 0$ or $x < 0$) can escape, so you see big lobes just to the right and left of line center. Their frequencies are symmetric about line center because the gas in the cubes did not have a velocity relative to the photon, so their rest frames were the same. These shifted frequencies still fall well within the generous (520 - 1860 Å) passband of Alice and would still be visible as Lyα photons.

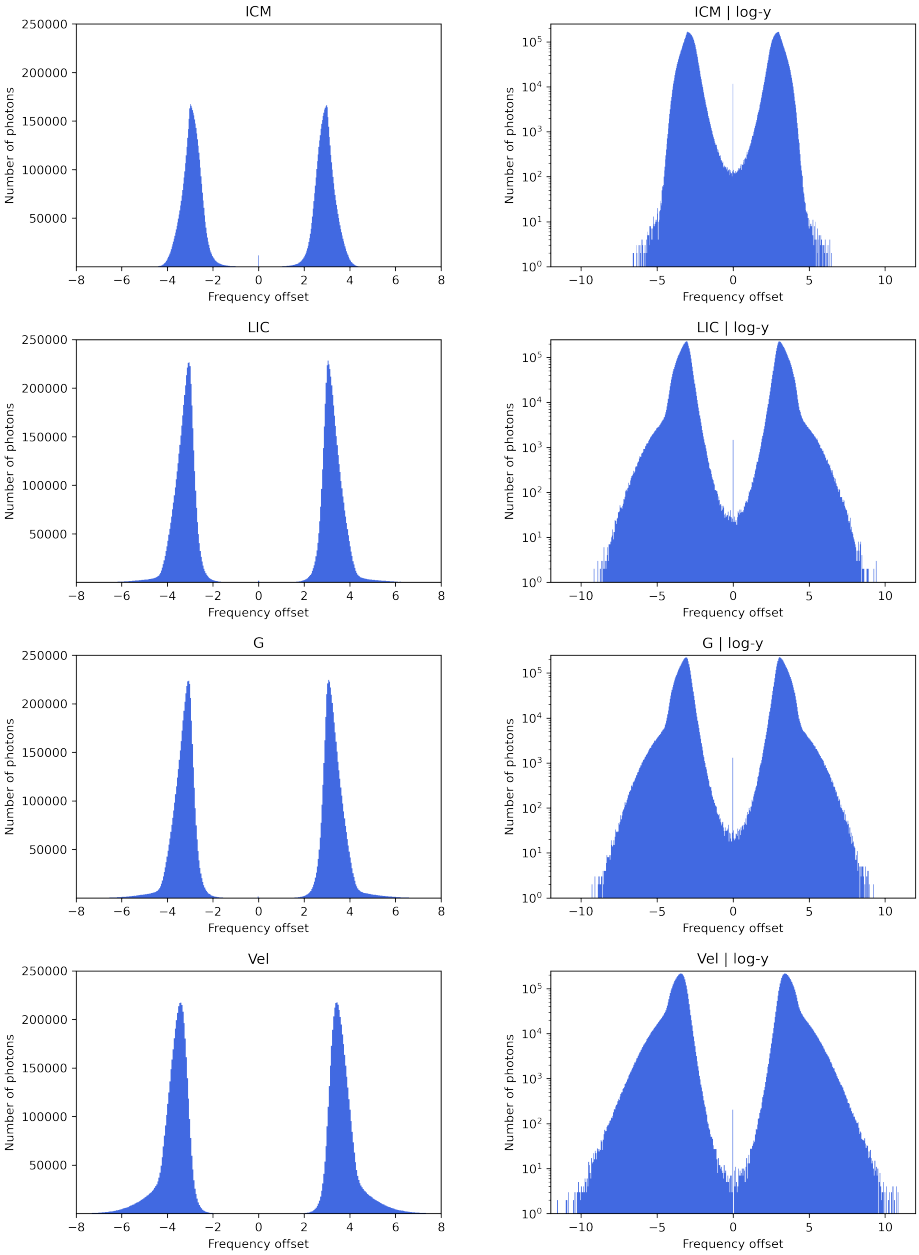

Figure 4.10: Frequency of photons at the moment of last scattering for `tlac` cube models. The x-axis zero-point is the frequency of line center for Lyα (1215.67 Å), with units of $x = (\nu - \nu_0)/\Delta\nu$. The y-axis records the number of photons at that final frequency, and is linear in the left plots and log in the right plots.

Position

For photons that escape the cube, the location of their last scattering is recorded and plotted in Figure 4.11. The *last scattering* is the final interaction a photon has before exiting the box, and thus determines its final frequency and 3D velocity vector. As we look at different faces of the box, we see that face-on to the plane of emission, photons escape roughly randomly and fill the entire XY plane, just like how they were emitted. We notice a slightly higher proportion of them are concentrated towards the edges of the box than the center (by less than an order of magnitude), especially noticeable for the densest cloud, Vel. This can be explained because photons near the edge of the box have a shorter distance to travel to escape the box, are thus are more likely to escape on average. When viewed from the side (ZX and ZY planes), the escaping photons are highly concentrated at the central plane where they were emitted, and exponentially drop off to the edges. This indicates that most photons take their final leap from the cube while still relatively close to their location of emission, which is supported by Figure 4.9 which shows that most photons escape after only a few scatterings.

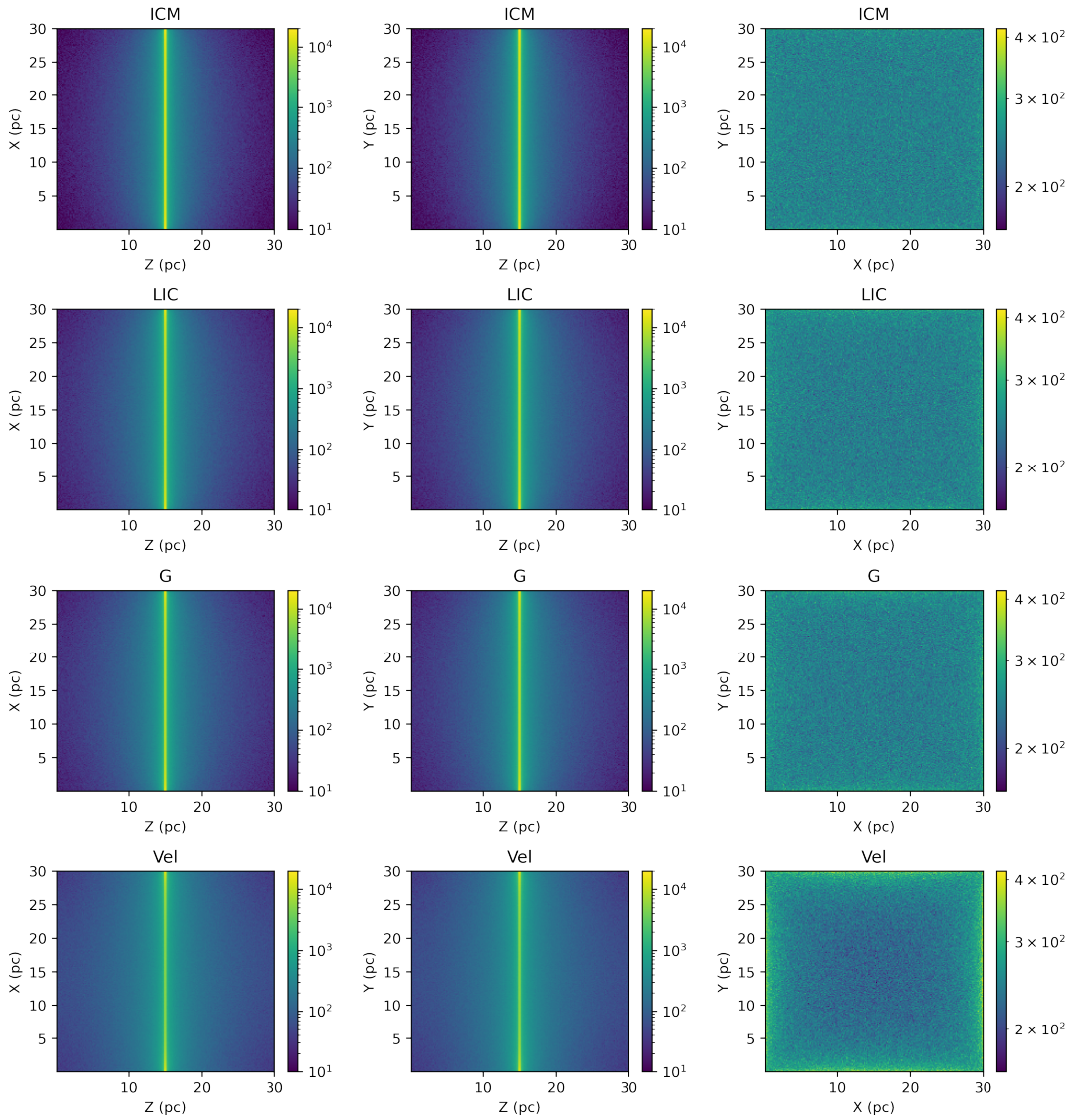

Figure 4.11: Position of photons' last scattering for `tlac` cube models. The location of each photon at the moment it is last scattered is recorded. The photon then escapes the box and continues unchanged on its final 3D velocity vector. The colorbars depict photon count.

Takeaways

Overall, our takeaways from the `tlac` cube models are:

- The number of scatterings a photon experiences before escaping a medium

grows in tandem with the density of the medium. Regardless of density, the distribution decays exponentially for higher numbers of scatterings, such that most photons escape within only a few scatterings.

- Higher column densities will scatter more photons further from line center, but even for the highest column densities present in the LISM cloudscape ($10^{18.6}$ $N(\mathrm{H\,I})$ cm^{-2}), escaping Lyα photons still remain within the passband of *NH*.

- Lyα photons emerging isotropically from a sheet of emission will scatter randomly within a medium, maintaining their isotropy. However, we do not know how they behave at boundaries between bodies with different properties (such as the edges of clouds), which may break the isotropy.

Chapter 5

Results

We find that LISM absorption of an isotropic background Lyα emission alone does not fully explain the residuals in *NH*'s all-sky Alice observations, and further mechanisms (e.g., multiple scattering, localized emission) are important and must be incorporated.

5.1 Comparing Models & Observations

In Figure 5.1, we take a closer look at the residuals of the Alice data (after subtraction of the scattered solar model) in comparison with a modified version of **Model 1**. The background emission in this model has been raised arbitrarily to 60 R to better reproduce the brightness measurements from Alice in the polar regions.

Shadows

In this model (Fig. 5.1b), we see regions of high absorption, but they are localized on the right side, whereas most of the rest of the sky has a relatively more uniform brightness. The densest clouds (Cet, Vel, Leo) with column densities above $10^{18.5}$ $N(\mathrm{H\,I})$ cm^{-2} have the largest impact on absorption, appearing as the darkest blue regions.

The Alice all-sky observations are still being processed by the *New Horizons*

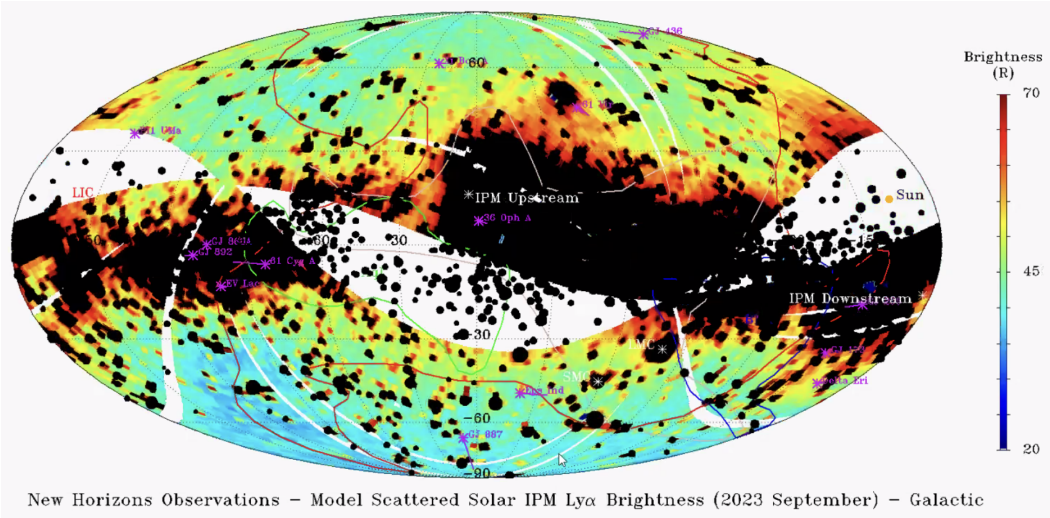

(a) Residual Lyα brightness as observed by *New Horizons'* Alice UV Spectrograph after subtraction of a scattered solar model and the deletion of known UV-bright stars (black dots). Data was not taken for the 30° swath that passes through the Sun (indicated by an orange dot). (Image: G. Randall Gladstone.)

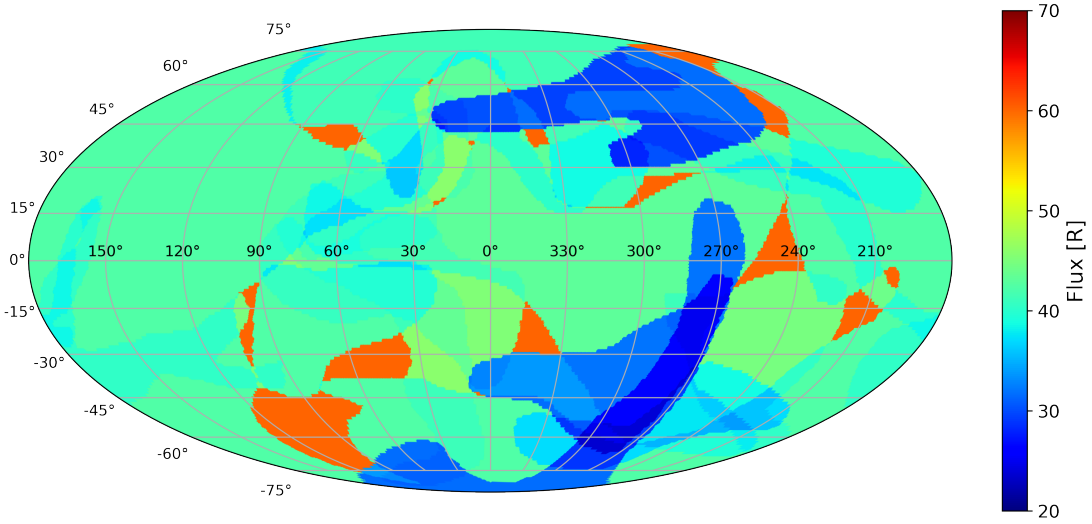

(b) Modified **Model 1** map of Lyα emission from a 60 R isotropic Galactic background source after transmission through the LISM cloudscape. The colorbar has been scaled to match plot (a).

Figure 5.1: Comparison of **Model 1** with the residuals from *NH*'s Alice all-sky Lyα observation. In both maps, data is displayed in Mollweide projection using galactic coordinates.

Science Team, but it is already apparent in Figure 5.1a that there is a marked difference in average brightness between the northern and southern polar regions, with $\sim$ 40 R in the north and $\sim$ 30 R in the south (Gladstone 2024). In this model, the presence of Cet covering the south pole brings the brightness of the south pole down to $\sim$ 30 R, while the lack of dense clouds at the north pole gives the north pole a higher brightness of $\sim$ 40 R. This seems initially promising; however, when flux values are averaged across the polar region as a whole (i.e., all latitudes above 60° for the north polar region, all latitudes below 60° for the south), we get values that are nearly the same across both poles: $\langle F_{\text{north}} \rangle = 40.5$ R and $\langle F_{\text{south}} \rangle = 42.5$ R.

Additionally, the presence of a dark patch due to Leo at northern latitudes is not seen in the data.

Highlights

On the other end of the brightness scale, especially bright patches (seen in orange in the model) peek out from between clouds in the model, and these bright spots are not present in the data. Particularly notable is the large bright orange patch around $(l, b) = (100, -50)$, which paradoxically corresponds to the lowest brightness region in the data. A possible explanation for these bright spots could be that the modeled background Galactic emission level of 60 R is too high and should be lowered back down closer to the literature value of 43 R. However, this would also lower the brightness of the rest of the map, bringing the median bulk flux down into the 20s of R across the map, much lower than is seen in the data. Another explanation could be the presence of unknown absorbers or scattering mechanisms in these peek-a-boo regions between clouds, diffusing and extinguishing some of the light. In our `tlac` experiments (Fig. 4.11) we saw that

the hot inter-cloud medium was just as effective at scattering photons as the G Cloud, so perhaps the distinction between cloud and non-cloud in the LISM is not as significant as we had thought. A more realistic model would incorporate the ICM to account for absorption and scattering occurring between clouds.

Sharp Edges

Another feature of our model is sharp boundaries at the edges of clouds, which are not readily seen in the data. We expect that if we were to introduce multiple scattering into the model, these hard edges might get blurred out to some degree.

5.1.1 Discussion

Our absorption-only line of sight models indicate that if we assume Galactic emission in Lyα is isotropic, then the transmitted Lyα necessarily becomes *an*isotropic due to the intense and direction-dependent absorption that occurs as it passes through the clumpy LISM cloudscape.

Here we revisit the question of whether isotropic Galactic emission is a reasonable assumption. Since Lyα is readily produced in stars, we might expect instead that the Galactic plane should glow brightly in Lyα, creating a wall of light where stars are packed tightly together, and fading out according to some scale height as sight lines move towards the poles. Indeed, the mid-plane of the Alice all-sky observation (Fig. 5.1a) is significantly brighter than the poles, even after black dots are placed over known stars. This ambient Lyα glow across the mid-plane cannot be attributed solely to individual stellar point-sources, and instead suggests phenomena that allow light to spread out.

Stellar point sources of Lyα could spread out moderately if those stars were

embedded in molecular clouds or stellar nurseries where photoionization and recombination cascades are occurring. The closest stellar nurseries are $\sim$ 130 pc from Earth (e.g., the Corona Australis Molecular Cloud, the Rho Ophiuchi Cloud, etc.). It is possible that these distances are be too vast for Lyα photons to survive all the way to us, and these sources take up relatively small angular areas on the sky, but they could be contributing something to the overall mid-planar glow.

Another source of midplanar glow could be Lyα emitted by distant stars that subsequently gets scattered and spread out as it travels though the distant ISM, although the degree to which we could expect these photons to spread out spatially in uncertain. Additionally, the pathlength of Lyα is quite short, and it may be unlikely that we are receiving Lyα photons from any but the closest stars.

The question of *where* exactly all this background Galactic Lyα originates is a longer question for another thesis. What we can say for the sake of this project is that Lyα does arrive from the Galaxy, and it likely has some kind of anisotropic spatial distribution. But if the Galactic Lyα background is anisotropic, why do Alice observations of the polar regions appear so smooth?

Perhaps it is most realistic to say that Galactic Lyα emission is highly anisotropic – originating from a combination of stellar and gaseous sources, in the Galactic plane and scattered across the sky – but is smoothed into near isotropy due to scattering and two-photon-production during its passage through the LISM. We expect multiple scattering to have the effect of smoothing out harsh boundaries by scattering photons into our line of sight at unexpected angles which, when traced back by the eye, may appear to have originated from within regions that should otherwise have been dark. While absorption-only models suggest that the sight lines that pass through the highest number of clouds should transmit the least amount of light, our models that incorporate two-photon production at

cloud-cloud interaction zones suggest the contrary, that these dense regions may actually be producing their own light, balancing out the absorption.

At the outset, we naively hoped that isotropic Lyα emission from the Galaxy might be filtering through the LISM cloudscape, and would reveal to us a distinct pattern corresponding to cloud boundaries, allowing us to map the LISM cloudscape in a new way. But no clear cloud boundaries have revealed themselves in the data thus far. We might turn our assumption on its head, and hypothesize anew that anisotropic flux from the Galaxy is being smoothed out by LISM cloud absorption, cloud-induced scattering, and inter-cloud photon production. In a roundabout way, the apparent invisibility of LISM cloud boundaries and the overall unexpectedly smooth appearance of Galactic Lyα might actually be confirmation that clouds are there in the first place.

Chapter 6

Conclusion

We set out to investigate whether *New Horizons* has finally put enough distance between itself and the Sun to have become sensitive to structures outside the Solar System, specifically nearby clouds in the local interstellar medium, seen as shadows cast against the background glow of the Milky Way. To answer this question, we modeled the radiative transfer of Lyα photons through the LISM cloudscape to see the imprint they might leave on the Galactic background emission. Our key findings are:

- Absorption-only line of sight radiative transfer models of Lyα traveling through the LISM cloudscape result in large (10-30 R) jumps/drops in flux at the edges of clouds, particularly around clouds with high column densities such as Leo, Vel, Cet, and Dor.

- These hard jumps are not seen in the latest Alice all-sky observations from *New Horizons*. The observed Lyα brightness (outside the Galactic midplane) is remarkably smooth, although not completely smooth, with a mottled appearance that varies locally on scales of $\sim$ 5 R. On average, the northern polar region appears $\sim$ 10 R brighter than the southern.

- Incorporating multiple scattering into future radiative transfer models could smooth out some of the harsh boundaries of earlier models.

- Localized Lyα emission could be occurring within the LISM cloudscape due to shocks at cloud-cloud collision zones. Incorporating Lyα emission at these zones in future models could additionally balance out the harsh drops in flux around the denser clouds.

- The small variations in the observed Lyα brightness at high/low latitudes could be due either to LISM clouds mottling an isotropic Galactic Lyα background flux, or LISM clouds smoothing out an anisotropic Galactic Lyα background. Further explorations into the likely sources and spatial distribution of the Galactic Lyα background would be fruitful.

6.1 Future Work

The models presented in this thesis are preliminary, and we look forward to refining and expanding upon them in the future. Our next goals are to:

- estimate densities for the LISM clouds to get us closer to a 3D model;

- create a fully 3D LISM cloudscape model in `tlac` and perform radiative transfer calculations that incorporate multiple scattering;

- consider other possible inputs to the apparent background Lyα flux, such as scattering off the Hydrogen Wall;

- subtract our models from the Alice data and quantitatively assess the goodness of fit of each model, giving us feedback with which to iterate on different parameters (e.g., adding more emission here or there);

- and finally, assess the optimal distance from Earth at which *NH* may become sensitive to observing structures in the LISM.

6.1.1 Estimating Density

Preliminary analysis of the Alice all-sky Lyα observations reveals an average difference in brightness between the northern and southern polar regions of ~ 10 R (Gladstone 2024). To explore this difference more, we would like to convert our LISM cloud column density measurements into actual density values. We can do so by assuming LISM clouds fill $5.5 - 19\%$ of the local interstellar volume, as per current volume filling factor estimates in the literature (Redfield & Linsky 2008), allowing us to estimate whether one pole has a higher average hydrogen density.

6.1.2 Multiple Scattering

Incorporating multiple scattering into our models could smooth out the harsh boundaries seen at the edges of LISM clouds by introducing off-axis photons scattered into the line of sight in the densest regions. We are exploring the possibility of using `tlac` to construct a 3D model of the entire LISM cloudscape. We would need to build a 3D grid on the scale of the local interstellar region, and fill individual grid cubes with relevant temperatures, dust opacities, and neutral hydrogen densities according to the positions of LISM clouds, while filling the remaining space with the properties of the ICM. We would then define a spherical shell of Lyα emission with a radius of 16 pc that lies exterior to the cloudscape as in **Model 1**, and possibly specify smaller regions of emission localized to cloud-cloud interaction zones as in **Model 3**. `tlac` would follow each photon on its path through the cloudscape, accounting for absorption and multiple scattering. If we place an observer at the center of the cloudscape, we could capture the distribution of surviving photons falling on that observer from each line of sight. We would ideally run this 3D grid through `tlac` repeatedly, iterating on the magnitude and

locations of incident Lyα emission as we seek explanations for the trends seen in the Alice observations. We are currently exploring whether `tlac` is configurable for this specific geometry.

6.1.3 Hydrogen Wall

As discussed previously in Section 2.4.4, the Lyα brightness observed by Alice could be originating from many sources, including solar Lyα scattering off the interplanetary medium, Lyα of Galactic origin, Lyα created by collisions and shocks within the LISM cloudscape, or solar Lyα scattering off the Hydrogen Wall in the outer helisophere. The scattered solar model from Pryor et al. (2024) tries to account for the first, our models seek to tackle the second and third, but we have not yet engaged with the fourth. Estimates suggest that Hydrogen Wall scattering could appear in Alice's Lyα measurements, contributing at most 10 - 20 R to the overall Lyα background (Gladstone 2024). We would like to look into the Hydrogen Wall scattering models of Baliukin et al. (2022) to see if combining them with our LISM Lyα absorption/scattering models might together do a better job at accounting for the Alice all-sky residuals.

6.1.4 Subtracting Models from the Data

Once fully processed data from Alice's all-sky observations are complete, we plan to subtract our models from the data and run χ^2 tests to determine the best fit. This will give us a quantitative metric to assess the goodness of fit of our various models.

6.1.5 Detectibility Threshold

We would like to do more thinking about the threshold of detectibility for Lyα background structure due to LISM clouds. If it is true that the LISM cloudscape is casting shadows on the Lyα emission reaching our solar system, on what level are those shadows visible, and how strong would the Galactic Lyα signal need to be for them to be detectable? In the models presented in this thesis – assuming a 43 R background flux from the Galaxy – the Lyα emission escaping the LISM cloudscape exhibits a mottled appearance with differences occurring on levels of $\sim$ 10 - 20 R. The scattered solar model that gets subtracted from Alice Lyα observations is only considered accurate down to 10 - 20 R, and consequently, we could expect variations due to LISM clouds to be comparable to noise. However, the most distinctive feature of the scattered solar model is its smoothness, so even if the overall flux value is wrong, anything varying from perfectly smooth must be due to something other than scattered solar light.

Currently 50% of Lyα received by *NH* is attributable to scattered solar emission, with the remaining 50% attributed to background sources. As *NH* travels further from the Sun, the scattered solar emission will decline in brightness as $1/r$, and the background Lyα will appear brighter in comparison. It would be interesting to extrapolate out into the future to see how far *NH* must travel for background Lyα to become 60, 70, or 80% of the received signal, and at what threshold the imprint of the LISM would become visible above the noise.

6.2 Implications

All-sky observations are costly in terms of fuel and human-hours spent planning and executing complex spacecraft maneuvers. Our work provides the first

step towards determining whether *New Horizons* is currently sensitive to ISM structures beyond the heliosphere, and will help the Science Team determine future priorities for the mission, including if/when it may be reasonable to perform subsequent all-sky observations. Our work also has the potential to provide observational evidence for the hypothesis that cloud-cloud collisions may be generating emission from within the LISM cloudscape. In future iterations, we hope to get closer to a model of background Lyα emission and its engagement with the LISM that can reproduce the data from Alice. For the field at large, this project represents a new method of studying the local ISM, improving our knowledge of the immediate environs in which our solar system is situated. The model I have begun developing in this thesis will continue to grow in effectiveness in the coming years as *NH* becomes increasingly sensitive to Galactic radiation the further it travels beyond the heliosphere.

6.3 Reflections of a Cloud Chaser

My highest hope when setting out on this journey was to visualize the local interstellar cloudscape – our corner neighborhood of the Milky Way – with the new ultraviolet eyes afforded by *New Horizons*. I hoped that after nearly 20 years of travel, *NH* was finally far enough away from the glare of the Sun that it might see the shadows of the LISM clouds emerge from the fog. What I found instead was that it is not fog that most obscures our view, but rather, the limitations imposed by our own assumptions.

One of the fundamental questions I wrestled with in this thesis was how to capture a cloud and pin it down. In order to perform calculations to estimate how light might interact with the LISM cloudscape, I had to simplify these amorphous,

diaphanous, continuously shifting entities into rigid, stationary slabs with stark boundaries. It is no surprise that the harsh boundaries created by my blocky models did not turn up in the data. In the process of modeling the clouds, I lost their essence and they slipped through my fingers.

At times I felt as frustrated as the singing nuns from the 1959 musical *The Sound of Music* as they struggle to describe the character Maria. They sing, "How do you solve a problem like Maria? / How do you catch a cloud and pin it down? / How do you find a word that means Maria? / ...How do you hold a moonbeam in your hand?" (Rodgers & Hammerstein 1959). A human being – like a cloud, like anything – is continuously in the process of becoming. As you sit here reading, your body is changing on a cellular level and your brain is creating neural pathways that were not there moments ago. Like a cloud that continually recycles its particles with the surrounding air, every cell in my body has been replaced within the past seven years, as have many of my tastes and opinions.

There have been many periods in my life when I have attached myself to an identity, because sometimes defining myself as a woman, or queer, an artist, or a scientist, has been useful to help me find community and belonging. We draw these boundaries from time to time and climb inside, so that we can have some kind of ground from which to speak. While these labels are practical, we risk trapping ourselves in the process. This is not to say we should banish all boundaries, but rather, hold them as we hold any tool – carefully, with purpose. We began this thesis with the aphorism *all models are wrong, some are useful*, and the key is to not mistake the model for more than it is, a useful estimation of something wilier than we will ever grasp. The fact that we will never fully pin down the universe does not make it any less fun to chase.

In an effort to unpack the challenge of pinning down the wily world, I shadowed

a Japanese woodblock printing class with Master Printmaker Keiji Shinohara during the heart of my thesis writing. I wanted to learn from the nearly two millennia of carvers who have perfected the art of crystallizing natural movement into stationary blocks of wood. Intently, I observed their techniques for carving clouds, their approaches to capturing texture, volume, and the interplay between transparency and opacity. In my first cloud carving (Fig. 6.1), I used curved strokes to outline the bulbous shape of a cumulonimbus cloud, varying the frequency of the lines to suggest highlights or regions of shadow. It came out looking like a lumpy, striped potato, unrecognizable even to my instructor.

Figure 6.1: Rewa Clark Bush, *Untitled (Test Print)*, woodblock, 2023.

In my next attempt, I experimented with a technique in which you carve only tiny parallel lines across the entire block, and then go back in, varying the pressure of your tool to increase or decrease the thickness of the line. More pressure leads to deeper grooves, opening more light on the page. Less pressure keeps the cuts shallow, leaving more of the wood's surface intact to receive ink. In this way, you create regions of light and darkness without ever drawing a border. When done this way, sun and shadow blend continually into one another, creating form as optical illusion rather than fact, and you lose the ability to say for sure where one body ends and another begins. In this way, my second cloud carving took shape (Fig. 6.2).

Figure 6.2: Rewa Clark Bush, *Cloudscape (Test Print)*, woodblock, 2023.

Up close, the image is unrecognizable, like the tri-colored dots that comprise a magazine picture, static. The picture changes when viewed from farther away, and billowing, voluminous shapes emerge out of the horizontal lines. By avoiding boundaries altogether, the clouds are allowed to breathe and move, even as they are carved in wood. To my delight, these clouds seem to resist being anywhere at all, and only appear to me momentarily and when viewed askance. My cloudscape of wood is no less fabricated than the cloud models I build in `Python`, but it somehow gets me closer to the experience of knowing a real cloud. In my research, I had become obsessed with the possibility of finding the sharp edge of a LISM cloud in the Alice data like an archaeologist digging for bones, losing sight of the fact that sharp edges have very little to do with real clouds and everything to do with my imaginary models of them.

In astronomy, we are in the business of catching moonbeams, of coming up with clever ways to momentarily hold the immaterial. In the end, our efforts seem to hinge on that which is lost in translation. The electron count measured by a CCD detector on a telescope is not the moonbeam itself, and no matter how well we characterize and quantify the noise in our system, what comes out the back end is always a co-construction, something partway between moonbeam and telescopic byproduct, a hybrid that reflects us, our tools, and our choices as much as it reflects the world we are trying to see. The physicist and feminist theorist Karen Barad explains that on the most fundamental, quantum level, the very act of measuring the world is to co-create it, to determine which way the wave function collapses, and thus we only ever, at best, "meet the universe halfway" (Barad 2007). This is not bad news, but actually quite exciting, and carries with it ethical ramifications.

If we are indeed co-creators of the world, we would do well to take fewer things

for granted. The questions we ask are not as neutral as we believe, but grow from the training we have received, from our institutions, and our scientific family tree. The very way we frame a question, and the instruments we build to answer them, inescapably shape the kinds of data we can collect, our interpretation, and the view we develop of the universe. Whether you take this metaphorically – or literally, as Barad does – the world is what we make of it. As a scientist I plan to continue asking unanswerable questions of the universe, and my hope is that, over time, I learn how to ask them kinder, and stranger, to bring into being a world that is gentler and wilier too.

Bibliography

1977, NASA Facts: Voyager

Adams, T. F. 1972, ApJ, 174, 439

Ajello, J. M., Stewart, A. I., Thomas, G. E., & Graps, A. 1987, ApJ, 317, 964

Arulanantham, N., et al. 2023, ApJ, 944, 185

Bagenal, F., et al. 2023, in AAS/Division for Planetary Sciences Meeting Abstracts, Vol. 55, AAS/Division for Planetary Sciences Meeting Abstracts, 215.01

Baker, D. J., & Romick, G. J. 1976, Appl. Opt., 15, 1966

Baliukin, I., Bertaux, J.-L., Bzowski, M., Izmodenov, V., Lallement, R., Provornikova, E., & Quémerais, E. 2022, Space Sci. Rev., 218, 45

Barad, K. M. 2007, Meeting the Universe Halfway : Quantum Physics and the Entanglement of Matter and Meaning (Durham, N.C.: Duke University Press)

Box, G. E. P., & Draper, N. R. 1986, Empirical model-building and response surface (USA: John Wiley & Sons, Inc.)

Brandt, P. C., et al. 2023, Space Sci. Rev., 219, 18

Breitschwerdt, D. 1998, in IAU Colloq. 166: The Local Bubble and Beyond, ed. D. Breitschwerdt, M. J. Freyberg, & J. Truemper, Vol. 506, 5–16

Chamberlain, J. W. 1961, Physics of the aurora and airglow

Cox, D. P. 2005, ARA&A, 43, 337

Crutcher, R. M. 1982, ApJ, 254, 82

Czesla, S., Schröter, S., Schneider, C. P., Huber, K. F., Pfeifer, F., Andreasen, D. T., & Zechmeister, M. 2019, PyA: Python astronomy-related packages

Dayal, P., Ferrara, A., & Saro, A. 2010a, MNRAS, 402, 1449

Dayal, P., Hirashita, H., & Ferrara, A. 2010b, MNRAS, 403, 620

Dijkstra, M., Haiman, Z., & Spaans, M. 2006, ApJ, 649, 14

Draine, B. T. 2011, Physics of the Interstellar and Intergalactic Medium

Frisch, P. C., et al. 2022, ApJS, 259, 48

Frisch, P. C., Redfield, S., & Slavin, J. D. 2011, ARA&A, 49, 237

Frisch, P. C., & Slavin, J. D. 2013, Earth, Planets and Space, 65, 175

Frisch, P. C., & York, D. G. 1983, ApJ, 271, L59

Giorgini, J. D., Chodas, P. W., & Yeomans, D. K. 2001, in AAS/Division for Planetary Sciences Meeting Abstracts, Vol. 33, AAS/Division for Planetary Sciences Meeting Abstracts #33, 58.13

Giorgini, J. D., & Yeomans, D. K. 1999, NASA TECH BRIEFS, NPO-20416, 48

Giorgini, J. D., et al. 1996, in AAS/Division for Planetary Sciences Meeting Abstracts, Vol. 28, AAS/Division for Planetary Sciences Meeting Abstracts #28, 25.04

Gladstone, G. R. 2024, Private Communication

Gladstone, G. R., et al. 2021, AJ, 162, 241

Gladstone, G. R., Pryor, W. R., & Stern, S. A. 2015, Icarus, 246, 279

Gladstone, G. R., et al. 2018, Geophys. Res. Lett., 45, 8022

Gronke, M., & Dijkstra, M. 2014, MNRAS, 444, 1095

Gry, C., & Jenkins, E. B. 2014, A&A, 567, A58

—. 2017, A&A, 598, A31

Gry, C., Lemonon, L., Vidal-Madjar, A., Lemoine, M., & Ferlet, R. 1995, A&A, 302, 497

Gurung-López, S., Orsi, Á. A., & Bonoli, S. 2019, MNRAS, 490, 733

Hall, D. T. 1992, PhD thesis, University of Arizona

Hansen, M., & Oh, S. P. 2006, MNRAS, 367, 979

Harrington, J. P. 1973, MNRAS, 162, 43

Haud, U. 2010, A&A, 514, A27

Heger, M. L. 1919a, PASP, 31, 304

—. 1919b, Lick Observatory Bulletin, 326, 59

Hunten, D. M., Roach, F. E., & Chamberlain, J. W. 1956, Journal of Atmospheric and Terrestrial Physics, 8, 345

Keller, H. U., Richter, K., & Thomas, G. E. 1981, A&A, 102, 415

Kohlhase, C. E., & Penzo, P. A. 1977, Space Sci. Rev., 21, 77

Krimigis, S. M., et al. 2019, Nature Astronomy, 3, 997

Kulkarni, S. R., & Shull, J. M. 2023, Two-photon production in low-velocity shocks

Lallement, R., & Bertin, P. 1992, A&A, 266, 479

Lallement, R., Bertin, P., Ferlet, R., Vidal-Madjar, A., & Bertaux, J. L. 1994, A&A, 286, 898

Lallement, R., Ferlet, R., Lagrange, A. M., Lemoine, M., & Vidal-Madjar, A. 1995, A&A, 304, 461

Lallement, R., Quémerais, E., Bertaux, J.-L., Sandel, B. R., & Izmodenov, V. 2011, Science, 334, 1665

Lallement, R., Welsh, B. Y., Vergely, J. L., Crifo, F., & Sfeir, D. 2003, A&A, 411, 447

Laursen, P., Razoumov, A. O., & Sommer-Larsen, J. 2009, ApJ, 696, 853

Linsky, J., Redfield, S., Ryder, D., & Moebius, E. 2022, Space Sci. Rev., 218, 16

Linsky, J. L., & Redfield, S. 2023, Frontiers in Astronomy and Space Sciences, 10, 15

Linsky, J. L., Redfield, S., Wood, B. E., & Piskunov, N. 2000, ApJ, 528, 756

Linsky, J. L., Rickett, B. J., & Redfield, S. 2008, ApJ, 675, 413

Linsky, J. L., & Wood, B. E. 1996, ApJ, 463, 254

Malamut, C., Redfield, S., Linsky, J. L., Wood, B. E., & Ayres, T. R. 2014, ApJ, 787, 75

McClintock, W., Henry, R. C., Linsky, J. L., & Moos, H. W. 1978, ApJ, 225, 465

McKee, C. F., & Ostriker, J. P. 1977, ApJ, 218, 148

Meier, R. R. 1995, ApJ, 452, 462

Meyer, D. M., Lauroesch, J. T., Heiles, C., Peek, J. E. G., & Engelhorn, K. 2006, ApJ, 650, L67

Möbius, E., et al. 2004, A&A, 426, 897

Morton, D. C. 2004, ApJS, 151, 403

Neufeld, D. A. 1990, ApJ, 350, 216

Oort, J. H. 1950, Bull. Astron. Inst. Netherlands, 11, 91

Opher, M., Loeb, A., Drake, J., & Toth, G. 2020, Nature Astronomy, 4, 675

Orsi, A. 2010, PhD thesis, Durham University

Orsi, A., Lacey, C. G., & Baugh, C. M. 2012, MNRAS, 425, 87

Osterbrock, D. E. 1962, ApJ, 135, 195

Parker, E. N. 1958, ApJ, 128, 664

—. 1961, ApJ, 134, 20

Poppe, A. R. 2016, **??**jnlIcarus, 264, 369

Pryor, W., et al. 2008, A&A, 491, 21

Pryor, W. R., Gladstone, G. R., Retherford, K. D., Tobiska, W. K., Holsclaw, G. M., & Esposito, L. W. 2024, The Astrophysical Journal, 960, 117

Pryor, W. R., et al. 1998, J. Geophys. Res., 103, 26833

Quémerais, E. 2000, A&A, 358, 353

Quemerais, E., & Bertaux, J. L. 1993, A&A, 277, 283

Quemerais, E., Malama, Y. G., Sandel, B. R., Lallement, R., Bertaux, J. L., & Baranov, V. B. 1996, A&A, 308, 279

Quémerais, E., Sandel, B. R., Bertaux, J. L., & Lallement, R. 2000, Ap&SS, 274, 123

Redfield, S. 2006, in Astronomical Society of the Pacific Conference Series, Vol. 352, New Horizons in Astronomy: Frank N. Bash Symposium, ed. S. J. Kannappan, S. Redfield, J. E. Kessler-Silacci, M. Landriau, & N. Drory, 79

Redfield, S., & Linsky, J. L. 2000, ApJ, 534, 825

—. 2001, ApJ, 551, 413

—. 2004, ApJ, 602, 776

—. 2008, ApJ, 673, 283

—. 2015, ApJ, 812, 125

Rodgers, R., & Hammerstein, O. 1959, Maria

Rybicki, G. B., & Lightman, A. P. 1979, Radiative processes in astrophysics

Saintonge, A., & Catinella, B. 2022, ARA&A, 60, 319

Shull, J. M., & Kulkarni, S. R. 2023, ApJ, 951, 35

Smith, B. A., et al. 1981, Science, 212, 163

—. 1989, Science, 246, 1422

—. 1986, Science, 233, 43

—. 1979, Science, 204, 951

Spitzer, L. 1978, Physical processes in the interstellar medium

Starecheski, S., Redfield, S., & Zucker, C. 2023, in American Astronomical Society Meeting Abstracts, Vol. 55, American Astronomical Society Meeting Abstracts, 212.03

Stern, A., & Spencer, J. 2003, Earth Moon and Planets, 92, 477

Stern, S. A. 2023, Private Communication

Stern, S. A., et al. 2015, Science, 350, aad1815

—. 2008, Space Sci. Rev., 140, 155

Stern, S. A., Spencer, J. R., Weaver, H. A., & Olkin, C. B. 2021, in The Pluto System After New Horizons, ed. S. A. Stern, J. M. Moore, W. M. Grundy, L. A. Young, & R. P. Binzel, 587–601

Stern, S. A., et al. 2019, Science, 364, aaw9771

Stone, E. C. 1981, J. Geophys. Res., 86, 8123

Stone, E. C., Cummings, A. C., Heikkila, B. C., & Lal, N. 2019, Nature Astronomy, 3, 1013

Stone, E. C., Cummings, A. C., McDonald, F. B., Heikkila, B. C., Lal, N., & Webber, W. R. 2013, Science, 341, 150

Streitmatter, R. E., & Jones, F. C. 2005, in International Cosmic Ray Conference, Vol. 3, 29th International Cosmic Ray Conference (ICRC29), Volume 3, 157

Swaczyna, P., et al. 2022, ApJ, 937, L32

Thomas, G. E. 1978, Annual Review of Earth and Planetary Sciences, 6, 173

Vannier, H. N., Redfield, S., Wood, B. E., Mueller, H. R., Linsky, J. L., & Frisch, P. C. 2019, in AGU Fall Meeting Abstracts, Vol. 2019, SH51E–3323

Velez, M. A., et al. 2023, arXiv e-prints, arXiv:2303.04043

VERA Collaboration et al. 2020, PASJ, 72, 50

Verhamme, A., Schaerer, D., & Maselli, A. 2006, A&A, 460, 397

Weaver, H. 2018, in 42nd COSPAR Scientific Assembly, Vol. 42, B1.2–1–18

Webber, W. R., & McDonald, F. B. 2013, Geophys. Res. Lett., 40, 1665

Wolfire, M. G., McKee, C. F., Hollenbach, D., & Tielens, A. G. G. M. 2003, ApJ, 587, 278

Wood, B. E. 2004, Living Reviews in Solar Physics, 1, 2

Wood, B. E., Linsky, J. L., Müller, H.-R., & Zank, G. P. 2001, ApJ, 547, L49

Wood, B. E., Müller, H. R., Zank, G. P., Izmodenov, V. V., & Linsky, J. L. 2004, Advances in Space Research, 34, 66

Wood, B. E., Redfield, S., Linsky, J. L., Müller, H.-R., & Zank, G. P. 2005, ApJS, 159, 118

Wyman, K., & Redfield, S. 2013, ApJ, 773, 96

Zank, G. P., & Frisch, P. C. 1999, ApJ, 518, 965

Zheng, Z., & Miralda-Escudé, J. 2002, ApJ, 578, 33

Zucker, C., et al. 2022, Nature, 601, 334